OLGA DOCENKO

NaRb UN NaCs MOLEKULU PAMATSTĀVOKĻU UN ATSEVIŠĶU IEROSINĀTU STĀVOKĻU AUGSTAS IZŠĶIRTSPĒJAS SPEKTROSKOPIJA

HIGH-RESOLUTION SPECTROSCOPY OF THE GROUND AND SELECTED EXCITED STATES OF THE NaRb AND NaCs MOLECULES

Doktora disertācija / Doctor thesis

Darba vadītāji
Vad. pētn., Dr. habil phys. Māris Tamanis
Prof., Dr. habil phys. Ruvins Ferbers

Latvijas Universitāte / University of Latvia

Rīga – 2006

Promotion work was accomplished in the Institute of Atomic Physics and Spectroscopy of the Faculty of Physics and Mathematics of the University of Latvia in the period from year 2002 to year 2006.

Type of work: dissertation

Scientific supervisors: Leading researcher., Dr.habil.phys. Māris Tamanis

Professor, Dr. habil. phys. Ruvins Ferbers

The work was reviewed by:

1. _____

_____

2._____

_____

3._____

_____

The defence of work will take place at the open meeting of the Astronomical and Physical Sciences Division of the Promotion Council at the University of Latvia on ''___'' _____ of 2006 at _____ in Zeļļu str 8 ____ leture hall.

The work and its summary are on public display in the scientific library of the University of Latvia (Kalpaka bulv. 4) and in the Latvian Academic library (Rūpniecības iela 10).

The Chairman of the Astronomical and Physical Sciences Division
of the Promotion Council at the University of Latvia:

_____

/ Prof. R. Ferber /

Abstract

Thesis is devoted to high resolution spectroscopic studies of heteronuclear alkali dimers. Research objects are NaRb and NaCs molecules. They were chosen to respond the demand for accurate spectroscopic information on the electronic states of these molecules, especially the ground states, due to growing interest to cold collision experiments with Na–Rb and Na–Cs pairs. Besides, the theoretical calculations needed a comparison with reliable experimental data. Therefore the following main goal of the present research was introduced: to obtain accurate spectroscopic information on the ground and selected excited states of the NaRb and NaCs molecules. The method applied is a Fourier transform spectroscopy of Laser induced fluorescence. For the first time the $X^1\Sigma^+$, $a^3\Sigma^+$, $C^1\Sigma^+$, $D^1\Pi$ states of NaRb and $X^1\Sigma^+$, $a^3\Sigma^+$ states of NaCs have been studied experimentally with high accuracy in a wide range of internuclear distances. Accurate empirical potential energy curves of these states have been determined and compared with the recent theoretical calculations. Our work has demonstrated that Fourier transform spectroscopy of laser induced florescence is a powerful tool for studying not only of ground states, but also excited states due to collision induced transitions. The results obtained in the course of work open path for new experimental studies, e.g. dynamic and structural studies of these molecules and cold collision experiments with atomic pairs.
Thesis consists of Abstract, 6 Chapters, including Introduction and Conclusions (105 pages, 50 figures and 18 Tables), and of References (105 citations). Thesis is written in the English language.

Anotācija

Promocijas darbs ir veltīts heteronukleāro sārmu metālu divatomu molekulu augstas izšķirtspējas spektroskopiskiem pētījumiem. Pētījuma objekti ir NaRb un NaCs molekulas. Tās tika izvēlētas, lai apmierinātu pieprasījumu pēc precīzas spektroskopiskās informācijas par šo molekulu elektroniskajiem stāvokļiem. Pateicoties augošai interesei par auksto sadursmju eksperimentiem ar Na-Rb un Na-Cs atomu pāriem, īpaši interesanti ir šo molekulu pamatstāvokļi. Arī *ab initio* aprēķinu precizitātes novērtēšanai ir nepieciešams salīdzinājums ar ticamiem eksperimentāliem datiem. Tāpēc promocijas darbam tika izvirzīts galvenais mērķis: iegūt precīzu spektroskopisku informāciju par NaRb un NaCs molekulu pamatstāvokļiem un atsevišķiem ierosinātiem stāvokļiem. Kā metode šī mērķa sasniegšanai tika izvēlēta lāzera inducētās fluorescences Furjē spektroskopija. NaRb molekulas $X^1\Sigma^+$, $a^3\Sigma^+$, $C^1\Sigma^+$ un $D^1\Pi$ stāvokļi un NaCs molekulas $X^1\Sigma^+$ un $a^3\Sigma^+$ stāvokļi pirmoreiz tika ar augstu precizitāti eksperimentāli izpētīti plašā starpkodolu attālumu diapazonā. Tika noteiktas šo stāvokļu empīriskās potenciālās enerģijas līknes un salīdzinātas ar teorētiskajiem aprēķiniem. Darbs parādīja, ka lāzera inducētās fluorescences Furjē spektroskopija ir laba metode ne tikai pamatstāvokļu, bet arī ierosinātu stāvokļu pētījumiem, pateicoties sadursmju izraisītām pārejām. Darbā iegūtie rezultāti paver iespējas jauniem eksperimentiem, piemēram, šo molekulu dinamiskiem un strukturāliem pētījumiem, auksto sadursmju eksperimentiem ar atomu pāriem.

Promocijas darbs satur anotāciju, 6 nodaļas, ieskaitot ievadu un secinājumus (105 lapas, 50 attēli un 18 tabulas), kā arī literatūras sarakstu (105 atsauces). Darbs ir uzrakstīts angļu valodā.

Contents

List of Abbreviations

BEC	Bose-Einstein condensation
BO	Born-Oppenheimer (approximation)
CCC	Coupled channels calculation
CDC	Centrifugal distortion constants
DCM	dicyanometylene dye
DPF	Direct potential fit
EPAPS	Electronic supplementary material
FCF	Franck-Condon factor
FTS	Fourier-transform spectrometer, Fourier-transform spectroscopy
FWHM	Full width at half-maximum level
HFS	Hyperfine structure
HP	heat-pipe
IPA	Inverted perturbation approach
LIF	Laser-induced fluorescence
LS	Least-squares (method)
MLJ	Morse-Lennard-Jones
MPPT	Multi-partitioning perturbation theory
Nd:YAG	Neodymium yttrium aluminum garnet
OODRPS	Optical-optical double resonance polarization spectroscopy
PA	Photoassociation
PCPP	Polynomial-corrected pointwise potential
PEC	Potential energy curve
PLS	Polarization labeling spectroscopy
PW	Pointwise (potential)
RF-ODR	Radio frequency – optical double resonance
Rh6G	Rhodamine 6G dye
RKR	Rydberg-Klein-Rees (potential)
SE	Schrödinger equation
SNR	Signal-to-noise ratio
SPP	Spline-pointwise potential
SVD	Singular value decomposition
WF	Wavefunction
WKB	Wentzel-Kramers-Brillouin
WLS	Weighted least-squares (method)

Chapter 1

Introduction

Motivation

Alkali-metal diatomic molecules have been a subject of scientific research for already more than a century since the first observation of Na_2 fluorescence in 1891 [1]. A lot of significant results have been obtained in this field already in pre-laser epoch [2, 3], but a real breakthrough has happened after invention of a laser. And since then alkali-metal diatomic molecules have proved to be in a focus of intensive experimental and theoretical studies. This is explained by the fact that they are the simplest molecules consisting from atoms having only one valence electron, therefore they can be used as test objects to probe different theoretical approaches. Understanding the structure of diatomic molecules is an essential step from atoms to bigger molecules. From the experimental point of view these molecules can be produced relatively easy and their spectra can be excited with a variety of conventional laser sources (Ar^+, He–Ne, dye lasers, etc.). From these experiments researchers can derive information about potential energy curves (PEC) of molecular states, permanent electric dipole moments, lifetimes, transition dipole moments, etc. and compare them with theoretical calculations. In spite of seemingly simple structure of alkali-metal dimers accuracy of fully theoretical (*ab initio*) calculations is not yet sufficient, due to the fact that Schrödinger equation cannot be solved analytically for these molecules, and approximations are used. For example, discrepancy of empirical and theoretical potential energy curves for heteronuclear dimers can reach several hundreds cm^{-1}, versus experimental error of less than 0.1 cm^{-1}. Therefore comparison with experimental data is essential for making choice among different models and theoretical approaches.

Homonuclear alkali dimers (e.g. Na_2, K_2) are the best studied diatomic alkali molecules. There is much less information on heteronuclear alkali molecules. The best studied heteronuclear alkali dimer is NaK molecule. There are still large gaps in knowledge of the structure of other molecules and the task of the molecular spectroscopy is to obtain accurate information about different electronic states, especially the ground state. Experimental knowledge of the ground state is essential, as all molecular transitions have their origin there. Accurate description of the ground state in the form of molecular constants or PEC is demanded for assignment of observed transitions, which is, in turn, a necessary step for further studies of excited states. Also knowledge of ground state PEC allows one to construct the so-called difference-based potentials from the *ab initio* PECs [4]. In a number of cases this approach yields a much better representation of excited molecular states compared to pure *ab initio*. Study of diatomic molecules also provides information about interactions of electronic states through observations of perturbations in the spectra [5]. For example, study of phenomena like Λ-doubling allows one to measure directly the strength of intramolecular $^1\Pi \sim {}^1\Sigma^{\pm}$ interaction, yielding an essentially novel insight into the structure not only of an isolated $^1\Pi$ state, but of a $^1\Pi \sim {}^1\Sigma^{\pm}$ complex.

Especial interest is put on studies of the ground and lowest triplet states near the asymptote. This is motivated by the other field of research of alkali dimers—formation of cold molecules. Currently, the goal of many researchers in the fields of atomic and molecular physics, physical chemistry and chemical

physics is to produce dense samples of ultracold[1] polar molecules (see Special issue on Cold Molecules [6] and references therein). This interest is motivated by the fact that molecules offer intriguing properties which are not available with atoms. This especially applies to heteronuclear molecules, which have permanent electric dipole moments. Formation of ultracold molecules is of actual interest for such fields as: controlling chemical reactions and collisions (ultracold chemistry) [7]; observation of Bose-Einstein condensation (BEC) and Fermi degeneracy with molecules; high resolution molecular spectroscopy; tests of fundamental theories such as search for an electric dipole moment of the electron [8, 9]; quantum computation using aligned molecular dipoles as qubits [10], etc.

Ultracold alkali *atomic* samples have been already successfully created and atomic BEC was formed. This became possible thanks to elaboration of methods for cooling, trapping, and manipulating of atoms. In 1997 and 2001 Nobel prizes in physics [11] were awarded for the research in this field, which highlights the general importance of these developments and achievements.

Now physicists move to more complex and challenging systems—to diatomic molecules. Cooling molecules is more difficult than cooling atoms. The complex molecular internal level structure does not allow a simple extension of laser cooling to molecules. Despite this, considerable progress has been made and we are in a period of very rapid world-wide growth in this new field. One of the most promising methods allowing to reach ultracold temperatures is *photoassociation* of ultracold atoms [12]: a pair of atoms first resonantly absorbs a photon to create a molecule in an excited electronic state, which may then be stabilized into a long-lived electronic state by spontaneous emission, or by induced emission from a second laser. The development of cold molecule formation schemes appears to be crucially dependent on *accurate spectroscopic information* about the molecules and on *active interplay between theory and experiment* (see Ref. [13, 14] and references therein). The stable alkali homonuclear ultracold molecules were formed [15, 16, 17, 18, 19]. Recently successful production of *ultracold* RbCs [20], KRb [21, 22] and NaCs [23] *heteronuclear dimers* via photoassociation was reported. Ultracold collisions and trap loss experiments were also performed for Na–Li [24] and Na–Rb pairs [25, 26]. In parallel, active theoretical investigations are done in order to choose the most promising ultracold molecule formation scheme, e.g. photoassociation rates of mixed cold alkali atom pairs and formation rates of cold heteronuclear alkali dimers in their ground state were computed, which showed that all alkali pairs involving either Rb and Cs are well suited for that purpose [27].

Another prospective method for formation of ultracold molecules is via magnetic Feshbach resonances. In the ultracold regime the collision of two atoms is described by the scattering length, which is very sensitive to the interaction (molecular) potential. If the atoms or the molecule or both are paramagnetic, the potential can be tuned by an external magnetic field. A Feshbach resonance occurs when the energy of the unbound state (the atomic pair) and of the bound state (the diatomic molecule) become equal. The scattering length changes at a Feshbach resonance. It can be made positive or negative and its magnitude arbitrarily large. By tuning through a resonance the atom pair can be driven into the bound molecular state. Information on scattering lengthes and Feshbach resonances can be obtained from *traditional spectroscopy* (molecular beam, laser-induced fluorescence spectroscopy) by studying energy positions of the last bound molecular levels with respect to the dissociation limit, see e.g. [28]. Knowledge of scattering lengths is also essential for formation of BEC, because the stability of a condensate is controlled by the sign of the scattering length. Two groups have found Feshbach resonances in heteronuclear systems [29, 30]. The next step is to transfer molecule to more tightly bound states using, for example, stimulated Raman process via $b^3\Pi \sim A^1\Sigma^+$ mixed levels [31]. Therefore *data from conventional short-range spectroscopy about molecular electronic states and especially the strongly mixed* $b^3\Pi \sim A^1\Sigma^+$ *complex are needed for planning such type of experiments.*

Heteronuclear diatomic molecules are also interesting objects for applied science. For example, prospective application of polar diatomics, especially in the $^1\Pi$ states, is connected with their usage for sensitive non-contact probing and mapping of external electric field distribution via changes in laser-induced fluorescence caused by parity mixing due to quasi-linear Stark effect [32, 33].

[1] As "cold" usually designate molecules with translational temperatures between 1 and 1000 mK, and as "ultracold"—with translational temperature less than 1 mK.

Research objects and goals

Research objects of the present Thesis are **NaRb** and **NaCs** molecules. They were chosen to respond the demand for accurate spectroscopic information on the electronic states of these molecules, especially the ground states, due to growing interest to cold collision experiments with Na–Rb [25, 26] and Na–Cs [23] pairs. Besides, the *ab initio* calculations [34, 4, 35] needed a comparison with reliable experimental data. Therefore the following main **goals** of the present research were introduced:

1. To obtain the NaRb $X^1\Sigma^+$ and $a^3\Sigma^+$ state accurate empirical PECs in a wide range of internuclear distancess and to perform the combined analysis of these states taking into account hyperfine mixing.
2. To obtain the NaRb $C^1\Sigma^+$ state accurate empirical PEC.
3. To obtain the NaRb $D^1\Pi$ state accurate empirical PEC, to study Λ-splitting in this state.
4. To obtain the NaCs $X^1\Sigma^+$ and $a^3\Sigma^+$ state accurate empirical PECs in a wide range of internuclear distances; to perform the combined analysis of these states taking into account hyperfine mixing.

Method and tasks

The **method** chosen for fulfilling these goals is a *Laser Induced Fluorescence* (LIF) method. The following methodological **tasks** have been formulated:

1. To prepare experimental setup for performing LIF measurements in the NaRb and NaCs molecules.
2. To excite electronic transitions in NaRb and NaCs, involving the states of interest, by using different laser sources.
3. To perform vibrational, rotational and isotopomer assignment of progressions in electronic spectra, as well as for rotational relaxation transitions. In the case of the $D^1\Pi$ state to analyse the derived Λ-splittings.
4. To perform a fitting procedure of potential energy curves to experimental data. To analyse the quality of potentials and to compare with available *ab initio* data.

A number of experiments have been carried out in order to realize these tasks. The initial part of experiments (NaRb $X^1\Sigma^+$ state) was done in Riga, in the Laboratory of Optical Polarisation of Molecules (head Prof. R. Ferber), Institute of Atomic Physics and Spectroscopy, University of Latvia. The further experiments were performed using high-resolution Fourier-transform spectrometer in the laboratory of Prof. E. Tiemann, Institute of Quantum Optics, University of Hannover.

The structure of the Thesis is the following. In the Second Chapter the theoretical background of the performed research is briefly given. In the Third Chapter the experimental setups are described. In the Fourth Chapter the results on the NaRb $X^1\Sigma^+$, $a^3\Sigma^+$, $C^1\Sigma^+$ and $D^1\Pi$ states are presented, whereas the Fifth Chapter is devoted to the NaCs $X^1\Sigma^+$ and $a^3\Sigma^+$ states. Results and conclusions are given in Chapter 6.

Publications

The main results of the Thesis are presented in the following scientific papers:

[dis1] **O. Docenko**, O. Nikolayeva, M. Tamanis, R. Ferber, E.A. Pazyuk and A.V. Stolyarov, *Experimental studies of the NaRb ground state potential up to $v'' = 76$ level*, Physical Review A 66, 052508 (2002).

[dis2] **O. Docenko**, M. Tamanis, R. Ferber, A. Pashov, H. Knöckel, and E. Tiemann, *Potential of the ground state of NaRb*, Physical Review A 69, 042503 (2004).

[dis3] A. Pashov, **O. Docenko**, M. Tamanis, R. Ferber, H. Knöckel, E. Tiemann, *Potentials for modeling cold collisions between Na (3S) and Rb (5S) atoms*, Physical Review A 72, 062505 (2005).

[dis4] W. Jastrzebski, P. Kortyka, P. Kowalczyk, **O. Docenko**, M. Tamanis, R. Ferber, A. Pashov, H. Knöckel, E. Tiemann, *Accurate characterisation of the* $C(3)^1\Sigma^+$ *state of the NaRb molecule*, European Physical Journal D 36, 57-65 (2005).

[dis5] **O. Docenko**, M. Tamanis, R. Ferber, A. Pashov, H. Knöckel, E. Tiemann, *The* $D^1\Pi$ *state of the NaRb molecule*, European Physical Journal D 36, 49-55 (2005).

[dis6] **O. Docenko**, M. Tamanis, R. Ferber, A. Pashov, H. Knöckel, E. Tiemann, *Spectroscopic studies of NaCs for the ground state asymptote of Na + Cs pairs*, European Physical Journal D 31, 205-211 (2004).

The obtained results have been reported in a number of international conferences, which is reflected in the following conference abstracts:

- **O. Docenko**, I. Klincare, O. Nikolayeva, M. Tamanis, R. Ferber, E.A. Pazyuk and A.V. Stolyarov, *Laser induced fluorescence studies of the NaRb molecule ground state up to* $v'' = 76$, in Abstracts of the 34th EGAS Conference (Sofia, Bulgaria, July 9-12, 2002), 26C, p. 80-81.
- **O. Docenko**, I. Klincare, O. Nikolayeva, M. Tamanis, R. Ferber, E. A. Pazyuk and A. V. Stolyarov, *Spectroscopic studies of the NaRb ground state up to near - dissociation limit*, , in Abstracts of the 17th International Conference on High Resolution Spectroscopy (Prague, Czech Republic, September 1-5, 2002) p. 185.
- **O. Docenko**, M. Tamanis, R. Ferber, A. Pashov, H. Knöckel, E. Tiemann, *Fourier-transform spectroscopy of NaRb*, 35th EGAS conference, in Abstracts of the 35th EGAS Conference (Brussels, Belgium, July 15-18, 2003), 27B, p. 65.
- **O. Docenko**, M. Tamanis, R. Ferber, A. Pashov, H. Knöckel, E. Tiemann, *Fourier-transform spectroscopy studies of the NaRb molecule*, in Abstracts of the workshop Non-destructive electric field imaging and high-frequency plasma applications for nanoscale surface treatment (Riga, August 21-22, 2003), p.10.
- **O. Docenko**, M. Tamanis, R. Ferber, A. Pashov, H. Knöckel, and E. Tiemann, *The* $D^1\Pi$ *state of the NaRb molecule*, in Abstracts of the ECAMP 8 conference (Rennes, France, July 6-10, 2004), 28F, vol. 2, p. 43.
- **O. Docenko**, M. Tamanis, R. Ferber, A.Pashov, H. Knöckel, and E. Tiemann, *The* $a^3\Sigma^+$ *state of the NaRb molecule*, in Abstracts of the ECAMP 8 conference, 28F, vol. 2, p. 44.
- **O. Docenko**, M. Tamanis, R. Ferber, A. Pashov, H. Knöckel, and E. Tiemann, *The ground state of NaCs*, in Abstracts of the ECAMP 8 conference, 28F, vol. 2, p. 45.
- W. Jastrzebski, P. Kortyka, P. Kowalczyk, **O. Docenko**, M. Tamanis, R. Ferber, A. Pashov, H. Knöckel, and E. Tiemann, *The accurate* $C^1\Sigma^+$ *state potential of the NaRb molecule*, in Abstracts of the ECAMP 8 conference, 28F, vol. 2, p. 85.
- H. Knöckel, **O. Docenko**, E. Zaharova, M. Tamanis, R. Ferber, A. Pashov, and E. Tiemann, *Spectroscopic studies of the NaCs triplet ground state*, in Verhandlungen der Deutschen Physikalischen Gesellschaft (Berlin, March 4-9, 2005), p. 70.
- **O. Docenko**, J. Zaharova, M. Tamanis, R. Ferber, A. Pashov, H. Knöckel, E. Tiemann, The $a^3\Sigma^+$ state of the NaCs molecule, in Abstracts of the 37th EGAS Conference (Dublin, Ireland, August 3-6, 2005), 29I, p. 189.

Chapter 2

Structure and spectra of diatomic molecules

2.1 Born-Oppenheimer approximation

For the full quantum-mechanical treatment of a molecule it would be necessary to solve the time-independent Schrödinger equation (SE)

$$\hat{H}\Psi_i = E_i\Psi_i, \tag{2.1}$$

where $\hat{H}$ is the non-relativistic Hamiltonian for the molecule, E_i and Ψ_i are energies and wavefunctions (WF) of molecular eigenstates. For diatomic molecules $\hat{H}$ may be approximated as a sum of three operators

$$\hat{H} = \hat{T}^n(R,\theta,\varphi) + \hat{T}^{el}(r) + \hat{V}(r,R), \tag{2.2}$$

where $\hat{T}^n$ – nuclear kinetic energy operator,
$\hat{T}^{el}$ – electron kinetic energy operator,
$\hat{V}$ – operator of the electrostatic potential energy of the nuclei and electrons,
R – internuclear distance,
θ, φ – angles, which specify the orientation of the internuclear axis (molecule-fixed coordinate system) relative to the laboratory coordinate system,
r – coordinates of all electrons in the molecule-fixed frame.

However, the entire molecular system composed of interacting electrons and nuclei is so complicated that an exact quantum-mechanical solution is impossible and approximations are needed. Since the electrons are very much lighter than the nuclei, the electron motion is much faster than that of the nuclei. Thus, at each instant the electronic energy may be considered to have reached its equilibrium value corresponding to current internuclear distance. This justifies treating the vibration and rotation of nuclei separately from the electronic motion. It is therefore reasonable to treat the electronic motion first, considering nuclei as fixed. This approximation is called the *Born-Oppenheimer* (BO), or *adiabatic approximation*. It allows one to express the total molecular wave function as a product of nuclear Ψ_n and electronic Ψ_{el} wave functions:

$$\Psi_{BO} = \Psi_{el}(r,R) \cdot \Psi_n(R,\theta,\varphi), \tag{2.3}$$

Treating motion of electrons in the adiabatic approximation, the internuclear distance R is a parameter of Ψ_{el}. In this way the electrons are found to be capable of occupying several states, each giving the molecule a particular value of the energy $U(R)$, for each internuclear distance. In this treatment $U(R)$, which is the sum of the electron energy and energy of electrostatic interaction between the two nuclei,

appears as the *potential energy*. It can be viewed as the potential energy curve (PEC) in which the nuclei move, but it should be noted, that PECs do not correspond to any physical observable. They are a concept, derived from a specific set of assumptions for defining a particular type of approximate wavefunctions (2.3).

Factorization of the WF and separation of radial and angular variables (as in the case of hydrogen atom) allows to reduce the problem of a diatomic molecule to *the radial Schrödinger equation:*

$$\left[-\frac{\hbar^2}{2\mu}\frac{d^2}{dR^2} + \frac{\hbar^2}{2\mu R^2}\left(J(J+1) - \Omega^2\right) + U(R)\right]\Psi_{vJ}(R) = E_{vJ}\Psi_{vJ}(R), \tag{2.4}$$

where $\mu = \frac{M_A M_B}{M_A + M_B}$ – molecular reduced mass, M_A and M_B being the masses of atoms A and B,
$J(J+1)$ – an eigenvalue of the square of the total angular momentum operator $\hat{J}^2$,
Ω – projection of $\mathbf{J}$ on the internuclear axis,
v and J – vibrational and rotational quantum numbers.

Equation (2.4) has the form of the elementary Schrödinger equation for a particle moving in one-dimensional effective potential

$$U_{eff}(R) = U(R) + \frac{\hbar^2}{2\mu R^2}\left(J(J+1) - \Omega^2\right) \tag{2.5}$$

Here the first term is the total electronic potential, while the second is a centrifugal potential associated with the rotation of the molecular axis. Thus, the effect of increasing the rate of molecular rotation manifests itself as an addition of an increasingly strong repulsive centrifugal term to the basic (rotationless) PEC for a given electronic state.

Since it is actually seldom possible to solve the electronic wave equation, it is customary to use empirical expressions for $U(R)$.

2.2 Classification of electronic states and Hund's cases

Classification of molecular electronic states is made according to good quantum numbers which arise from angular momenta which commute with the total Hamiltonian. Let's consider different angular momenta and coupling between them in a diatomic molecule.

There is a close parallelism between the various angular momenta involved in molecules and those in atoms, however molecules involve more types of angular momenta (see Table 2.1) because of the possibility of rotation of a molecule. In addition, for linear and symmetric-top molecules the projection of various angular momenta on the symmetry axis may be of interest as well as their projections on a direction fixed in space. The diatomic molecule is somewhat similar to an atom subjected to a very large electric field along the direction of the molecular axis. This field produces a large Stark effect which interferes with the orbital motion of the electrons.

Although the orbital angular momentum is not constant and the quantum number L loses its significance, in many cases the projection Λ of $\mathbf{L}$ on the axis is constant. The energy is dependent on the value of Λ, which is, of course, integer and may be equal to Λ, $\Lambda - 1$, ..., $-\Lambda$. However, positive and negative values of Λ have the same energy, so that unless $\Lambda = 0$, the levels are doubly degenerate. This degeneracy may be removed by the rotation-electron interaction discussed below (Λ-type doubling).

If the electronic orbital angular momentum Λ along the internuclear axis of a linear molecule is 0, ±1, ±2, ±3, ..., the molecule is said to be in a Σ, Π, Δ, Φ, ... state, respectively. If the electronic spin S is 0, $\frac{1}{2}$, 1, ... the state is said to be singlet, doublet, or triplet—again in analogy with the atomic case. Thus $^1\Pi$ term indicates $S = 0$ and $\Lambda = 1$. The component of the total angular momentum along the molecular axis can take the values $\Lambda + S$, $\Lambda + S - 1$, ..., $\Lambda - S$, and is written as a right-hand term subscript, for example, $^3\Pi_1$. Its absolute value is denoted Ω.

The sequence of electronic terms is denoted by numbers or letters. Numbers are attributed in analogy with atomic principal quantum numbers, i.e. $(1)^1\Sigma^+$, $(2)^1\Sigma^+$, $(3)^1\Sigma^+$, etc. in the order of increasing

Table 2.1. Molecular angular momenta and their notations

Electronic orbital angular momentum	$\mathbf{L}$
Projection on molecular axis	Λ
Electron spin angular momentum	$\mathbf{S}$
Projection on molecular axis	Σ
Sum of spin and electronic orbital momentum ($\mathbf{L}$+$\mathbf{S}$)	$\mathbf{J}_a$
Rotational angular momentum	$\mathbf{R}$
Total orbital angular momentum including rotation of molecule	$\mathbf{N}$
Total angular momentum excluding nuclear spin	$\mathbf{J}$
Projection on molecular axis	Ω
Total angular momentum including nuclear spin	$\mathbf{F}$

energy. In the alphabetic way of labelling electronic states, the ground state is always labelled X, and, in order of increasing energy, other states of the same spin multiplicity are labelled A, B, C, ..., etc., while states of different spin multiplicity are labelled a, b, c, ..., etc.

Molecular angular momenta may interact, or couple together, in a various ways. The coupling cases were first systematically treated by Hund [36], who described five ideal cases. Molecules do not fit such ideal descriptions exactly, but Hund's cases are usually very good approximations to the actual states of many linear molecules. Which case applies most closely depends on the relative energy of interaction between the angular momentum vectors. Coupling between the nuclear spin and other vectors by hyperfine interaction is much smaller than other couplings, and is not treated in these cases. Interactions whose relative magnitude needs to be considered occur between any two of the vectors **L**, **S**, **N**, **R** and **A**, where **A** is a vector directed along the molecular axis. Interactions between two of those vectors will be represented by a notation like {**L, S**}.

Choice of Hund's cases means also a choice of basis set, which implies a partitioning of the Hamiltonian into a part $\mathbf{H}^0$, which is fully diagonal in the selected basis set, and a residual part, $\mathbf{H}'$. The basis sets associated with Hund's cases reflect different choices of the parts of **H** that are included in $\mathbf{H}^0$. Although in principle the eigenvalues of **H** are unaffected by the choice of basis, as long as this basis set forms a complete set of functions, one basis set is usually more convenient or appropriate than the others for a particular problem.

In the Hund's case (a), the strongest interactions are between the molecular axis and **L** and between the axis and **S**. **L** interacts strongly with the axial field of the molecule and hence precesses about the molecular axis, so that its projection Λ is constant. The electronic spin can not be coupled directly to the internuclear axis, since its associated moment has purely magnetic nature. But when $\Lambda \neq 0$, the magnetic field generated by orbital motion interacts with the spin angular momentum and coupling of **S** to the internuclear axis becomes possible, with projection Σ being constant. For $\Lambda = 0$ states Σ is not defined. In Hund's case (a) the total angular momentum along the molecular axis is $\Omega = |\Lambda + \Sigma|$. Then $\mathbf{\Lambda + \Sigma}$ adds vectorially to the rotational angular momentum **R** to form the total angular momentum (excluding nuclear spin) **J**. The angular momenta $\mathbf{\Omega}$ and **R** hence precess around the vector **J** which is fixed in space. Schematically this coupling can be expressed as {{{**L**, **A**}, **S**}, **R**}. Good quantum numbers in Hund's case (a) are J, S, Λ, Σ and Ω. The notation of electronic terms is ${}^{2S+1}\Lambda$.

In Hund's case (b) the electron spin is coupled more strongly to $\mathbf{N}$=$\mathbf{\Lambda}$+**R** than to the molecular axis. **L**, however, is still strongly coupled to the molecular axis. Shortly, coupling scheme is {{{**L**, **A**}, **R**}, **S**}. As for molecules with $\Lambda = 0$ the coupling between the spin and the molecular axis is small, they typically fall in Hund's case (b). However, there are molecules with $\Lambda \neq 0$ which also fall in case (b). These are usually very light molecules, such as hydrides, which rotate rapidly, increasing strength of the spin-rotation coupling. Good quantum numbers in Hund's (b) case are J, N, Λ and S. The notation of electronic terms is ${}^{2S+1}\Lambda$.

In molecules involving heavy nuclei, the spin-orbit interaction {**L, S**} may be larger than the {**L**, **A**} interaction. This gives Hund's case (c) with coupling scheme {{{**L**, **S**}, **A**}, **R**}. In this case Λ and S are not good quantum numbers any more. **L** and **S** add vectorially to form a vector $\mathbf{J}_a$ which is then coupled to the internuclear axis with a projection Ω on this axis. Therefore the only good quantum numbers are J and Ω. The electronic states are designated as Ω. It should be noted that Hund's case (c) starts to be important also for lighter molecules, when internuclear distance becomes sufficiently large, as in this case coupling of the angular momenta to the molecular axis weakens.

Hund's case (d) occurs when the coupling between **L** and the rotational momentum **R** is much larger than that between **L** and the molecular axis. This case is an intermediate between (b) and (e), as a decoupling of a part of the electronic motion from the axis takes place. The electron motion is described in two parts. One part (the core) is coupled to the axis and results to $\mathbf{J}_{core}$ and the other is free with respect to the molecular frame forming with $\mathbf{J}_{core}$ the total momentum **J**. An example of such state is a molecule with a Rydberg electron orbiting around the core with its orbital angular momentum l and its spin s.

Hund's case (e) appears for a highly rotating molecule, where rotational energy is so large that the coupling to the axis is of no importance anymore. Another example of this case is an atom pair close to dissociation. Due to weak binding energy the Hund's case (e) can already appear for slow rotation.

2.3 Symmetry properties of the wavefunctions

For the classification of molecular electronic states, the symmetry properties of the wavefunctions are very important. The electronic basis functions associated with positive and negative signs of $(\Lambda, \Sigma, \Omega)$ are degenerate. However, they are not symmetrized and only their linear combination has a well-defined symmetry. This symmetry is called parity and can be *even* (+) or *odd* (−). Even WFs are those which remain unchanged after inversion of spatial and spin coordinates of all electrons and nuclei, whereas odd WFs change their sign. This symmetry alternates with J, therefore a label free of J-dependence is introduced, the so called e/f parity: total parity is $+(-1)^J$ for e levels and $-(-1)^J$ for f levels.

For Σ states there is possible another type of symmetry arising from the reflection in any plane containing internuclear axis: Σ^+ and Σ^- states.

For homonuclear molecules (or more rigourously—when two nuclei have the same charge) there exists also a center of symmetry and WFs remain unchanged or change their sign when reflected at this center. This leads to gerade (g) — ungerade (u) symmetry.

2.4 Λ-doubling

In Hund's cases (a) and (b) the interaction between the rotation of the nuclei and orbital angular momentum **L** has been neglected. For larger speeds of rotation this interaction must be taken into account and is found to split each rotational level J into two components in the states with $\Lambda \neq 0$ which are doubly degenerate without rotation. In general, this splitting increases with increasing rotation—that is, with increasing J. It is present for all states with $\Lambda \neq 0$ and is called Λ-type doubling (shown qualitatively in the energy level diagram in Fig. 2.1).

The two Λ-doubling components do not correspond simply to projections $+\Lambda$ and $-\Lambda$ of **L** on the internuclear axis, but are linear combinations of wavefunctions for positive and negative values of Λ. The electronic-rotational WF $|\Lambda J M \epsilon\rangle$ can be expressed as a linear combination over rotational $|\Lambda J M\rangle$ parts [5]:

$$|\Lambda J M \epsilon\rangle = \frac{1}{\sqrt{2}} \left(|\Lambda\rangle |\Lambda J M\rangle + \epsilon |-\Lambda\rangle |-\Lambda J M\rangle \right) \tag{2.6}$$

ϵ being the "parity index" distinguishing between the two Λ-doublet states possessing total parity $+(-1)^J$ for $\epsilon = +1$ (e levels), and $-(-1)^J$ for $\epsilon = -1$ (f levels).

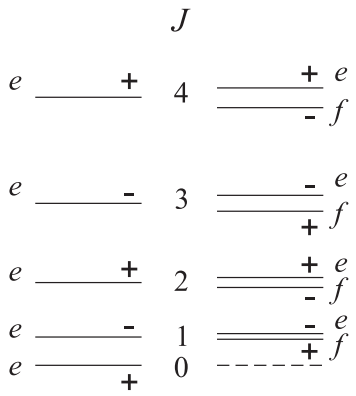

Figure 2.1. Rotational levels in the Σ^+ and $^1\Pi$ states.

Λ-splitting can be treated as electronic-rotational perturbation between the $^1\Pi$ state and $^1\Sigma^\pm$ states. In the case of regular perturbations [5] the splitting Δ_{ef} between e and f components of the initially degenerate rovibronic $^1\Pi$ levels is expected to be very small. Its main J dependence can be approximated by the second order nondegenerate perturbation theory as

$$\Delta_{ef}^{\Pi} = q_{vJ}^{\Pi} J(J+1), \tag{2.7}$$

where the so-called q-factor q_{vJ}^{Π} possesses a definite sign. The expression for q-factors takes the form

$$q_{vJ}^{\Pi} = \frac{1}{2\mu^2} \sum_{\Sigma} (-1)^k \sum_{v_\Sigma} \frac{|\langle v_J^{\Pi} | L_{\Pi\Sigma}/R^2 | v_J^{\Sigma} \rangle|^2}{E_{vJ}^{\Pi} - E_{v'J}^{\Sigma}} \tag{2.8}$$

and is expected to be a rather smooth function of the vibrational v and rotational J quantum numbers. Here $L_{\Pi\Sigma}(R)$ are the L-uncoupling electronic matrix elements between the sampled $^1\Pi$ state and the remote $^1\Sigma^\pm$ states ($k = 0$ and 1 for $^1\Sigma^+$ and $^1\Sigma^-$ states, respectively). The E_{vJ} and $|v_J\rangle$ are the eigenvalues and eigenfunctions of the vibrational SE. Due to the factor R^{-2} in Eq. (2.8), the main contribution to the q values of the given $^1\Pi$ state comes from $^1\Pi \sim {}^1\Sigma^\pm$ interactions having large matrix elements at relatively small internuclear distance R.

In such a way the q-factors reflect directly the measure of intramolecular $^1\Pi \sim {}^1\Sigma^\pm$ interaction, yielding an essentially novel insight into the structure not only of an isolated $^1\Pi$ state, but of a $^1\Pi \sim {}^1\Sigma^\pm$ complex.

2.5 Laser-Induced Fluorescence. Selection rules and intensity distribution

For studying internal energy structure of molecules one must probe it with electromagnetic radiation, i.e. to excite a molecule and to observe absorption or emission transitions between electronic, vibrational and rotational levels. In our work we applied a method of laser-induced fluorescence, in which incident monochromatic laser radiation selectively populates excited state levels (v', J'). Following this, the laser-induced fluorescence is observed. Its spectrum contains radiation from all allowed transitions to levels of lower states (v_i'', J_i''). Due to selective population of upper state levels the resulting spectrum is much easier to identify than absorption spectra.

The spontaneous transition probability A_{km} is proportional to the square of the matrix element of the electric dipole moment operator:

$$A_{km} \propto \left| \int \psi_k^* \cdot \mathbf{r} \cdot \psi_m d\tau_n d\tau_{el} \right|^2, \tag{2.9}$$

where $\mathbf{r}$ is the radius-vector of the excited electron and the integration extends over all nuclear and electronic coordinates. Within the BO approximation the total wave function can be separated into a product of electronic, vibrational and rotational factors. If the electronic transition moment does not critically depend on the internuclear separation R, the total transition probability is then proportional to the product of three factors

$$A_{km} \propto |M_{el}|^2 |M_{vib}|^2 |M_{rot}|^2, \tag{2.10}$$

where the first factor

$$M_{el} = \int \psi_{el}^{*\prime} \psi_{el}'' d\tau_{el}, \tag{2.11}$$

represents the electronic matrix element that depends on the coupling of the two electronic states. The second integral

$$M_{vib} = \int \psi_{vib}' \psi_{vib}'' d\tau_{vib}, \text{ with } d\tau_{vib} = R^2 dR \tag{2.12}$$

depends on the overlap of the vibrational wave functions in the upper and lower states. The square of this integral is called the *Franck-Condon factor* and it primarily determines the intensity pattern of the observed transitions. The third integral

$$M_{rot} = \int \psi_{rot}' \psi_{rot}'' g_i d\tau_{rot}, \text{ with } d\tau_{rot} = d\vartheta d\varphi \tag{2.13}$$

is called the *Hönl-London factor*. It depends on the orientation of the molecular axis relative to the electric vector of the observed fluorescence wave. This is expressed by the factor $g_i (i = x, y, z)$, where $g_x = \sin\vartheta \cos\varphi$, $g_y = \sin\vartheta \sin\varphi$, and $g_z = \cos\vartheta$ with ϑ and φ being the polar and azimuthal angles.

Only those transitions for which all three factors are nonzero appear as lines in the fluorescence spectrum. The Hönl-London factor is always zero unless

$$\Delta J = J' - J'' = 0, \pm 1, \text{ with exception } J' = 0 \nleftrightarrow J'' = 0 \tag{2.14}$$

which is one of two main selection rules governing laser-induced fluorescence (LIF) spectra. The second one is the parity selection rule:

$$+ \longleftrightarrow -.$$

Thus in ${}^1\Sigma \leftrightarrow {}^1\Sigma$ transitions only P $(J' - J'' = -1)$ and R $(J' - J'' = 1)$ lines are possible, whereas in ${}^1\Sigma \leftrightarrow {}^1\Pi$ transitions Q lines appear additionally at $\Delta J = 0$.

2.6 Perturbations

If the BO eigenenergies E_i don't coincide with the experimentally observed energies, it means that the assumed approximation is not valid, or, in other words, that the matrix representation of the total Hamiltonian, constructed by evaluating matrix elements between BO basis functions, has significant *off-diagonal elements*. Then a SE solution must be expressed as a linear combination of BO eigenfunctions. The coefficients of this expansion are determined by diagonalizing total Hamiltonian in the BO basis.

Neglecting some interactions, or couplings, in the molecule then corresponds to omitting some off-diagonal matrix elements. As a result of such approximation, observations don't fit calculations and this difference is treated as *a perturbation* in the framework of the used model.

Let's describe the nonzero off-diagonal matrix elements of the total Hamiltonian

$$\hat{H} = \hat{H}^{el} + \hat{T}^{n}(R) + \hat{H}^{ROT} \tag{2.15}$$

between approximate BO product basis functions. The off-diagonal matrix elements of the electronic energy operator $\hat{H}^{el}$ give rise to *electrostatic perturbations*. The off-diagonal matrix elements of nuclear kinetic energy operator $\hat{T}^{n}(R)$ give rise to *nonadiabatic interactions*. The off-diagonal matrix elements of nuclear rotation operator $\hat{H}^{ROT}$ give rise to rotational perturbations: *spin-electronic* and *electronic-rotational*. The total Hamiltonian discussed above is non-relativistic. Relativistic effects mainly consist of three parts: *spin-orbit, spin-rotation and spin-spin* interaction.

Selection rules for perturbations are $\Delta J = 0$, $e \leftrightarrow e$, $f \leftrightarrow f$ (except for the hyperfine perturbations).

2.7 Hyperfine structure in diatomic molecules

In most *atoms* the predominant mechanism responsible for the hyperfine structure is the *magnetic dipole interaction* between a nuclear magnetic moment and magnetic fields of the atomic electrons. Effects of nuclear *electric quadrupole moment* are smaller and give small deviations from the expected magnetic hyperfine intervals.

However, for most *molecules in the ground state* (usually the $^1\Sigma$ state) the magnetic fields due to various electrons almost completely cancel, giving zero or only very small magnetic fields at the nucleus. The cancelation of magnetic fields in molecules due to electronic motions is simply because the electrons are paired—for each electron with an angular momentum and hence magnetic field, there is another electron in a similar state but with oppositely directed angular momentum. But even for these molecules, however, there are weak interactions involving nuclear magnetic moments. These include interaction between magnetic moments of two nuclei in the same molecule (spin-spin interactions) and interaction between a nuclear magnetic moment and rather small magnetic fields produced by molecular rotation (spin-rotation interactions).

For the rare molecules having odd number of electrons, such as NO, ClO_2 and NO_2, a complete pairing of electron spins is impossible. These molecules in the ground state are hence paramagnetic and have large magnetic hyperfine structures. For the overwhelming majority of molecules, however, magnetic hyperfine effects are extremely small, and electric quadrupole hyperfine interaction plays the major role for molecules in the ground state.

When a molecule has non-zero electronic angular momentum, i.e., is in some state other than $^1\Sigma$, the magnetic fields associated with this momentum interact strongly with the nuclear moments present in the molecule, giving rise to a magnetic hyperfine structure of a magnitude comparable to one found in atoms. The interaction is either due to electronic orbital angular momentum $\mathbf{L}$ or to spin angular momentum $\mathbf{S}$.

Typical features of the molecular magnetic hyperfine interactions may be compared with those of atoms. The interaction of the nuclear spin with the electronic spins in the atomic case is treated quite differently in s state ($L = 0$) and non-s states. For non-s states, the spin coupling may be written as the interaction of two point magnetic dipole. For s-states, this interaction vanishes (as does the orbital interaction), and the actual hyperfine coupling must be accounted for by a more refined treatment of the magnetic interaction, namely by treating the interaction of the nuclear magnetic moment with the electronic currents via the Dirac equation for the electron. Advantage may be taken of the spherical symmetry of the potential field in which electron moves to express the hyperfine splitting in the form [37]

$$E_{\rm hfs} = \frac{16\pi}{3}\frac{\mu_0\mu_I}{I}\Psi_r^2(0)\mathbf{I}\cdot\mathbf{S}, \tag{2.16}$$

where μ_0 – Bohr magneton, μ_I – nuclear magnetic moment, $\mathbf{I}$ – nuclear spin, $\mathbf{S}$ – electron spin moment, $\Psi_r^2(0)$ – the electron density at the nucleus. This energy is called *Fermi contact interaction.*

In the case of diatomic molecule the potential field possesses only axial symmetry and no classification of state according to a total angular momentum quantum number can be made. Thus, there can be no separation of the hyperfine interaction into characteristic s- and non-s forms. Nevertheless, effects similar

to the atomic s-state interactions are found and term like in Eq. (2.16) appears in the energy expression for molecular state. Whenever there is an appreciable amount of s character to the WF of an unpaired electron, the hyperfine interaction which is proportional to $\Psi_r^2(0)$ may be expected to dominate. In particular, $a^3\Sigma^+$ molecular state, which is one of the subjects of research in this thesis, shows non-vanishing hyperfine structure and *Fermi contact interaction* is responsible for it.

As was described in Section 2.2, in Hund's cases the hyperfine interaction was not taken into account. Let's analyze the coupling appropriate for the $a^3\Sigma^+$ state of NaRb and NaCs molecules if nuclear magnetic moment is introduced into the coupling scheme. The appropriate Hund's case for the $a^3\Sigma^+$ state is (b). Then there are three possible hyperfine coupling schemes: $(b_{\beta N})$, $(b_{\beta S})$ and $(b_{\beta J})$ (here β indicates that the total nuclear spin $\mathbf{I}$ couples to $\mathbf{N}$, $\mathbf{S}$, and $\mathbf{J}$, respectively, rather than to the internuclear axis). Case $(b_{\beta N})$ is rarely observed because both $\mathbf{S}$ and $\mathbf{J}$ are usually associated with much larger magnetic moments than $\mathbf{N}$, so $\mathbf{I}$ couples primarily to $\mathbf{S}$ or $\mathbf{J}$ rather than to $\mathbf{N}$. Cases $(b_{\beta S})$ and $(b_{\beta J})$ are the two important hyperfine coupling schemes in the case (b) limit. Whether a state belongs to case $(b_{\beta S})$ or $(b_{\beta J})$ depends on the relative strength of the coupling of $\mathbf{S}$ to $\mathbf{I}$ or $\mathbf{N}$, or, in other words, whether Fermi contact or spin-rotation interaction is dominant.

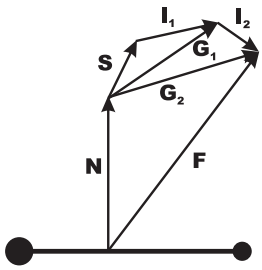

Figure 2.2. Coupling scheme for Hund's $(b_{\beta S})$ case

For the NaRb and NaCs $a^3\Sigma^+$ state because of the spherically symmetric s atomic orbitals composing the $a^3\Sigma^+$ state, the spin-spin and spin-rotation interaction are expected to be very small and the Fermi contact interaction to dominate in the a state. In this case it is appropriate to employ the Hund's case $(b_{\beta S})$ (see Fig. 2.2). The total electron spin $\mathbf{S}$ and nuclear spin $\mathbf{I}_1$ are coupled to form $\mathbf{G}_1$, then $\mathbf{G}_1$ and nuclear spin $\mathbf{I}_2$ are coupled to form $\mathbf{G}_2$, and finally $\mathbf{G}_2$ and $\mathbf{N}$ couple to give $\mathbf{F}$. Here $\mathbf{N}$ is the sum of the rotational angular momentum and the electronic orbital angular momentum. However, at high N-values a deviation from the pure $(b_{\beta S})$ case can take place due to the spin-rotation interaction. Such deviations can happen also due to perturbations [38].

Nuclear spins are coupled in the order of decreasing coupling energies. Hence for NaRb molecule $\mathbf{I}_1$ is for $^{85(87)}$Rb and $\mathbf{I}_2$ for Na, and for NaCs $\mathbf{I}_1$ is for Cs and $\mathbf{I}_2$ for Na, because nuclear spins are $I(^{23}\mathrm{Na}) = 3/2$, $I(^{85}\mathrm{Rb}) = 5/2$, $I(^{87}\mathrm{Rb}) = 3/2$, $I(^{133}\mathrm{Cs}) = 7/2$.

2.8 Long-range behavior

If two atoms lie sufficiently far apart, that their electron clouds overlap negligibly, then one can ignore electronic coupling and fine-structure effects, an their interaction energy can be expanded as

$$U(R) = D - \sum_m \frac{C_m}{R^m} \tag{2.17}$$

where D is the energy at the potential asymptote, the powers m are positive integers, and the nature of the atomic species to which a molecular state dissociates determines which powers contribute to this

expansion. Perturbation theory yields explicit expressions for the C_m constants in terms of the properties of the isolated atoms and the symmetry of the particular molecular state.

The *first-order perturbation* theory contributions to (2.17) are terms corresponding to the electrostatic interactions between permanent electric moments (charge, dipole, quadrupole, ...) on the component species, and the associated inverse powers are the same as those occurring for the interaction between such charge distributions in classical physics.

The *second-order perturbation* theory interactions involve only *even* values of m, and are of two types. The first is the "*induction*" interaction between a permanent electric moment on one particle and the electron distribution on the other; terms of this type also have explicit classical analogs. The other type of second-order term is the non-classical "*dispersion*" interaction ($m \geq 6$), which may be thought of as arising when the instantaneous electric moment due to a momentary electron configuration on one species induces a moment on the other, and then interacts with it, with this interaction being averaged over the full electronic configurations. "Dispersion energy" terms contribute to all interactions between atomic systems. Eq. 2.17.

The term $\frac{C_6}{R^6}$ expresses the London dispersion energy. It corresponds to dipole-dipole interaction. Term $\frac{C_8}{R^8}$ appears from the dipole-quadrupole interaction, whereas $\frac{C_{10}}{R^{10}}$ term arises from quadrupole-quadrupole and dipole-octopole interaction.

R. Le Roy [39, 40] proposed to express the lower R limit (in literature refered to as *Le Roy radius*) of Eq. 2.17 validity as

$$R_{\mathrm{LR}} = 2\left[\sqrt{\langle r_e^2\rangle_a} + \sqrt{\langle r_e^2\rangle_b}\right], \tag{2.18}$$

where $\langle r_e^2\rangle_a$ is the expectation value of the square of the radius-vector of the electrons in the valence shell of atom a (in other words, the radius of the valence electron shell). At this distance the exchange energy is approximately 10% of the Coulomb energy.

It means that two atoms must be far apart enough so that the mutual distortion of their charge clouds is small and that the short-range interactions (the charge-overlap interaction, i.e. the Coulomb repulsion between the electrons, and exchange interaction imposed by the Pauli exclusion principle) are small compared to the long-range interactions. The criterion (2.18) has been widely adopted in the long-range analysis of various molecular states.

An accurate knowledge of long-range potential curves is crucial in the interpretation of new physical phenomena associated with ultracold atoms, such as cold collision dynamics, photoassociative ionization, fine- and hyperfine predissociation, and the stability of Bose–Einstein condensates. Attention is often centered on the values of the multipolar expansion dispersion coefficients used to characterize the long-range region of the potential at large internuclear distance R where the exchange energy is much smaller in magnitude than the Coulomb (dispersion) energy.

In long-range limit, where atomic overlap is small, the exchange energy for two S-atoms forming a molecule, is written as

$$E_{ex}(R) = 1/2[U_a(R) - U_{\mathrm{X}}(R)], \tag{2.19}$$

where $U_{\mathrm{X}}(R)$ and $U_a(R)$ are the potentials of the X and a states. Thus, when the two lowest electronic potentials of a diatomic molecule—the singlet $\mathrm{X}^1\Sigma^+$ state and triplet $a^3\Sigma^+$ state—are known precisely up to near dissociation, their potentials can be used to determine the exchange energy as a function of internuclear distance.

The exchange energy can be also estimated from the properties of individual atoms. The exchange interaction expression calculated using the surface integral method of Smirnov and Chibisov is [41, 42]

$$E_{ex}(R) = \pm J(A, B, \alpha, \beta, R) \cdot R^{[2/\alpha+2/\beta-1/(\alpha+\beta)-1]} \cdot e^{-(\alpha+\beta)R}, \tag{2.20}$$

where $\alpha = \sqrt{2I_a}$ and $\beta = \sqrt{2I_b}$ ($I_{a,b}$ – ionization energy of each atom in atomic units). The function $J(A, B, \alpha, \beta, R)$ can be expanded in a power series $\sum_n J_n R^n(\alpha - \beta)^n/n!$ with coefficients J_n expressed as integrals that must be solved numerically. The constants A and B are related to the size of the wave function of each atom in the region of interaction [64].

2.9 Empirical level energy expressions

2.9.1 Band constants

Energy of the rovibronic level $E(v,\, J)$ of the molecule in the $^1\Sigma$ state can be expressed using the so-called *band constants* – spectroscopic constants derived from the analysis of vibrational and rotational bands in the spectra[1].

$$E_{BC}(v,\, J) = G(v) + B_v[J(J+1)] - D_v[J(J+1)]^2 + H_v[J(J+1)]^3 + \cdots \equiv \sum_m K_m(v)[J(J+1)]^m \quad (2.21)$$

The first term in this equation is the vibrational energy $G(v)$. It also can be expressed as a polynomial, expanded over powers of $(v + 1/2)$:

$$G(v) = \omega_e(v+1/2) - \omega_e x_e(v+1/2)^2 + \omega_e y_e(v+1/2)^3 + \omega_e z_e(v+1/2)^4 + \cdots \quad (2.22)$$

The coefficients in (2.22) are called *vibrational constants*. The first of them ω_e is a classical oscillator frequency, but further coefficients $\omega_e x_e$, $\omega_e y_e$, etc. take into account the vibrational unharmonicity, therefore they are called *unharmonicity constants*. The rest terms in (2.21) describe the rotational energy and coefficients before $J(J+1)$ are called rotation constants. B_e is the inertial rotation constant and represents rotational energy of the rigid rotator (index e stands for its equilibrium value, see below). D_e, H_e, etc. – centrifugal distortion constants (CDC) in the equilibrium state. Corresponding constants for an arbitrary vibrational level are B_v, D_v, H_v, etc.

At small energies (small v and J values) vibrational and rotational motions are almost independent, but as energy grows their interaction must be taken into account. Mathematically, this is maintained by the dependence of rotational constants on vibrational quantum numbers:

$$\begin{aligned}
B_v &= B_e - \alpha_e(v+1/2) + \alpha_2(v+1/2)^2 - \alpha_3(v+1/2)^3 + \cdots & (2.23)\\
D_v &= D_e - \beta_e(v+1/2) + \beta_2(v+1/2)^2 - \beta_3(v+1/2)^3 + \cdots & (2.24)\\
H_v &= H_e - h_e(v+1/2) + h_2(v+1/2)^2 - h_3(v+1/2)^3 + \cdots, & (2.25)
\end{aligned}$$

where α_i, β_i, h_i are constants of rotation-vibration interaction. Equilibrium values of the rotational constants are:

$$\begin{aligned}
B_e &= \frac{\hbar^2}{2\mu R_e^2} & (2.26)\\
D_e &= \frac{4B_e^3}{\omega_e^2} & (2.27)\\
H_e &= \frac{2D_e}{3\omega_e^2}\left(12B_e^2 - \alpha_e\omega_e\right) & (2.28)
\end{aligned}$$

where R_e denotes the position of the potential minimum.

2.9.2 Dunham constants

Dunham [43] has calculated the energy levels of a vibrating rotor in the quasiclassical Wentzel-Kramers-Brillouin (WKB) approximation for any potential which can be expanded as a powers series of $(R - R_e)$ in the neighborhood of the potential minimum:

$$U(\xi) = a_0\xi^2(1 + a_1\xi + a_2\xi^2 + \cdots), \quad (2.29)$$

[1] For $\Omega \neq 0$ states $J(J+1)$ should be replaced with $J(J+1) - \Omega^2$

where $\xi = \frac{R-R_e}{R_e}$. The centrifugal term is also expanded as

$$U_r(\xi) = B_e J(J+1)(1 - 2\xi + 3\xi^2 - 4\xi^3 + \cdots) \tag{2.30}$$

This type of potential is essentially a Taylor series expansion beyond a harmonic oscillator leading term, and, if enough terms are included, it can give an arbitrarily accurate representation of a potential over any finite range of R. Dunham derived expressions for spectroscopic constants in terms of the coefficients in the expansion. Thus Dunham provided a very simple and convenient method for computing spectroscopic constants from a theoretical potential energy curve. The parameters a_0, a_1, a_2, ... are obtained by a least squares fit of the theoretical curve to the Eq. (2.29) and then theoretical spectroscopic constants can be calculated for comparison with the empirical values.

However, the power series expansions (2.29) and (2.30) are not suitable for the inverse process of determining an "experimental" potential curve from known spectroscopic constants. This is because of their very poor convergence. The expansion (2.30) converges only for $|\xi| < 1$, that is for $R < 2R_e$, and in practice it is found that the useful range of convergence is much less than this.

Dunham showed that in the case of a such power series expansion the energy levels can be written in the form

$$E(v,\, J) = \sum_{l,m} Y_{lm}(v + 1/2)^l (J(J+1))^m \tag{2.31}$$

where Y_{lm} are called Dunham constants. By comparison of (2.31) with (2.21) one can derive correspondence between Y_{lm} and band constants:

$$\begin{array}{lll} Y_{1,0} = \omega_e & Y_{0,1} = B_e & Y_{0,2} = -D_e \\ Y_{2,0} = -\omega_e x_e & Y_{1,1} = -\alpha_e & Y_{1,2} = \beta_e \\ Y_{3,0} = \omega_e y_e & Y_{2,1} = \alpha_2 & Y_{2,2} = -\beta_2 \\ \cdots & \cdots & \cdots \end{array}$$

However, it was found by Dunham that these relations are true only if B_e/ω_e is small, which is usually the case. According to Dunham's formulae there is also a non-vanishing term $Y_{0,0}$. For excited states this term is replaced by a constant term T_e. The value of potential minimum $U(R_e)$ however differs from T_e by the value of $Y_{0,0}$ which in terms of the other constants may be written as

$$Y_{0,0} = \frac{B_e}{4} + \frac{\alpha_e \omega_e}{12 B_e} + \frac{\alpha_e^2 \omega_e^2}{144 B_e^3} - \frac{\omega_e x_e}{4}. \tag{2.32}$$

Dunham constants are widely used by spectroscopists thanks to relative easiness of calculation and direct physical meaning of several first coefficients.

The fact that Dunham's energy level formula is based on the concept of potential energy curve provides many self-consistency checks between molecular constants, for example, the *Kratzer relation*,

$$Y_{0,2} = -\frac{4Y_{0,1}^3}{Y_{1,0}^2}, \tag{2.33}$$

which is valid for harmonic or Morse potentials (see Section 2.10.2), and the *Pekeris relation*,

$$Y_{1,1} = \frac{6Y_{0,1}^2}{Y_{1,0}} \left[1 - \sqrt{\frac{-Y_{2,0}}{Y_{0,1}}} \right], \tag{2.34}$$

which is valid for a Morse potential.

If there are several isotopomers the question appears of appropriate transformation of the molecular constants. In the simplest treatment, independent sets of Dunham molecular constants are obtained

for each isotopomer. However, this involves considerable redundancy, since the resulting constants for different isotopomers are known to be interrelated:

$$Y_{lm}^{\beta} = \sum_{l,m} Y_{lm}^{\alpha} \left(\frac{\mu_\alpha}{\mu_\beta}\right)^{m+\frac{l}{2}} = \sum_{l,m} Y_{lm}^{\alpha} \rho^{2m+l}, \tag{2.35}$$

where Y_{lm}^{α} – Dunham constants of α isotopomer;
$\mu_\alpha = \frac{M_A^\alpha M_B^\alpha}{M_A^\alpha + M_B^\alpha}$ – reduced mass of α isotopomer;
Y_{lm}^{β}, μ_β – Dunham constants and reduced mass of β isotopomer.

2.9.3 RKR potential

With the expressions for the vibrational energy $G(v)$ and inertial rotational constant $B(v)$ obtained from empirical fits, the potential energy curve of the molecular state may be determined through the Rydberg-Klein-Rees (RKR) method [44], which is based on the first-order WKB approximation. RKR method allows to obtain the classical turning points of the nuclear motion without making any assumptions about the potential curve. This gives the possibility to construct the potential up to the highest observed vibrational level. RKR method is based on Klein integrals:

$$R_+(v) - R_-(v) = 2\sqrt{\frac{\hbar^2}{2\mu}} \int_{v_{\min}}^{v} \left[G(v) - G(v')\right]^{-\frac{1}{2}} dv', \tag{2.36}$$

$$\frac{1}{R_-(v)} - \frac{1}{R_+(v)} = 2\sqrt{\frac{2\mu}{\hbar^2}} \int_{v_{\min}}^{v} B(v') \left[G(v) - G(v')\right]^{-\frac{1}{2}} dv', \tag{2.37}$$

from which the outer and inner classical turning points $R_+(v)$ and $R_-(v)$ can be determined. $v_{\min}$ is the extrapolated value of the vibrational quantum number at the potential minimum.

2.10 Direct Potential Fit Analysis

It is seldom possible actually to solve the electronic wave equation, therefore it is customary to use an empirical expression for $U(R)$. So, *one of the main spectroscopical tasks is to restore the potential energy curve (PEC) from the observations.* The most widely used method for a long time was construction of RKR potential from Dunham molecular constants. This method however has several important disadvantages:

1. Method is based on the first-order WKB approximation, which is accurate only for heavy molecules,
2. RKR is defined only in turning points of vibrational motion and does not contain information about extrapolation in the region not covered by the experimental data,
3. It fails for "exotic potentials", such as double minimum potentials,
4. A lack of self-consistency in vibrational and rotational constants due to strong inter-parameter correlation in the Dunham expansion can result in unphysical bends of the RKR potential.

As an alternative, various fully quantum mechanical techniques have been developed, providing determination of PECs directly from the experimental data—*direct potential fit* (DPF) analysis. These methods compare observed transition energies with eigenvalue differences calculated numerically from an effective radial Schrodinger equation (2.4) for a parameterized potential energy function and use a least-squares (LS) fit to optimize the values of those potential function parameters.

For a wide variety of cases, this approach has been shown to represent the experimental data with equivalent accuracy and usually much more compactly than do conventional analyses based on fits to empirical level energy expressions.

2.10.1 Pointwise Potentials

In the earliest applications of the DPF approach the PEC was represented by a polynomial-corrected pointwise potential (PCPP)[2]. It was proposed in 1975 by Kosman and Hinze [46] and in 1977 by Vidal and Scheingraber [47] as a fully quantum mechanical method for defining an accurate potential energy curve of a diatomic molecular state. In literature this method is often mentioned as IPA (Inverted Perturbation Approach) method because the basic idea of it is to find such a correction $\delta U(R)$ to initial approximate potential $U_0(R)$, that the set of eigenvalues $\{E_{vJ}\}$ obtained by solving the Schrödinger equation with $U_0(R) + \delta U(R)$ will agree with the set of experimental eigenvalues $\{E_{vJ}^{expt}\}$ in the LS sense.

For an efficient and rapidly converging method the functional form of the correction function $\delta U(R)$ is of crucial importance. Most conveniently, $\delta U(R)$ can be described as a linear superposition of some functions $f_i(R)$:

$$\delta U(R) = \sum_i c_i f_i(R) \tag{2.38}$$

In this case the coefficients c_i are given by a system of linear equations:

$$\delta E_{vJ} = \sum_i c_i \langle \Psi_{vJ}^0 | f_i(R) | \Psi_{vJ}^0 \rangle, \tag{2.39}$$

where Ψ_{vJ}^0 are WFs obtained with the initial potential $U_0(R)$. This system is generally overdetermined and can be solved by a LS method.

As an appropriate choice of $f_i(R)$ functions, Kosman and Hinze [46] have selected Legendre polynomials $P_i(x)$. Vidal and Scheingraber [47] proposed to use functions $f_i(R) = P_i(R)\exp(-R^{2n})$, with $1 \leq n \leq 5$. This modification was made in order to avoid unphysical oscillations of the potential outside the R_{min} and R_{max}, determined by the last E_{vJ}^{expt} observed. For systems with small reduced masses that approach yielded significant improvements over the accuracy of RKR potentials. However, the polynomial-type correction functions used in most applications cannot be extrapolated in a realistic manner, so this approach provides no sensible description of the system beyond the range of internuclear distances used in the analysis.

PCPP approach is also model-dependent and is not flexible enough when potentials are of "exotic shape", e.g., double well or shelf state potentials. Facing this problem, A. Pashov and coworkers in 2000 [48] proposed to express the correction to the potential curves in a set of N equidistant[3] points $\{R_i, u_i\}$ connected with a cubic spline function. This method is often called a modified IPA method in literature, and potential energy function is further referenced to as spline-pointwise potential (SPP), as proposed in Ref. [45].

It is possible to show [48, 49, 50] that the correction appears as a linear combination of known functions $S_i(R)$ with coefficients u_i:

$$\delta U(R) = \sum_i S_i(R) u_i \tag{2.40}$$

$S_i(R)$ may be considered as a measure of the strength of the "contribution" of u_i to the value of $\delta U(R)$. In the grid points (R_1, R_2, ..., R_i, ...) the value of $S_i(R)$ is always zero except the case of the for $R = R_i$, where it is 1.

From Eq. (2.40) we derive a system of linear equations

$$E_k = E_k^0 + \sum_i \langle \Psi_k^0 | S_i(R) | \Psi_k^0, \rangle \Delta u_i, \tag{2.41}$$

where Δu_i is the correction to the ith fitting parameter. Replacing E_k with E_k^{expt} provides a set of M linear equations (M denotes the number of experimental levels) with N unknowns (where N is the number of the fitted parameters, i.e. grid points).

[2] Terminology suggested by Y.H. Huang and R.J. Le Roy in Ref. [45].

[3] Initially the method was developed for the case of equidistant grid of points, but later generalized to irregular spaced grid.

Expansion (2.40) is very flexible and allows smooth and accurate interpolation of a variety of functions. It imposes no limitations on the shape of the fitted curve and therefore can be applied to both regular and irregular potential energy curves. The flexibility, however, can often result in unphysical oscillations of the fitted potential curve. This happens usually in the regions which are not sufficiently described by the experimental data. To handle the problem the *Singular Value Decomposition* (SVD) [51] is used for minimization of the merit function $\chi^2(U)$. This method allows to select such parameters which can not be determined from the fit (have huge standard deviation and change value from minus infinity to plus infinity) and set their values to zero. In our case it means that grid points which will have small influence on eigenenergies will be fixed at some initial values. The strength of the SVD is governed by a singularity parameter ζ. If $\zeta = 0$, the SVD solution will not differ from the usual LS method. Increasing ζ we can monitor behavior of χ^2 and we stop increase of ζ when χ^2 goes beyond some limit.

Recently an additional tool for providing a smooth solution was suggested [50]. Generally, the usual way of obtaining a smooth fitted function $f(R, \mathbf{a})$ is to add to the merit function $\chi^2(\mathbf{a})$ a regularizing functional $H(\mathbf{a})$ which is responsible for the smoothness of the solution and to minimize the sum

$$\chi^2(\mathbf{a}) + \lambda^2 H(\mathbf{a}), \tag{2.42}$$

where λ is a parameter used to tune the degree of regularization. Possible forms of $H(\mathbf{a})$ can be found in [51]. One of them is :

$$H(\mathbf{a}) = \int_{R_1}^{R_2} [f''(R, \mathbf{a})]^2 dR. \tag{2.43}$$

By minimizing the integral of the square of the second derivative, one sets the additional condition that the fitted function should be as close to a straight line as possible between R_1 and R_2. Since in the method described the fitted potential is defined as a cubic spline function drawn between given grid points (R_i, u_i), the second derivative $U''(R, \mathbf{u})$ between these points is a linear function of R. Therefore, a simplified form of the regularizing functional is introduced:

$$H(\mathbf{u}) = \sum_i [U''(R_i, \mathbf{u})]^2, \tag{2.44}$$

where $U''(R_i, \mathbf{u})$ denotes the second derivative of the potential in a grid point R_i.

When $\lambda = 0$, the system (2.41) remains unchanged, i.e., no regularization is imposed. Increasing λ results in flattening of the potential in competition with the initial condition defined by Eq. 2.41. Again a compromise between smoothness and χ^2 must be searched.

A key strength of the SPP form is its model-free nature − it can treat any shape of potential energy curve without the intrinsic limitations imposed by choice of a particular analytic form. Construction of SPP has been successfully applied to analyses of data for a number of standard (normal single-well potential) and nonstandard (double-minimum, shelf-state, or barrier potential) cases [52, 53, 54, 55, 56, 57, 58, 59] and has been widely applied in the present work.

2.10.2 Analytic Potentials

A wide range of analytic functions for representing ordinary single-minimum potential energy curves have been proposed over the years. However, exact analytic expressions for vibrational and rotational level energies can be obtained only for several of them. These functions in simplest cases are defined by two or three parameters which typically characterize the well depth D_e, the position of the potential minimum R_e, and the well shape. Let's consider several kinds of potentials that are widely used as the simplest models or as the basis of flexible many-parameter potential, and also the potentials which were applied in this work.

Morse Potential

It is a sum of attractive and repulsive exponential terms

$$U_{Morse}(R) = D_e \left[e^{-2\beta(R-R_e)} - 2e^{-\beta(R-R_e)} + 1 \right] = D_e \left[1 - e^{-\beta(R-R_e)} \right]^2 \tag{2.45}$$

whose vibrational eigenenergies are:

$$G(v) = \omega_e(v + 1/2) - \omega_e x_e (v + 1/2)^2 \tag{2.46}$$

This potential is widely used, but its main disadvantage is that exponential form doesn't fit the inverse-power behavior of long-range potentials.

Lennard-Jones (m, n) Potentials

This is a family of potentials with inverse-power attractive and repulsive terms

$$U_{LJ}(R) = \frac{C_m}{R^m} - \frac{C_n}{R^n} + D_e = D_e \left[\frac{n}{m-n} \left(\frac{R_e}{R} \right)^m - \frac{m}{m-n} \left(\frac{R_e}{R} \right)^n + 1 \right] \tag{2.47}$$

where $m > n$ are both positive integers. This potential doesn't have analytic expressions for vibrational and rotational energies, whereas it is widely used because of the simplicity of the form (especially for fixed $m = 2n$) and because it allows one to provide the correct long-range behavior on the potential by setting n equal to the power of the first non-zero term in Eq. 2.17.

Generalized Morse-Type Potential Functions

This is a generalization of the Morse function where the exponent parameter is expanded in a power series in some R–dependent expansion variable:

$$\beta = \beta(R) = \beta_0 + \beta_1 y(R) + \beta_2 y(R)^2 + \beta_3 y(R)^3 + \cdots \tag{2.48}$$

The great advantage of this functional form is that the Morse potential structure gives the basic shape of the potential, and only modest smooth variations in $\beta(R)$ are required to give a flexibility in the describing details of the shape. In contrast, in simple power-series potential forms the polynomial expansion is responsible both for the basic structure and for accounting for details of the shape.

Dunham's power series expansion

– see Section 2.9.2.

Morse-Lennard-Jones[4] Potential Function

In 2000 [60] R. Le Roy and P. G. Hajigeorgiou introduced a new analytical model for the internuclear potential energy function of a diatomic molecule which has the same flexibility and compactness yielded by the variable-exponent Morse-type potentials, but which can also incorporate the correct theoretically known inverse-power long-range behavior. The new model is a kind of a generalization of the prototypical Lennard-Jones $(2n, n)$ function with the form

$$U(R) = D_e \left[1 - \left(\frac{R_e}{R} \right)^n \right]^2, \tag{2.49}$$

[4] In the original work [60] this function was called the "modified Lennard-Jones oscillator" potential because of a wish to emphasize the inverse-power long-range behavior. Later the authors redefined the leading term in the acronym MLJ.

It is a qualitatively correct model for a single minimum diatomic molecule internuclear potential energy function, but does not have a flexibility required to represent accurately extensive experimental information. That's why the function was modified in the following way:

$$U(R) = D_e \left[1 - \left(\frac{R_e}{R}\right)^n \phi(R)\right]^2, \tag{2.50}$$

where $\phi(R)$ is the modifying function, which is used in order to bring the potential into a better correspondence with the experimental data. Analysis showed that this function can not be efficiently represented with the power expansion because of its shape and relatively rapid variation with internuclear separation. In turn, its exponential representation $\phi(R) = \exp[-\beta_{MLJ}(z) \cdot z]$, where $z = \frac{R-R_e}{R+R_e}$ is a generalized variable, appeared to be more suitable. That's why the MLJ potential was introduced in the form

$$U_{MLJ}(R) = D_e \left[1 - \left(\frac{R_e}{R}\right)^n e^{-\beta_{MLJ}(z)z}\right]^2. \tag{2.51}$$

In the limit $R \to \infty$ ($z \to 1$), the MLJ potential takes the form

$$U(R) = D_e - 2D_e \left(\frac{R_e}{R}\right)^n e^{-\beta_\infty} = D_e - \frac{C_n}{R^n}. \tag{2.52}$$

An appropriate choice of the power n imposes the correct theoretically predicted limiting long-range functional behavior.

The constant β_∞ in Eq. 2.52 indicates that $\beta_{MLJ}(z)$ must be expressed as a function which will naturally approach a finite limit as $R \to \infty$ ($z \to 1$). The simplest way of doing this is to write it as a power series in z:

$$\beta_{MLJ}(z) = \sum_{m=0}^{M} \beta_m z^m, \tag{2.53}$$

so that

$$\lim_{z\to 1} \beta_{MLJ}(z) = \sum_{m=0}^{M} \beta_m. \tag{2.54}$$

MLJ potential has been successfully tested for several molecular states, e.g. Rb_2 ground state potential [62] and has been also implemented in the current research.

In Ref. [63] a new, flexible potential model has been proposed by E.Tiemann and coworkers. The potential is represented as a truncated expansion over analytic functions:

$$U(R) = \sum_{i=0}^{n} a_i \left(\frac{R - R_m}{R + bR_m}\right)^i, \tag{2.55}$$

where a_i, b and R_m are parameters (R_m is close to the equilibrium distance). The parameter b models the very different steepness of the potential inside and outside R_e and is chosen such that the number of a_i coefficients needed to represent the potential is minimized.

Chapter 3

Experimental setup

In this Section the experimental setups used in the present experiments performed in the laboratories at the University of Latvia and the University of Hannover will be described.

3.1 Experimental setup at the University of Latvia

Laser induced fluorescence (LIF) was excited by an Ar^+ laser (Spectra Physics 171) operating in a single-mode regime at 514.5 nm wavelength. LIF has been dispersed by a double monochromator DFS-12 with 1200 lines/mm diffraction gratings and 5 Å/mm inverse dispersion in the first diffraction order, providing at reasonable slit width the 0.2 Å spectral resolution. Fluorescence progressions have been detected up to 680 nm by a FEU-79 photomultiplier operating in a photon counting regime. Simultaneously detected Ar and Ne discharge lines have been used as frequency standards. The average uncertainty of LIF line positions was estimated as ca. 0.1 cm^{-1}. A scheme of the setup can be seen in Fig. 3.1.

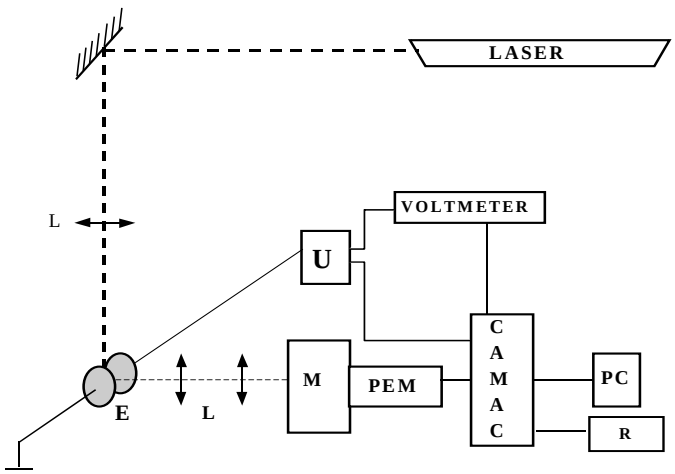

Figure 3.1. A scheme of the LIF experimental setup in Riga. E – cell with electrodes, M – monochromator, PEM – photoelectric multiplier, CAMAC – data acquisition interface, R – recorder, PC – computer, U – voltage supply, L – lenses.

NaRb molecules were formed from a 4:1 mixture (by weight) of natural Rb (containing 72% of ^{85}Rb and 28% of ^{87}Rb) and ^{23}Na metals in an alkali-resistant glass thermal cell at temperature ca. 550 K. At the initial stage of the experiment a cell with electrodes and connected to the vacuum pump was

used. Applying of electric field [65] allowed us to distinguish between the $^1\Pi - {}^1\Sigma$ and $^1\Sigma - {}^1\Sigma$ doublet progressions. Then the evacuated cell not connected to the vacuum system was used. The cell was heated in a two part resistance oven, maintaining approximately $20\,^0$C higher temperature in the upper part than in the lower one in order to prevent metal condensation in the upper part of the glass cell.

3.2 Experimental setup at the University of Hannover

In this Section the LIF experimental setup used in the studies performed at the University of Hannover is described. A diagram of the setup can be seen in Fig. 3.2. A laser beam passes through the sample in the heat-pipe oven (or metal cell) and a fluorescence is collected in the direction opposite to the propagation of the laser beam and then focused into the input aperture of IFS 120 HR Fourier-transform spectrometer. Let us describe the main parts of the experiment in more detail.

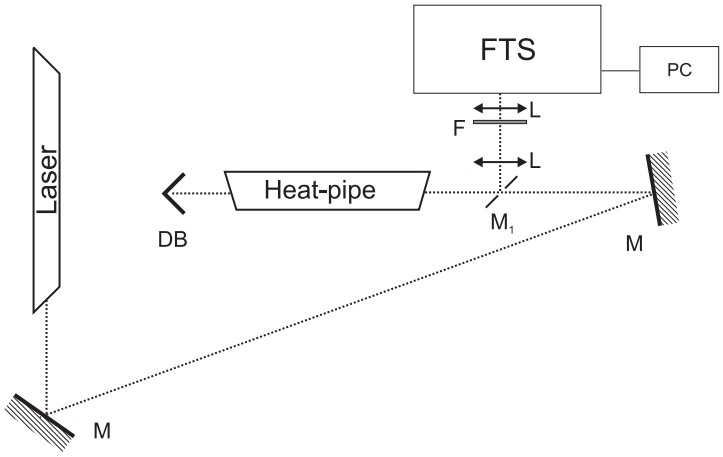

Figure 3.2. A scheme of the LIF experimental setup in Hannover. FTS – Fourier-transfrom spectrometer, M – mirrors, M_1 – mirror with slit, L – lenses, F – optical filter, DB – dark box, PC – computer.

3.2.1 Preparation of the molecules

For preparation of the molecules a heat-pipe oven or a metal cell were used. A single section heat-pipe (HP) cell is made of a stainless steel tube. A commercial oven from the Carbolite company was used for heating the cell. It allows to reach temperatures close to 1500 K and can be used to heat a tube with diameter smaller than 60 mm. The pipe is 960 mm long, has a diameter of 34 mm and a wall thickness of 2 mm. The inner part of the heat-pipe is covered by a fine metal mesh. The alkali metal is placed near the center of the tube. Each end of the tube is closed by a glass window with antireflection coating. The end parts are water cooled. Thus during a heating a micro-climate develops in the tube, and alkali metal atoms evaporate out and diffuse into the cold zones where condensation occurs. The liquid metal is then sucked back towards the center by surface tension forces between the metal atoms and the mesh. In order to prevent atom condensation on the windows, the buffer gas is used. As the buffer gas, we used argon with typical pressure of few millibars (mbar). A schematic picture of the heat-pipe can be seen in Fig. 3.3.

The NaRb molecules were produced in a heat-pipe oven by heating 5 g of Na (purity 99.95%) and 10 g of Rb (purity 99.75%, natural isotopic composition) from Alfa Aesar. The oven was operated at temperatures between 560 K and 600 K and typically with 2 mbar of Ar buffer gas. The heat-pipe was in operation for about 120 hours without refilling and at the end of the experiment it was still in good

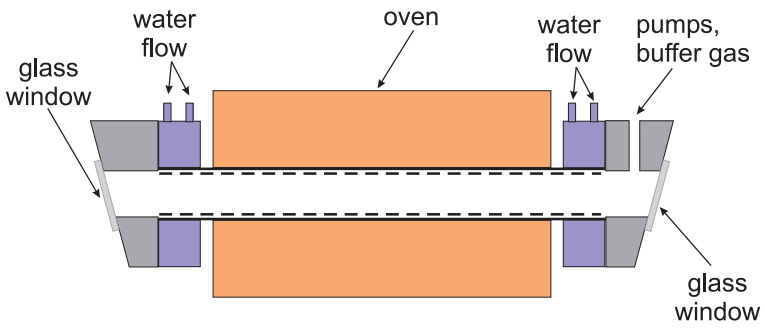

Figure 3.3. A scheme of a heat-pipe.

operation condition. After the end of experiments the heat-pipe was filled with argon and disconnected from the vacuum system. After half a year it was successfully operated again.

For experiments with NaCs in order to ensure safe operation with Cs, a metal cell was designed (see Fig. 3.4). The 300 mm long cell has approximately 30 mm in diameter and CF flanges are welded at both ends for mounting sapphire windows (Varian Vacuum Technologies). A metal container is appended at the side of the cell for two ampullae with 1 g Na and 1 g Cs and closed by a CF flange. The end of the Na ampulla was cut just before the loading. The cell is connected to the vacuum apparatus via a metal bellows-all-welded valve from Swagelock welded to the cell. In this configuration the whole cell (including the windows, container and the metal valve) can be heated up to 700 K. After the cell was pumped for several days at temperatures up to 400 K, low enough for not losing Na, the Cs ampulla was broken by shaking the cell. The advantages of using a metal cell compared to traditional heat-pipe ovens are safe procedures for loading, possibility for operation with small amounts of metals, and also without presence of a buffer gas. Usually the cell was heated to $550 - 600$ K and operated without buffer gas. Unfortunately, after about 20 hours of operation a leak in the sapphire windows of the cell was found. It might have happened due to general non-resistance of the welding between the sapphire and the metal of CF flange to alkali metal vapors.

For longer experimental studies of NaCs a heat-pipe oven (see Fig. 3.5) was designed as described above which was provided with a short metal container welded to the central part of the pipe. A 5 g glass ampulla of Cs from Alfa Aesar was loaded in the container and closed with a CF flange. About 10 g of Na were loaded in the heat-pipe in a usual way. After several days of conditioning, the Cs ampulla was broken by shaking the heat-pipe oven. Since the container was mounted close to the pipe and heated simultaneously with it up to the same temperature, the heat-pipe was operated in a simple single-section heat-pipe regime. The oven was operated at temperatures between 560 K and 600 K and typically with 3 mbar of Ar buffer gas. The oven was in operation for about 50 hours without refilling and at the end of the experiment it was still in good working condition. Like NaRb heat-pipe after the end of experiments it was filled with argon and disconnected from the vacuum system. After 6 months, and afterwards after 12 months it was successfully operated again and no metal refilling appeared to be necessary.

The heat-pipes of construction designed at the University of Hannover appeared to be very efficient for work with alkali-metal dimers. Their important advantages are rather simple design, safe operation with metals and long lifetime.

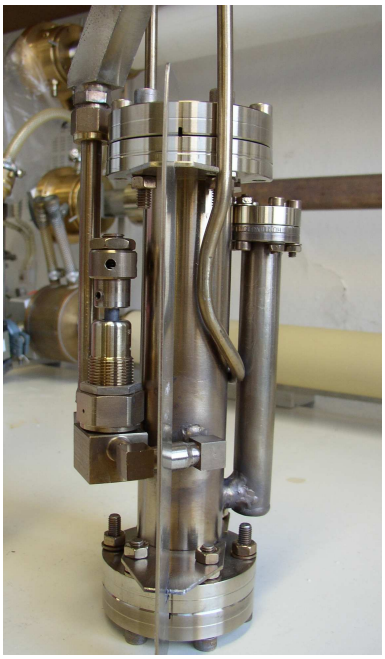

Figure 3.4. Metal cell used for experiments with NaCs.

Figure 3.5. Oven with the NaCs heat-pipe.

3.2.2 Lasers

Several different types of cw lasers were used in the present experiments.

1. Ar^+ laser (Spectra Physics BeamLok 2060) operated at lines 514.5, 501.7, 496.5, 488.0, 476.5 nm in a multimode (typical power 0.5-3 W) and a single mode regime (typical power 100-500 mW).
2. Tuneable single-mode frequency doubled Nd:YAG[1] laser with a typical output power of 70 mW at 532.2 nm. Tuning range app. 3 cm^{-1}.
3. Ring dye laser Coherent 699-21 with Rhodamine 6G dye (tuning range 550–590 nm, peak at 560 nm) with power ca. 100 mW, pumped by Nd:YAG frequency doubled laser (Verdi, Coherent).
4. Linear dye laser Coherent 599 with DCM dye (tuning range 610–695 nm, peak at 645 nm) with power ca. 70 mW, pumped by Ar^+ laser.

3.2.3 Fourier-Transform Spectrometer

Fourier-Transform Spectrometer (FTS) is a dual-beam interferometer, which is most frequently of the Michelson type, as shown in Fig. 3.6. If the arms of the interferometer have equal lengths, the path

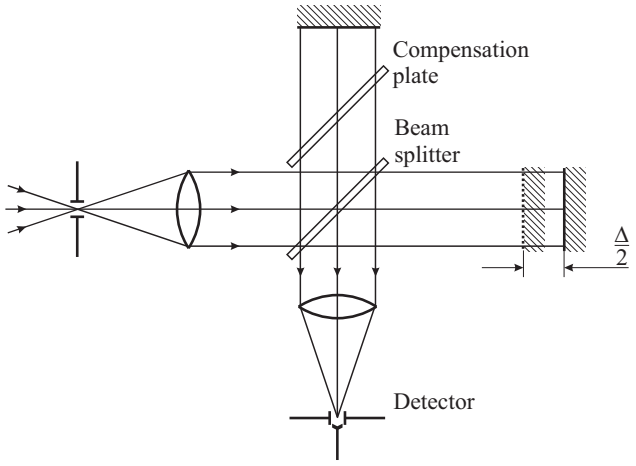

Figure 3.6. Principal Fourier spectrometer scheme based on the Michelson interferometer.

difference between the two interfering beams is zero. If one mirror is shifted by $\Delta/2$, an optical path difference of Δ is introduced. For the case of monochromatic radiation with frequency σ in wavenumbers and equally intense beams the intensity at the detector is

$$I(\Delta) = I_0(1 + \cos(2\pi\sigma\Delta)) \tag{3.1}$$

If the light source emits a spectrum $B(\sigma)$ we then obtain

$$I(\Delta) = \int_0^{+\infty} B(\sigma)(1 + \cos(2\pi\sigma\Delta))d\sigma = \frac{I(0)}{2} + \int_0^{+\infty} B(\sigma)\cos(2\pi\sigma\Delta)d\sigma, \tag{3.2}$$

where $I(0) = \int_0^{+\infty} B(\sigma)d\sigma$.

[1] Nd:YAG stands for neodymium yttrium aluminum garnet

After applying the theorems of Fourier analysis we get that

$$B(\sigma) = const \int_0^{+\infty} \left[I(\Delta) - \frac{I(0)}{2} \right] \cos(2\pi\sigma\Delta) d\Delta, \tag{3.3}$$

which is called the *main integral equation* of the Fourier-transform spectroscopy. It expresses the fact, that spectrum $B(\sigma)$ can be calculated as the Fourier transform of the interferogram $\left[I(\Delta) - \frac{1}{2}I(0)\right]$ (Sometimes only I(Δ) is called interferogram). The interferogram has many similarities to a hologram. Every part of it contains information on the whole structure, but high resolution is achieved only when a large part of it is utilized. One of the great advantages of FTS is that all spectral lines are recorded at the same time (the *multiplex* or *Felgett advantage*). Further, a FTS has a comparatively high light collecting efficiency, since it does not require narrow slits for the above-mentioned reasons (the *Jaquinot advantage*). Spectrometers of that kind have a very good signal-to-noise ratio and instruments with a resolution of $R = 10^7$ can be constructed. The movement of a mirror is controlled by fringes from a He-Ne laser.

In practice, the movable mirror can only be moved over a limited distance (typically about 1 m or more) and therefore the upper integration limit in Eq. 3.3 is finite. Such a limited integration gives rise to side maxima of the spectral lines. Using a mathematical trick, which involves the multiplication of the integrand in (3.3) by a particular function, the unwanted maxima can be suppressed. However, this procedure, which is called *apodization*, gives rise to broader spectral lines. The simpliest apodization functions are boxcar and triangular ones.

Michelson was fully aware of the spectroscopic potential of his interferometer, but the lack of sensitive detectors and nonexistence of computers for performing Fourier-transform algorithms became insurmountable barriers for its practical implementation. That's why practical Fourier-transform spectroscopy appeared only in the early 1950s. Its development was greatly aided by the invention of the "fast Fourier transform" algorithm. Today, commercial Fourier-transform spectrometers are widely available and used for spectroscopy in many diverse disciplines.

In the present work we used the Fourier-Transform Spectrometer IFS 120 from Bruker Optics. It operates (with appropriate change of optics and detectors) in a spectral range from 63200 cm^{-1} in the ultraviolet region to 450 cm^{-1} in the infrared region. The instrument allows to obtain relative accuracy better than $0.5 \cdot 10^{-7}\sigma$ and an absolute accuracy better than $5 \cdot 10^{-7}\sigma$, where σ is a frequency in wavenumbers. In the region of 20000 cm^{-1} it corresponds to 0.001 cm^{-1} and 0.01 cm^{-1} accuracies, respectively.

Fourier spectrometer IFS 120 is operated with the help of OPUS software, which allows one to set the scan parameters (resolution, aperture, frequency range, number of scans, electrical filters, apodization function, etc.), initializes measurement, performs the Fourier transformation of the interferogram and allows further data processing. This model of the Fourier spectrometer has a useful tool of operation in "Preview mode", which makes possible to visualize a low-resolution spectrum in several seconds. This is especially important for searching the signal in an unexplored frequency region.

The LIF signal was detected with a Hamamatsu R928 photomultiplier tube (range of sensitivity $54000 - 11100$ cm^{-1}) or a silicon diode (range of sensitivity $25000 - 9000$ cm^{-1}) depending on the desired wavelength region. The scanning path of the spectrometer was set to reach a typical resolution of 0.0115–0.03 cm^{-1} and the typical number of scans for averaging varied between 10 and 20. In order to avoid the illumination of the detector by the He-Ne laser, used for calibration of the spectrometer, a NOTCH interference filter with 8 nm full width at half maximum was introduced. For better signal-to-noise ratio some spectra were recorded by limiting the desired spectral window with colored glass or interference filters.

Chapter 4

NaRb molecule

4.1 Background

Among heteronuclear alkali dimers, the NaRb molecule is relatively little known. First experiments with NaRb were made in 1928 by Walter and Barratt [66] who found an absorption spectrum of the NaRb molecule in the green region 18404-18753 cm^{-1}. In 1936 Kusch [67] found a new band system of NaRb in the red region 15778-16678 cm^{-1}. This system was assigned as a $^1\Pi - ^1\Sigma^+$ transition and the vibrational constants ω_e and $\omega_e x_e$ of both $X^1\Sigma^+$ ground state and the $^1\Pi$ excited state were determined.

The next experiments with the NaRb molecules were made only in 1981 [68]. They were the first in a series of measurements in NaRb performed in the Prof. Hajime Katô group in Japan. In Ref. [68] the LIF spectra of NaRb, excited with the He-Ne, Kr^+ and Ar^+ lasers were recorded. Green band system in 20000-17000 cm^{-1} region was assigned as the $D^1\Pi - X^1\Sigma^+$ transitions, but red band system in 17000-14000 cm^{-1} as $B^1\Pi - X^1\Sigma^+$. Spectroscopic constants and dissociation energies of the $X^1\Sigma^+$, $B^1\Pi$ and $D^1\Pi$ states were obtained. A few rovibronic levels of the $D^1\Pi$ state with vibrational quantum numbers $v' = 0 - 13$ and rotational quantum numbers between $J' = 11$ and 100 were studied. Molecular constants for the bottom of the $D^1\Pi$ state potential were estimated for the first time from the transition frequencies in the D–X LIF spectra as well as their intensity distributions.

The first high-resolution studies of NaRb were made in 1991 [69]. $^{23}Na^{85}Rb$ $B^1\Pi(v' = 0 - 12) \leftarrow X^1\Sigma^+(v'' = 0 - 6)$ transitions were studied using the technique of Doppler-free laser polarization spectroscopy. Molecular constants G_v, B_v, D_v and H_v and Dunham molecular constants of the X and B states were obtained. Dissociation energy of the X and the B states were estimated as 5030 ± 2 cm^{-1} and 1319 ± 2 cm^{-1}, respectively.

The energy levels of the $B^1\Pi$ state were found to present many irregularities due to perturbations. The fluorescence spectrum to the $a^3\Sigma^+$ state following an excitation to a strongly perturbed B state level was recorded with monochromator. According to their assignment they observed transitions to $v = 0 - 17$ and $N = 13 - 25$ and obtained from these data Dunham molecular constants of the $a^3\Sigma^+$ state. The dissociation energy value obtained for the $a^3\Sigma^+$ state was 182 ± 2 cm^{-1}.

In Ref. [70] perturbations in the $B^1\Pi$ state were studied in more detail. A number of the rovibrational levels of the B state were found to be strongly perturbed. Molecular constants of the $c^3\Sigma^+$ and the $b^3\Pi_1$ states were estimated. The hyperfine splitting of the $c^3\Sigma^+$ state was observed.

In Ref. [71] hyperfine structures of the triplet states were analyzed. The sub-Doppler high resolution excitation spectrum of NaRb was measured by selectively monitoring the fluorescence intensity from perturbed levels to the $a^3\Sigma^+$ lower state. Many transitions were observed to the $(2)^3\Sigma^+$ state perturbed by $B^1\Pi$. Fully resolved hyperfine splittings were observed and analyzed.

In 1996 [72] S. Kasahara *et al.* measured high-resolution spectra of the $B^1\Pi - X^1\Sigma^+$ transitions in the $^{23}Na^{85}Rb$ molecule by the technique of the Doppler-free optical-optical double resonance polarization spectroscopy OODRPS (pump beam excites the $B^1\Pi(v', J')$ level, whereas probe beam is scanned across

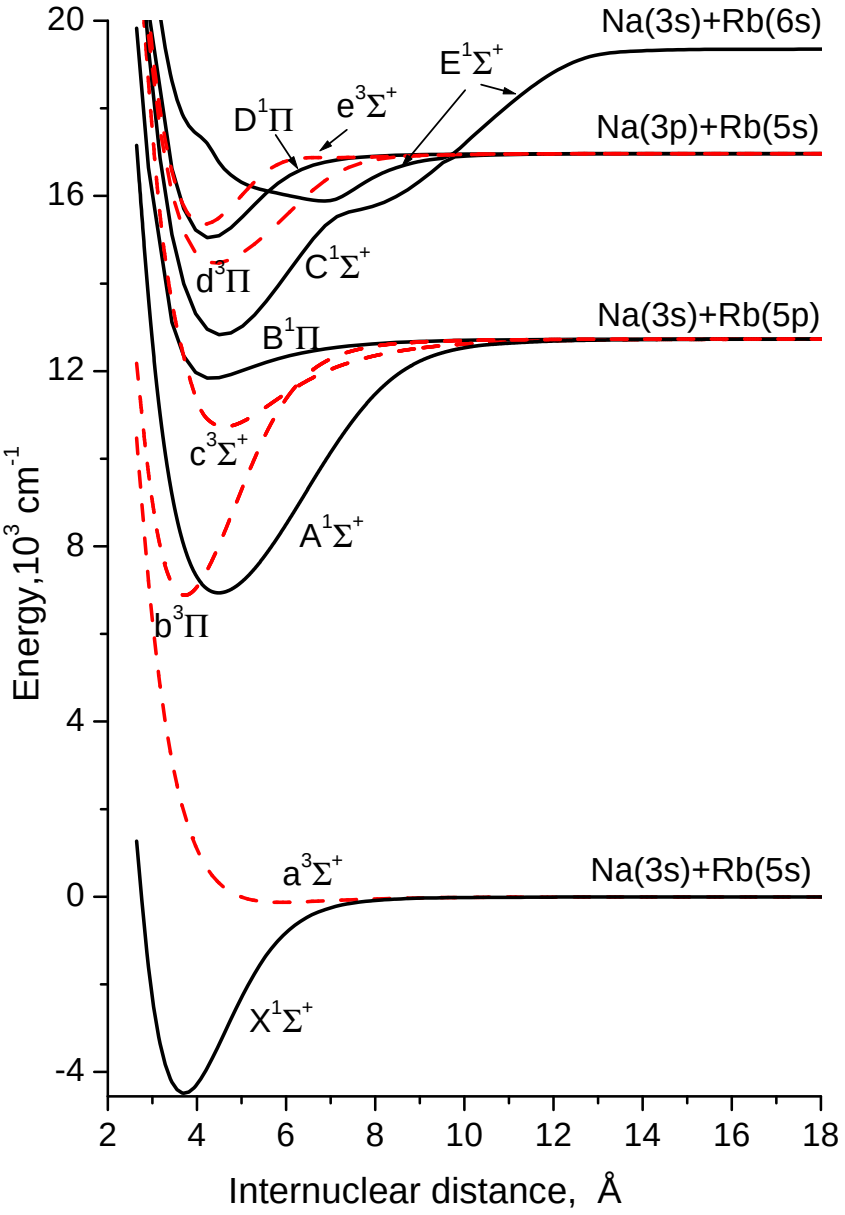

Figure 4.1. Potential energy curves for the low lying singlet (solid lines) and triplet (dashed lines) states of NaRb from *ab initio* calculations [34].

the $B^1\Pi\,(v',\,J') - X^1\Sigma^+(v'',\,J'')$ transitions). 44 level energies with $J'' = 10$ and 12 in the v'' range 5–30 were obtained. Combining data from 1996 and 1991 [69] the Dunham constants valid up to $v'' = 30$ (57% of the potential well depth) were obtained and RKR potential in the internuclear distance range $2.86 \leq R \leq 5.17$ Å was constructed.

In the same work transitions to the $a^3\Sigma^+$ state level ($v'' = 4, N'' = 15$) from the $B^1\Pi(v' = 8,\, J' = 15)$ level were measured by the Doppler-free OODRPS. The hyperfine splittings, which are described by Hund's case ($b_{\beta S}$), were observed, and the hyperfine constants $A_{\rm Na}$ and $A_{^{85}\rm Rb}$ of the $a^3\Sigma^+$ ($v'' = 4$) level were determined as 0.0293 and 0.0336 $\rm cm^{-1}$, respectively. The hyperfine splittings were identified as originating from the Fermi contact interaction.

In 2001 W.T. Zemke and W.C. Stwalley [73] made analysis of all available experimental and theoretical data about the $X^1\Sigma^+$ and $a^3\Sigma^+$ states in order to obtain potentials of these states in a wide range of internuclear distances. The experimental data used were from Ref. [69, 72]. Dunham molecular constants for the X state from Ref. [72] were replaced my more precise analogue. Hybrid potentials of the $X^1\Sigma^+$ and $a^3\Sigma^+$ states were constructed using experimental data, theoretical long-range potentials, and exponential repulsive wall extrapolation. As a result, new, more accurate values of the dissociation energies of the X and a states were obtained, being 5030.75 ± 0.10 $\rm cm^{-1}$ and 183.0 ± 0.10 $\rm cm^{-1}$, respectively. The authors of Ref. [73] have concluded that further experimental studies of the X state in the $v'' > 30$ region are required to refine the NaRb $X^1\Sigma^+$ state potential curve in the intermediate energy region.

Laboratory of Optical Polarisation of Molecules at the University of Latvia has also contributed a lot to the studies of NaRb.

Accurate measurements of the Λ-splitting energy $\Delta_{e/f}$ of particular rovibronic levels of the $B^1\Pi$ and $D^1\Pi$ state by means of the Radio Frequency – Optical Double resonance (RF-ODR) method were performed in Ref. [65]. The measured $\Delta_{e/f}$ values were used to determine the q factors [4] and the permanent electric dipole moments for a number of v', J' levels employing dc Stark effect in the $^1\Pi$ states [65].

In Ref. [4] the experimental D–X LIF intensities and rovibronic term values were simultaneously embedded in a non-linear least-square fitting procedure to refine the $D^1\Pi$ potential.

Recently the spontaneous lifetimes (about 20 ns) have been determined for a number of $D^1\Pi(v',\,J')$ levels from LIF decay after pulsed excitation [74].

In the paper [75] the first study of the fully mixed $A^1\Sigma^+ - b^3\Pi$ complex of the NaRb molecule based on high-resolution sub-Doppler spectroscopy and intensity measurements was performed. A two-laser V-type pump–probe excitation scheme was employed to obtain A←X transition frequencies to 16 A-state vibrational levels from $v = 6$ to $v = 21$ with J from 8 to 23. Additionally, relative intensities in A→X LIF spectra have been recorded, including progressions with all observable transitions to the ground state vibronic levels, the latter yielding unambiguous v assignment of the observed A-state levels. All experimental rovibronic term values and all measured intensity distributions were embedded in a direct simultaneous weighted nonlinear fitting in the framework of an elaborated inverted channel-coupling approach allowing authors to obtain the deperturbed relativistic diabatic potentials of the interacting $A^1\Sigma^+$ and $b^3\Pi$ states.

LIF intensity distribution as a deperturbation tool and its application to the fully-mixed $A^1\Sigma^+ - b^3\Pi$ complex of NaRb was further discussed in more detail in Ref. [76].

The most comprehensive theoretical studies of the NaRb molecule have been reported in Ref. [34] where potential energy curves (PEC) for the ground and several excited states up to their atomic limits are given. In Ref. [4] *ab initio* calculations of the 11 lowest electronic states potential energy curves, transition dipole moments for a number of electronic transitions, and L-uncoupling matrix elements between $^1\Pi$ and $^1\Sigma^+$ states with respective Λ-doubling constants are presented.

Na-Rb system is an interesting object for studying atom-atom collisions at ultra-low temperature as well as a promising candidate for two-species Bose-Einstein condensate. Results of experimental research performed in different groups on inelastic cold collisions in Na-Rb trap were reported in Refs. [25, 26, 77], analyzing trap losses as dependent on trap laser intensity and frequency. Theoretical calculations of

long-range potentials exist [78, 79, 80, 81]. Calculations of the Na-^{85}Rb and Na-^{87}Rb scattering lengths have been recently reported in Refs. [82, 83, 84, 85], where results obtained in this thesis [dis1, dis2] were used.

Summarising, at the moment of the beginning of this work most of information on the NaRb electronic states was fragmentary and of accuracy, insufficient for demands of modern spectroscopy, especially cold collision physics. Available information on the $X^1\Sigma^+$ state was of high accuracy, but limited at $v'' = 30$ and low J''. The lowest triplet $a^3\Sigma^+$ state was studied in a wide range, but with low accuracy. $D^1\Pi$ state was also investigated in a limited range of quantum numbers with low accuracy. $C^1\Sigma^+$ state has never been observed previously.

4.2 NaRb $X^1\Sigma^+$ state: Experiments at the University of Latvia [dis1]

During the studies on the permanent electric dipole moments and q factors in the $B^1\Pi$ and $D^1\Pi$ states of NaRb performed at the University of Latvia [65, 4], it was realized that information on the $X^1\Sigma^+$ ground state is insufficient, therefore we put forward a **goal** to obtain accurate $X^1\Sigma^+$ state potential, which would be applicable in a wide range of vibrational and rotational quantum numbers.

4.2.1 Observations

The usual way of extending the range of ground state vibrational levels v'' observed in emission for alkali dimers is to observe either the A–X or C–X transitions, instead of the B–X. In the present study we made use of the opportunity to excite the high vibrational levels of the $C^1\Sigma^+$ electronic state in a direct $C^1\Sigma^+ \leftarrow X^1\Sigma^+$ transition and to exploit the subsequent visible emission. As follows from the *ab initio* potential curves [4] depicted in Fig. 4.1, there is enough reason to predict that $C^1\Sigma^+ \rightarrow X^1\Sigma^+$ fluorescence can be excited by visible Ar^+ laser lines and that it should be intense up to sufficiently high v'' levels of the $X^1\Sigma^+$ state due to considerable shift between the respective potentials (similarly to the case of the NaK molecules, see [86]). In the early paper on the NaRb LIF studies [68] it was reported that the Ar^+ laser 514.5 nm line induced fluorescence spectrum was observed up to 14000 cm^{-1} (710 nm). This spectrum was later [69] recognized as the transitions ending on high v'' levels of the $X^1\Sigma^+$ state. The simplicity of the excitation scheme and the convenient visible range of LIF encouraged us to undertake further investigations of the $C \rightarrow X$ emission in order to reach as many as possible $v'' > 30$ rovibronic levels and, thus, to fill the gap between the accurate low v'' experimental data [72, 69] and calculated long-range data [73, 79].

4.2.2 Analysis of the $C^1\Sigma^+ \rightarrow X^1\Sigma^+$ progressions

In our experiments we used the Ar^+ laser 514.5 nm (19429.826 cm^{-1}) line for exciting the $C^1\Sigma^+ \rightarrow X^1\Sigma^+$ progressions, which stem up to $v'' = 76$, thus providing the data about vibrational levels $v'' > 30$. These progressions, possessing maximum intensity in the red spectral range, can be attributed to the C–X system originating from high $v' > 30$ levels. Such assumption is proved by tentative evaluation of the respective Franck-Condon factors using the difference based *ab initio* $C^1\Sigma^+$ potential [4].

Experimental justification is as follows. First, no singlet red LIF progressions have been observed, only the doublet-type series which correspond to the $\Sigma - \Sigma$ transitions. Additionally, we have undertaken a Stark-effect based test which showed that applying an external electric field up to 5 000 V/cm did not cause any changes in the red LIF spectra. If it were the $D^1\Pi$ state, due to the Stark-induced e/f mixing in the $^1\Pi$ state (see [4, 65]) the triplet LIF spectra would be observed instead of the doublet spectra. The above considerations allowed us to conclude that LIF progressions observed in the red spectral range up to 680 nm originated from the $C^1\Sigma^+$ state.

Fig. 4.2 presents fragments of the $C^1\Sigma^+ \rightarrow X^1\Sigma^+$ fluorescence progressions in the range of high ground state v'' values. To assign the transitions in this spectrum, it was necessary to go to smaller $v'' < 30$ region where accurate spectroscopic constants of the $Na^{85}Rb$ ground state from Refs. [69, 73] are applicable. This was the most difficult part of the experiment due to smaller intensities of the C–X transitions in the low v'' region and the partial overlapping with D–X transitions. As a result, we have registered and assigned five $C^1\Sigma^+ \rightarrow X^1\Sigma^+$ fluorescence progressions presented in Table 4.1 which were excited by different modes of the 514.5 nm line. For small J'' ($J'' < 27$) the progressions assignment was based on Dunham molecular constants [73], while for large J'', as well as for the $^{23}Na^{87}Rb$ isotopomer, a numerical solution of the radial Schrödinger equation was exploited with the RKR potential constructed from molecular constants, given in Ref. [73].

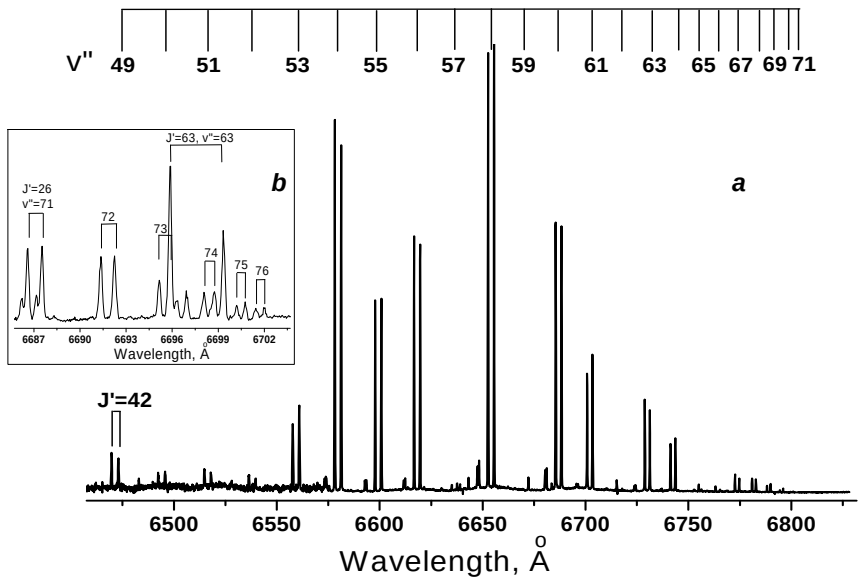

Figure 4.2. Pieces of the C→X fluorescence spectrum induced by absorption of the Ar^+ laser 514.5 nm line. (a) $C^1\Sigma^+(v'=34,\ J'=42) \leftarrow X^1\Sigma^+(v''=1,\ J''=43)$ in $Na^{85}Rb$; (b) $C^1\Sigma^+(v'=39,\ J'=26) \leftarrow X^1\Sigma^+(v''=4,\ J''=25)$ in $Na^{85}Rb$ and $C^1\Sigma^+(v'=35,\ J'=63) \leftarrow X^1\Sigma^+(v''=1,\ J''=62)$ in $Na^{87}Rb$. Vibrational assignment of the $C^1\Sigma^+$ state levels was established in later studies (see Section 4.5).

4.2.3 Analysis of term values

The total data set included in the analysis of the $X^1\Sigma^+$ state term values comprises three parts. The first part contains the present measured 302 term values $E^{expt}_{v''J''}$ assigned to both $Na^{85}Rb$ and $Na^{87}Rb$ isotopomers corresponding to $v'' \in [24, 76]$; $J'' \in [12, 64]$ levels (see Table 4.1). The average accuracy of these data is estimated as 0.1 cm^{-1}. The second part contains 44 highly accurate (with a line position uncertainty $\sigma^{expt}_{v''J''} \approx 0.003$ cm^{-1}) experimental term values for $v'' \in [5, 30]$; $J'' = 10, 12$ levels of $Na^{85}Rb$ given in Table I of Ref. [72]. The third part contains eight $v'' \in [0, 3]$; $J'' = 10, 12$ term values restored using the relevant G_v, B_v, D_v and H_v molecular constants of the $^{23}Na^{85}Rb$ isotopomer given in Table I of Ref. [69]; it is assumed that the uncertainty of these data $\sigma^{expt}_{v''J''}$ does not exceed 0.003 cm^{-1}.

Altogether 354 term values of the NaRb $X^1\Sigma^+$ state were treated simultaneously by the combined-isotopomer weighted least-squares (WLS) fit:

$$\bar{\sigma}_f = \min \left[\frac{1}{N-M} \sum_{v''J''}^{N} \left(\frac{E^{expt}_{v''J''} - E^{calc}_{v''J''}}{\sigma^{expt}_{v''J''}} \right)^2 \right]^{1/2}, \tag{4.1}$$

where N is the total number of the experimental energies, and M is the number of the fitting parameters obtained below by both Dunham-type and direct potential fit analysis.

4.2.4 Dunham-type fit

Term values for the isotope-substituted NaRb molecule were represented by a Dunham expansion. The Dunham parameters Y_{lm} of the $Na^{85}Rb$ isotopomer presented in Table 4.2 were obtained by the weighted linear LS fitting procedure (4.1) accompanied by experimental determination of the optimum power degrees (l_{max}, m_{max}) for each vibrational and rotational expansion. During the fit the lowest centrifugal

Table 4.1. $C^1\Sigma^+(v',\,J') - X^1\Sigma^+(v'',\,J'')$ transitions induced by the 514.5 nm Ar^+ laser line. $E^{expt}_{v'J'} = E^{calc}_{v''J''} + \nu_{laser}$ are the respective $C^1\Sigma^+$ term values. Parameters $\Delta E_{v'J'} = E^{expt}_{v'J'} - E^{shift}_{v'J'}$ account for uncertainty in the fluorescence series origin, $E^{shift}_{v'J'}$ denoting the corrected term value. $\Delta E^{Dunh}_{v'J'}$ and $\Delta E^{MLJ}_{v'J'}$ values were obtained within the Dunham-type and direct MLJ potential fits, respectively. The errors given in parentheses are equal to two standard deviations. All energies are in cm^{-1}.

Isotopomer	v''	J''	J'	$E^{expt}_{v'J'}$	observed v'' range	$\Delta E^{Dunh}_{v'J'}$	$\Delta E^{MLJ}_{v'J'}$
$^{23}Na^{85}Rb$	1	12	13	19600.11	[21,70]	0.12(±0.04)	0.10(±0.05)
$^{23}Na^{85}Rb$	4	25	26	19947.63	[26,76]	-0.01(±0.04)	-0.01(±0.02)
$^{23}Na^{85}Rb$	1	43	42	19720.75	[15,71]	0.19(±0.09)	0.21(±0.11)
$^{23}Na^{87}Rb$	3	61	60	20056.69	[27,71]	0.48(±0.25)	0.35(±0.22)
$^{23}Na^{87}Rb$	1	62	63	19858.11	[24,71]	0.37(±0.30)	0.18(±0.16)

distortion constants (CDCs) $Y_{0,2}$, $Y_{1,2}$ and $Y_{0,3}$ were held fixed at the values obtained from highly accurate $v'' \in [0,6]$; $J'' \in [0,80]$ term energies, see Table III in Ref. [69]. Five adjustable parameters $\Delta E^{Dunh}_{v'J'}$ presented in Table 4.1 were added to the fitting procedure to remove systematic errors caused by an uncertainty of the present experimental series origin, i.e. $E^{expt}_{v'J'}$. The resulting molecular constants presented in Table 4.2 reproduce the high accuracy data [69, 72] corresponding to $J'' = 10, 12$ levels with r.m.s.= 0.002 cm^{-1} while the present experimental term values are reproduced with r.m.s.= 0.1 cm^{-1}.

The resulting $G(v'')$ and $B(v'')$ expansions were further applied to a conventional first-order RKR potential construction [44] up to the last observed vibrational level $v'' = 76$. A non-physical bend (a "turning over") had appeared in the inner wall of the RKR curve for $v'' \geq 55$ levels. This means that the obtained vibrational and rotational constants are not self-consistent for upper vibrational levels due to strong correlation between the rotational and CDC parameters. The bend problem was solved by the exponential extrapolation of the inner wall and respective correction of the outer wall.

The quality of Dunham, RKR and hybrid approaches is illustrated by Fig. 4.3 (a, c). In contrast to E_{Dunh} and E_{RKR} term values, the E_{hyb} ones systematically deviate from the experimental data for $v'' > 35$, the difference reaching its maximum at $v'' \simeq 58$. At the same time, the pronounced systematic errors of the E_{RKR} values corresponding to highest vibrational terms still remain, see Fig. 4.3 (a).

4.2.5 Morse-Lennard-Jones potential fit

To consistently process different sets of experimental and theoretical data, we applied a direct potential fit analysis based on the Morse-Lennard-Jones (MLJ) potential (2.51) (see also Section 2.10.2). Since the reduced masses of the $Na^{85}Rb$ and $Na^{87}Rb$ isotopomers are very close to each other, the difference in the respective adiabatic correction to the relevant Born-Oppenheimer potential can be neglected. Hence, the adiabatic potentials for both isotopomers can be represented by a single mass-independent curve.

The power $n = 6$ predicts correct long-range behavior of the NaRb ground state potential $U(R) \sim D_e - C_6/R^6$ dissociated into two ^1S state atoms. In the z-region covered by the experimental term values the exponent parameter $\beta(z)$ is approximated by the ordinary polynomial expansion $\sum_{m=0}^{M} \beta_m z^m$. To extrapolate the $\beta(z)$ function to the "dark" interval between the region covered by experimental data and the dissociation limit, the ordinary cubic spline $\beta_E(z) = \sum_{n=0}^{3} b_n (z-1)^n$ was adopted. Respective coefficients $b_0 = \beta_\infty$, $b_1 = 0$, $b_2 = [3(\beta_M - b_0) - \beta'_M(z_M - 1)]/(z_M - 1)^2$ and $b_3 = [\beta'_M - 2b_2(z_M - 1)]/3(z_M - 1)^2$ are determined by matching smoothly the $\beta(z)$ polynomial expansion at the meeting point $z_M = (R_M - R_e)/(R_M + R_e)$. Here $\beta_M \equiv \beta_E(z_M) = \beta(z_M)$; $\beta'_M \equiv \partial\beta_E(z_M)/\partial z = \partial\beta(z_M)/\partial z$ and the boundary conditions are used at $R \to \infty$, i.e. $\beta_E(1) = \beta_\infty$ and $\partial\beta_E(1)/\partial z = 0$.

The $\beta_\infty = 0.638$ value was estimated according to $\beta_\infty = \ln[2D_e R_e^6/C_6]$ [60], where the dispersion coefficient C_6 was taken from Ref. [79]. The matching point $R_M = 11$ Å was fixed at near the right turning point of the last observed vibrational level $v'' = 76$. The equilibrium distance R_e, polynomial coefficients

Table 4.2. Dunham parameters (in cm^{-1}) for the $X^1\Sigma^+$ state of the $Na^{85}Rb$ isotopomer, obtained from a simultaneous fit of the total set of the experimental term values corresponding to both $Na^{85}Rb$ and $Na^{87}Rb$ isotopomers. Five additional fitting parameters corresponding to origin uncertainties in the present $C \rightarrow X$ LIF series are given in Table 4.1. The value of $Y_{0,0}$ is calculated.

$Y_{0,0}$	-0.0225	$Y_{2,1}$	1.558186×10^{-6}
$Y_{1,0}$	106.844973	$Y_{3,1}$	-5.705886×10^{-7}
$Y_{2,0}$	-0.3769493	$Y_{4,1}$	3.065820×10^{-8}
$Y_{3,0}$	$-1.3253577 \times 10^{-3}$	$Y_{5,1}$	$-7.845547 \times 10^{-10}$
$Y_{4,0}$	6.1584938×10^{-5}	$Y_{6,1}$	9.305117×10^{-12}
$Y_{5,0}$	$-4.7069851 \times 10^{-6}$	$Y_{7,1}$	$-4.254388 \times 10^{-14}$
$Y_{6,0}$	1.8256265×10^{-7}	$Y^{\dagger}_{0,2}$	-1.2107×10^{-7}
$Y_{7,0}$	$-4.4448825 \times 10^{-9}$	$Y^{\dagger}_{1,2}$	-9.50×10^{-10}
$Y_{8,0}$	$6.4873784 \times 10^{-11}$	$Y_{2,2}$	1.78×10^{-10}
$Y_{9,0}$	$-5.2293387 \times 10^{-13}$	$Y_{3,2}$	-1.92×10^{-11}
$Y_{10,0}$	$1.7866377 \times 10^{-15}$	$Y_{4,2}$	5.3×10^{-13}
$Y_{0,1}$	7.011329×10^{-2}	$Y_{5,2}$	-4.6×10^{-15}
$Y_{1,1}$	-2.823823×10^{-4}	$Y^{\dagger}_{0,3}$	2.08×10^{-13}
No. of data		354	
Total no. of parameters		31	
No. of fitting parameters		27	
$\bar{\sigma}_f$		1.18	

† Value and uncertainty are taken from Table III of Ref. [69].

β_m ($m \in [0, 9]$), as well as the origins of the present five LIF series were considered as adjustable fitting parameters during the weighted non-linear LS fit. The required initial set of the R_e and β_m values was estimated by a transformation of the present RKR potential to its MLJ counterpart. The $D_e = 5030.75$ cm^{-1} value [73] was fixed during the fit as considering dissociation energy as a free parameter in the MLJ approach has often been found to noticeably underestimate D_e value [62]. The resulting MLJ potential given in Table 4.3 reproduces low-J'' term values from Refs. [72, 69] with r.m.s.= 0.004 cm^{-1} while the present experimental term values with r.m.s.= 0.1 cm^{-1}.

Table 4.3. MLJ potential (2.51) parameters for the $X^1\Sigma^+$ state of NaRb obtained from a direct fit to the experimental term values corresponding to both $^{23}Na^{85}Rb$ and ^{23} $Na^{87}Rb$ isotopomers. The numbers in parentheses are equal to two standard deviations. Five additional fitting parameters corresponding to the origin uncertainties in the present $C \rightarrow X$ LIF series are given in Table 4.1.

D_e (cm^{-1})	5030.75[a]	($\pm$0.10)[a]
R_e (Å)	3.64421	($\pm 1.1 \times 10^{-3}$)
β_0	-6.312091	($\pm 4.4 \times 10^{-4}$)
β_1	9.665262	($\pm 7.1 \times 10^{-4}$)
β_2	12.70902	($\pm 1.2 \times 10^{-3}$)
β_3	65.58015	($\pm 2.3 \times 10^{-3}$)
β_4	-15.30441	($\pm 4.3 \times 10^{-3}$)
β_5	-643.6652	($\pm 3.1 \times 10^{-2}$)
β_6	2488.876	($\pm$0.30)
β_7	-10772.84	($\pm$0.78)
β_8	22720.46	($\pm$0.74)
β_9	-16240.38	($\pm$0.46)
R_M (Å)		11.0
b_∞		0.638804
b_2		-0.986641
b_3		-1.525996
No. of data		354
Total No. of parameters		21
No. of fitting parameters		16
$\bar{\sigma}_f$		1.27

[a] Value and uncertainty are borrowed from Ref. [73].

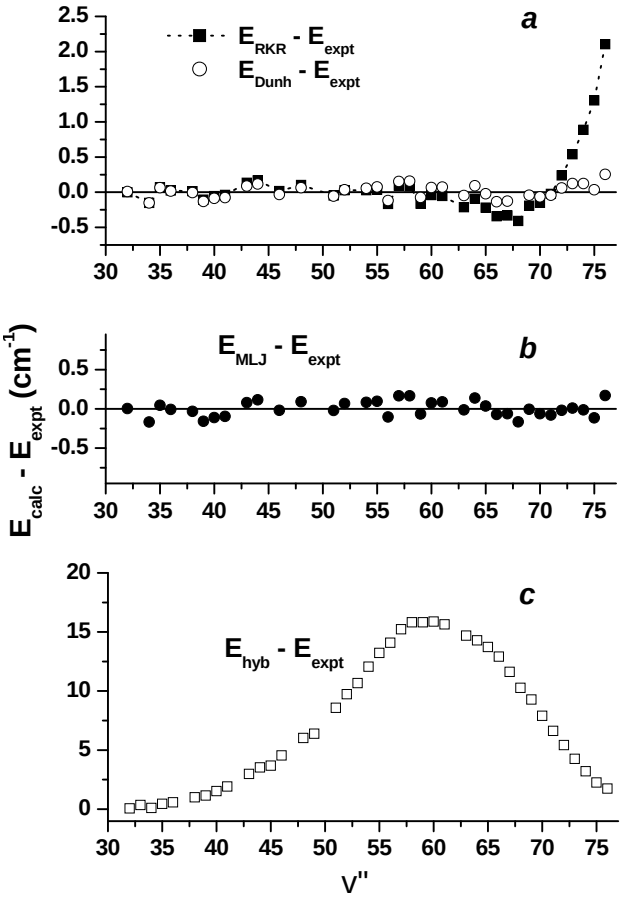

Figure 4.3. Differences between calculated $E^{calc}_{v''J''}$ and experimental $E^{expt}_{v''J''}$ term values for $Na^{85}Rb$ $X^1\Sigma^+(v'' > 30, J'' = 25)$. (a) $E^{Dunh}_{v''J''}$ are calculated by Dunham constants from Table 4.2 and $E^{RKR}_{v''J''}$ by the present RKR; (b) $E^{MLJ}_{v''J''}$ are calculated by the present direct MLJ potential fit analysis; (c) $E^{hyb}_{v''J''}$ are calculated by the preceding hybrid potential [73].

4.2.6 Results and conclusions

1. LIF spectra to the NaRb $X^1\Sigma^+$ ground state up to $v'' = 76$ were recorded for the first time using $C^1\Sigma^+ \rightarrow X^1\Sigma^+$ transitions. The obtained data set consists of 300 transitions in $Na^{85}Rb$ and $Na^{87}Rb$ to ground state levels in the range $v'' = 24 - 76$, $J'' = 12 - 64$, with typical accuracy of 0.1 cm^{-1}. The last observed level is ($v'' = 76$, $J'' = 27$).

2. Transition frequencies were used for a direct fit of a MLJ potential energy curve. The fitted potential describes the present experimental data with r.m.s.= 0.1 cm^{-1}. Experimental PEC covers 99.85% of the potential well depth. Term energies were also represented by the Dunham expansion and RKR potential.

3. MLJ construction allowed us to match gently the previous highly accurate experimental term values available for the bottom of the potential with its long-range behavior through the intermediate v'' region completely covered by the present measurements. In spite of the moderate accuracy of the current measurements (0.1 cm^{-1}) the derived MLJ potential significantly improves the description of the NaRb $X^1\Sigma^+$ ground state in the $v'' \gtrsim 35$ region.

4. Highly accurate experimental term values for the extended range of rotational levels would be desirable for further improvement of the ground state potential.

5. $C^1\Sigma^+$ state has been observed for the first time. Rotational and isotopomer assignment of five levels has been made.

4.3 NaRb $X^1\Sigma^+$ state: Experiments at the University of Hannover [dis2]

4.3.1 Experiment

In the experiments in Hannover the NaRb molecules were studied with the same LIF method, but two important changes compared to the experiments performed in Riga have been introduced: producing of molecules in a heat pipe oven and fluorescence analysis with a Fourier-transform spectrometer. Another great advantage of the laboratory in Hannover is a variety of available laser sources, see Section 3.2.

The heat-pipe oven was operated at temperatures between 560 K and 600 K and typically with 2 mbar of Ar as buffer gas. At these conditions apart from the atomic vapors all three types of molecules were formed: Na_2, Rb_2 and NaRb. This mixture was illuminated by three different laser sources: a single mode, frequency doubled Nd:YAG laser, Ar^+ ion laser, and Rhodamine 6G dye laser. Setting the working temperatures as low as possible we reduced the density of the Na_2 molecules reaching a relatively intense NaRb spectra almost free of Na_2 emission. As follows from Ref. [87], Rb_2 fluorescence can be observed when using for excitation Ar^+ lines with wavelength smaller than 496.5 nm. We clearly observed Rb_2 progressions in the IR region ($C^1\Pi_u \rightarrow 2^1\Sigma_g^+$), and also noticed some weak lines in the visible range, which could be attributed to Rb_2 based on their spacings.

The Ar^+ ion laser was operated both in a single-mode and multi-mode regimes. The 514.5 nm, 501.7 nm, 496.5 nm, 488.0 nm, and 476.5 nm lines induced fluorescence mainly due to the $D^1\Pi \rightarrow X^1\Sigma^+$ transitions in NaRb. The Na_2 $B^1\Pi_u \rightarrow X^1\Sigma_g^+$ band was also observed, especially exciting with the bluer Ar^+ laser lines. Along with the D $\leftarrow$ X system, the 514.5 nm line excites also transitions in the $C^1\Sigma^+ \leftarrow X^1\Sigma^+$ system of NaRb, as was established in our experiments in Riga [dis1] (see Section 4.2). Ar^+ laser line 501.7 nm also excites the C state, but the resulting fluorescence is very weak. Only one progression was identified. Altogether with the Ar^+ laser lines 93 $D^1\Pi \rightarrow X^1\Sigma^+$ and 12 $C^1\Sigma^+ \rightarrow X^1\Sigma^+$ progressions were identified.

We used the following method in order to bring the frequency of the single-mode Ar^+ laser exactly in resonance with desired transitions. As a first step we recorded the LIF spectrum for a given frequency simultaneously with the Fourier spectrometer and a GCA/McPherson Instruments scanning monochromator (1 m focal length). The high resolution Fourier spectrum helped us to assign unambiguously the record of the monochromator. Then we set the monochromator on a strong and pronounced line of the progression of interest and tuned the Ar^+ laser frequency until the maximum signal on the monochromator was achieved. The frequency stability of the laser with a temperature stabilized intra-cavity etalon was sufficient in order to perform 10–20 scans with the Fourier spectrometer.

The Nd:YAG laser excited the $C^1\Sigma^+ \leftarrow X^1\Sigma^+$ and $D^1\Pi \leftarrow X^1\Sigma^+$ systems of NaRb (see Fig. 4.4). The frequency was varied between 18787.25 cm^{-1} and 18788.44 cm^{-1} and spectra were recorded at frequencies which excited strong fluorescence. 38 $D^1\Pi \rightarrow X^1\Sigma^+$ and 17 $C^1\Sigma^+ \rightarrow X^1\Sigma^+$ progressions were assigned.

The dye laser (Rhodamine 6G dye) excited the $B^1\Pi \leftarrow X^1\Sigma^+$ transitions and also weak transitions in the $C^1\Sigma^+ \leftarrow X^1\Sigma^+$ system and was used for two reasons. The first was to enrich the information on the ground-state levels with intermediate vibrational quantum numbers because of the gap between the levels from the D $\leftarrow$ X system (mainly with low v'') and those from the $C^1\Sigma^+ \leftarrow X^1\Sigma^+$ system (mainly with high v''). Second, we wanted to excite levels of the B state with significant triplet admixture due to perturbations from the neighboring $c^3\Sigma^+$ and $b^3\Pi$ states [69, 70]. Indeed, scanning the frequency of the dye laser from 16729 cm^{-1} to 16965 cm^{-1} we encountered a large number of excitations where a second fluorescence band around 12000 cm^{-1} appeared along with the B $\leftarrow$ X system (see Fig. 4.5). The analysis of this band confirmed that we have observed transitions to the $a^3\Sigma^+$ lowest triplet state (see Section 4.4)

4.3.2 Assignment of LIF progressions

The assignment of the recorded spectra was simplified by the MLJ potential (see Table 4.3) obtained from the experiments performed in Riga. First, spectra induced by the Ar^+ laser were assigned, because they

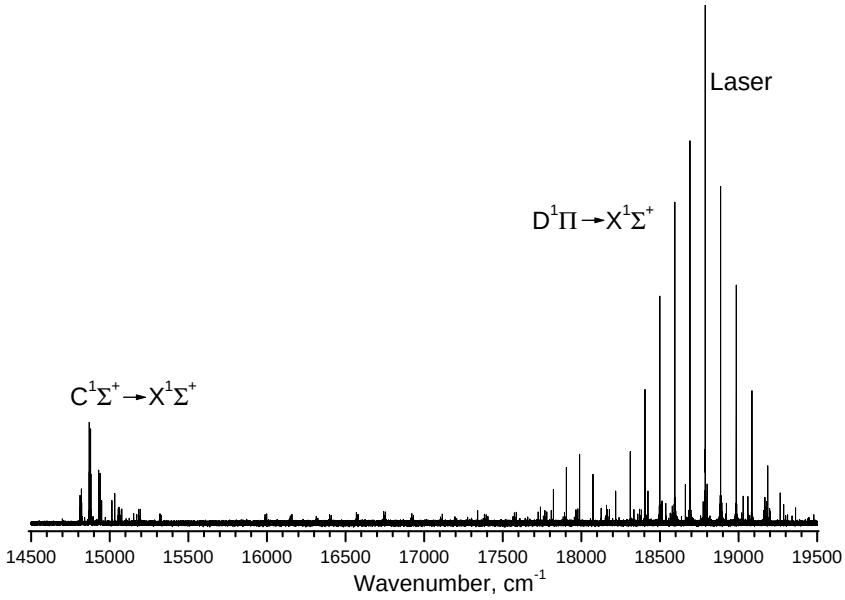

Figure 4.4. The $D^1\Pi \rightarrow X^1\Sigma^+$ and $C^1\Sigma^+ \rightarrow X^1\Sigma^+$ bands of NaRb excited by a single mode Nd:YAG laser (18787.985 cm^{-1}).

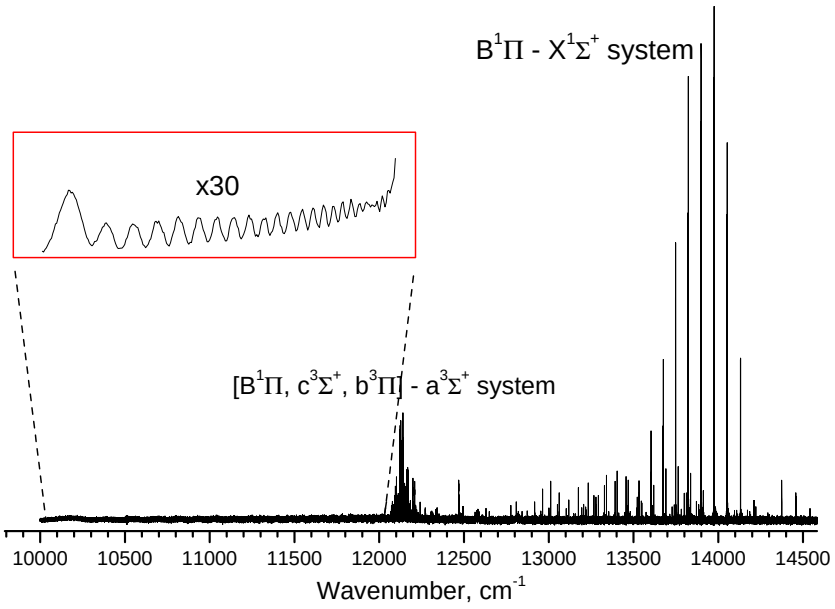

Figure 4.5. The $B^1\Pi \rightarrow X^1\Sigma^+$ and $[B^1\Pi, b^3\Pi, c^3\Sigma^+] \rightarrow a^3\Sigma^+$ bands of NaRb excited by a single mode Rhodamine 6G laser at frequency 16927.97 cm^{-1}. In the zoom box the continuum due to the bound-free emission to the repulsive wall of the $a^3\Sigma^+$ state is seen.

were partly known from the low-resolution studies [68, 65, 4, dis1]. Identification of 5 C $\rightarrow$ X progressions (see Table 4.1) from previous studies was clearly confirmed by high-resolution measurements. The longest observed progression ends at $v'' = 76$, see Fig. 4.6. Identification procedure was much faster that in the case of monochromator data due to high accuracy of the FTS data. High accuracy allows not to construct the Birge-Sponer plots[1] for the whole progression, but to use only several vibrational levels of the series for identification.

The assignment procedure was realized with the help of the programs (*Ident.exe*, *Find3.exe*) made by Dr. A. Pashov. As an input data the *Ident* program gets wavenumbers of the successive P, R or Q lines and the laser frequency. It calculates vibrational and rotational differences between observed lines. Then it compares these differences with the corresponding differences between the eigenenergies, calculated by solving SE or by Dunham expansion. The best 10 combinations of quantum numbers are given in the output for each isotopomer. Among them the best guess is made and the term energy of the upper level is also calculated from the frequency of the first listed transition and the eigenenergy of the corresponding level of the lower state. The exciting frequency value is searched in the vicinity of the given laser frequency and is also given for each assignment hypothesis. With different hypotheses one can calculate the LIF progression (*Find3*) and compare the calculated frequencies with the observations. In such a way assignment of LIF progressions becomes much faster, of course with two prerequisites: high accuracy data and sufficiently good initial potential or Dunham constants.

After we identified the strongest progressions, which were already observed in previous studies [68, 65, 4, dis1], a new spline pointwise PEC was fitted. This preliminary potential was further improved filling additionally collected experimental data; this sequential procedure allowed continuous checking of the assignment, especially for high J'' and in cases of large gaps in v''. The total data set (Fig. 4.7) consists of more than 6150 transitions in $Na^{85}Rb$ and 2650 in $Na^{87}Rb$.

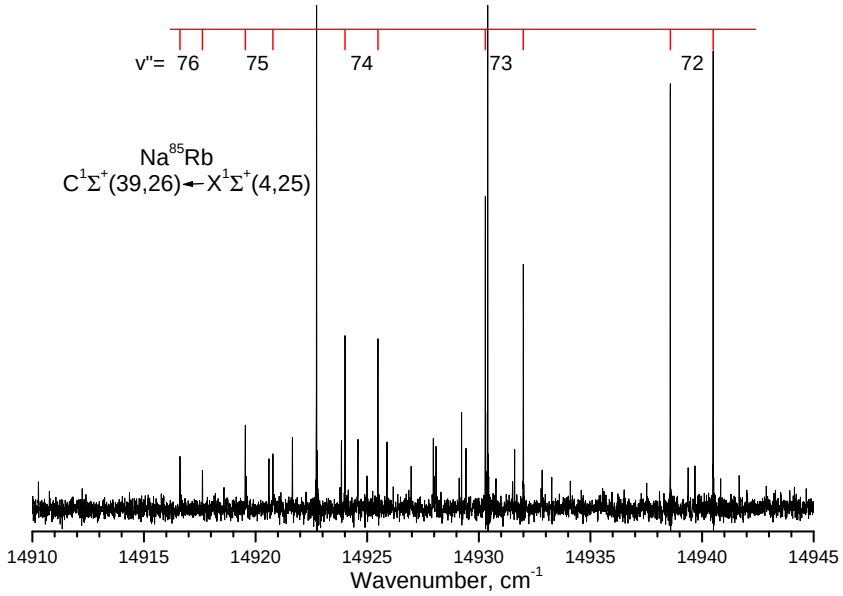

Figure 4.6. The vibrational progression up to $v'' = 76$ in $Na^{85}Rb$ excited by a single-mode Ar^+ laser line 514.5 nm.

In order to exclude any fitting parameters depending on the details of the excited states, we fitted the ground-state potential directly to the observed differences between ground-state levels [59]. Due to the

[1] Plot of vibrational spacings versus vibrational quantum number.

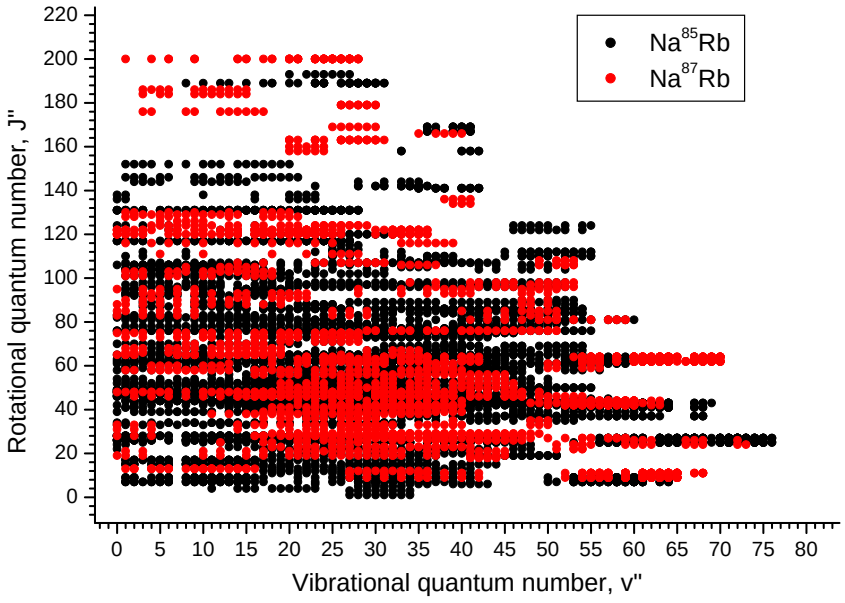

Figure 4.7. The range of vibrational and rotational quantum numbers of the observed ground state energy levels in $Na^{85}Rb$ and $Na^{87}Rb$.

large number of observed transitions, we restricted the possible combinations of line frequencies within a fluorescence progression only to pairs of one P and one R line. That is, we calculated only differences between each P and all R lines of a given progression. In our case of 8800 transitions we selected about 43300 differences for representing the different cases of vibrational intervals.

The uncertainties of the differences were estimated taking into account the instrumental accuracy and resolution, and the signal-to-noise ratio (SNR) for both transitions forming the difference. The uncertainty of strong lines was set to 0.003 cm^{-1} increasing to 0.007 cm^{-1} for weaker ones with SNR < 2. Differences which were measured several times were averaged with weighting factors determined from their uncertainties.

4.3.3 Construction of potential energy curve

The ground singlet states of both isotopomers of NaRb are described in the adiabatic approximation with a single potential-energy curve. The potential was constructed as a set of points $\{R_i, U(R_i)\}$ connected with cubic spline function [48] (see Section 2.10.1). In order to ensure proper boundary conditions for solving the Schrödinger equation for high vibrational energy levels, potential energy curve shape at distances up to $R \approx 20$ Å has to be accounted for. Therefore for $R > R_{\rm out}$ we adopted the usual dispersion form

$$U(R) = D_e - \frac{C_6}{R^6} - \frac{C_8}{R^8} - \frac{C_{10}}{R^{10}} \tag{4.2}$$

with coefficients C_6, C_8 taken from Refs. [80, 81]. The connecting point $R_{\rm out}$ and the parameters D_e and C_{10} were varied in order to ensure a smooth connection with the pointwise potential as follows. Initially, the PEC was constructed in a pointwise form up to 16 Å. After each fitting iteration D_e and C_{10} were adjusted to fit the shape of the pointwise potential between 13.0 Å and 16.0 Å to the analytic formula. The crossing point of the pointwise and the long-range curves was taken as $R_{\rm out}$. Since the experimental data are almost insensitive to details of the potential shape in this region, we found this

procedure sufficient and did not fit the long-range parameters directly to the experimental data. Once the final form of the PEC was achieved, we found that it is possible to extend the validity of the long-range expression down to < 11.8 Å.

The final set of potential parameters consists of 51 points. In order to calculate the value of the potential for $R < R_{\text{out}}$ a natural cubic spline [51] through all 51 points and for $R > R_{\text{out}}$ the long-range expression (4.2) should be used with parameters listed in Table 4.4. This final PEC gives a standard deviation of $\sigma = 0.0031$ cm^{-1} and a normalized standard deviation of $\bar{\sigma} = 0.70$ showing the internal consistency of the data set and the quality of the derived potential.

Table 4.4. Pointwise representation of the potential energy curve for the $X^1\Sigma^+$ state of NaRb.

R [Å]	U [cm^{-1}]	R [Å]	U [cm^{-1}]
2.101916	21110.5539	5.167536	2866.7126
2.200000	16374.1819	5.328985	3174.1150
2.298084	12751.3674	5.490435	3450.2078
2.396168	9944.6386	5.651884	3694.1882
2.494252	7761.9582	5.813333	3906.7423
2.592337	5992.3235	6.065085	4179.8842
2.690421	4637.9707	6.253898	4343.3002
2.788505	3543.2165	6.442712	4476.4609
2.886589	2638.9307	6.631525	4584.0755
2.984673	1900.4037	6.820339	4670.5331
3.082757	1308.0797	7.009152	4739.7196
3.180841	845.5522	7.197966	4794.9580
3.278926	498.1298	7.386780	4839.0226
3.377010	252.2899	7.556326	4870.9517
3.475094	95.41660	7.783673	4904.8112
3.573178	15.73046	8.098462	4939.0358
3.671262	2.3375	8.384103	4961.0335
3.792152	62.2402	8.669744	4977.0314
3.933165	217.7034	9.014483	4990.8655
4.074177	443.0825	9.398621	5001.4491
4.215190	718.3282	9.722105	5007.8576
4.360290	1035.8028	10.201818	5014.3657
4.521739	1411.4474	11.214546	5022.0531
4.683188	1794.2206	12.227273	5025.7686
4.844638	2170.6796	13.240000	5027.9612
5.006087	2530.6262		
$D_e = 5030.8480$ cm^{-1}			
$R_{\text{out}} = 12.090520$ Å		$C_8 = 3.590 \cdot 10^8$ cm^{-1}Å^8	
$C_6 = 1.293 \cdot 10^7$ cm^{-1}Å^6		$C_{10} = 3.539 \cdot 10^{10}$ cm^{-1}Å^{10}	

In order to find the region where the PEC is unambiguously characterized by the experimental data we analyzed the uncertainty of the fitting parameters as described in Ref. [54, 59]. In Fig. 4.8 the uncertainties of the fitted potential for intermediate internuclear distances are presented for three different values of the singularity parameter ζ (see Section 2.10.1). Although the outer classical turning point of the last observed energy level ($v'' = 76$, $J'' = 27$) is 12.4 Å, we see that the shape of the potential energy curve is unambiguously fixed (within the experimental uncertainty) approximately only between 3.0 Å and 9.8 Å since the uncertainties there almost do not depend on ζ. Therefore, although the fitted potential energy curve describes all the experimental data up to $v'' = 76$, there is no rigorous way to estimate the uncertainty of its shape beyond 9.8 Å (see also [59]). The result of Fig. 4.8 might indicate that the correlation between the left ($R < 3$ Å) and right ($R > 9.8$ Å) branch of the potential becomes significant.

In this respect the reported potential in Table 4.4 for these regions is only one possibility which describes our observations within the error limits.

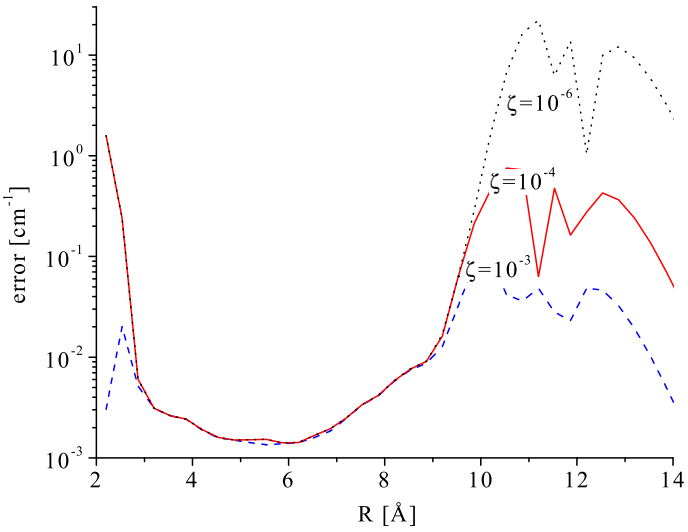

Figure 4.8. The derived standard deviation (in logarithmic scale) of the points of the pointwise potential curve of the NaRb $X^1\Sigma^+$ state for three different values of the singularity parameter ζ.

From the PEC we derive some parameters which will be useful when applying the potential for other calculations and spectroscopic studies. Their values are not rounded in order to keep consistency with the data from Table 4.4:

1. equilibrium distance of the potential, $R_e = 3.643415$ Å;
2. position of the level with $v'' = 0$ and $J'' = 0$, $E_{00} = 53.3117$ cm^{-1} with respect to potential minimum;
3. the dissociation energy of the ground state, calculated with respect to E_{00}, $D_0^{\mathrm{X}} = 4977.5363$ cm^{-1}.

In Fig. 4.9 the MLJ curve and the hybrid potential [73] are compared with the pointwise (PW) potential of this study. The reason for the difference between the PW potential and the MLJ potential around R_e is probably that for the construction of the latter potential the rotational quantum numbers for levels with $v'' < 30$ were limited only to the values of $J'' = 10, 12$. That's why rotational constant B_v of MLJ potential was inevitably determined with large uncertainty. Note that B_v determination error corresponds to shift of the whole potential along the internuclear axis, which is clearly indicated in Fig. 4.9.

The hybrid potential from Ref. [73] was constructed using the whole range of available rotational quantum numbers from the literature [69, 72], and therefore the agreement with the present study around R_e is much better. The deviations between the PW and the hybrid potential reaching 20 cm^{-1} for intermediate internuclear distances are caused by the extrapolation between the theoretical long-range part of the potential and the experimental short-range part. In the same region the experimentally determined shape of the MLJ potential is in a much better agreement with the present study.

Since the primary data from Ref. [69] were not available to us, we were able to check our potential only against the data published in Ref. [72]. Forming differences between transition frequencies exactly

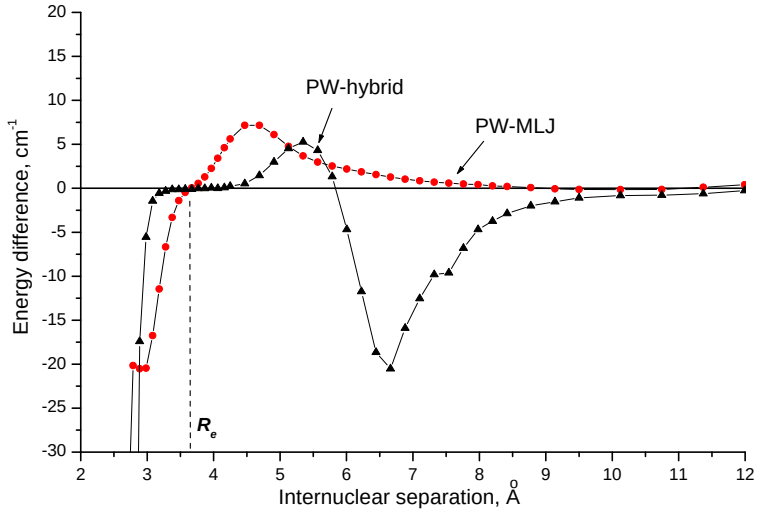

Figure 4.9. Differences between the pointwise representation of the NaRb ground-state potential derived in this study (PW) and previous potential energy curves from Ref. [73] (hybrid), Table 4.3(MLJ). The energy at the equilibrium point R_e is set to zero for all potentials and used as a reference point.

as for our LIF data, we found an agreement with the differences predicted by the present PEC from Table 4.4 with a standard deviation of 0.0026 cm^{-1}, well within the expected experimental error of 100 MHz. Only two transitions $(v' = 12, J' = 11) - (v'' = 17, J'' = 10)$ and $(v' = 12, J' = 11) - (v'' = 19, J'' = 10)$ were excluded from this comparison since differences with them showed systematically large deviations reaching 0.01 cm^{-1}.

The classical turning point of the last observed energy level ($v'' = 76$, $J'' = 27$) is around 12.4 Å. Although this point lies beyond the Le Roy radius for the NaRb 3^2S+5^2S asymptote ($R_{LR} = 11.2$ Å), the analysis of the PEC uncertainties indicates that with the present body of experimental data it is unsafe to determine C_6 and other dispersion coefficients. For this reason the experimental PEC was smoothly connected to a long-range potential formed by dispersion terms taken from the literature [80, 81]. For better description of the near asymptotic region of the PEC transition frequencies to weakly bound energy levels are needed and a combined analysis of the $X^1\Sigma^+$ and $a^3\Sigma^+$ states at long internuclear distances should be made (see Section 4.4.5).

4.3.4 Dunham molecular constants

We fitted a Dunham expansion to the observed $X^1\Sigma^+$ state levels using the program *Zweiat* [88]. In the Table 4.5 the set of Dunham coefficients for $Na^{85}Rb$ is listed. It describes the whole set of the measured differences for both isotopomers with a standard deviation of 0.003 cm^{-1} and a normalized standard deviation of 0.84. For calculating the eigenvalues for $Na^{87}Rb$ the usual scaling rules were used. The distribution of the indexes of the Dunham coefficients indicates that for description of such a large set of vibrational and rotational quantum numbers the parameters of the Dunham expansion lose their original meaning of "spectroscopic constants". The extremely small values of some coefficients $\sim 10^{-40}$ cm^{-1} indicate that they should be used with caution. Also, the extrapolation properties of such a set of Dunham coefficients are doubtful. Therefore, we prefer to give the full description of the experimental data by a potential-energy curve, which is obviously a much better physical model, and to present Dunham coefficients only for convenience since there are still applications where their use is easier and faster.

Table 4.5. Dunham coefficients Y_{ik} for $Na^{85}Rb$, in cm^{-1}, derived from the experimental data with $v'' \leq 76$ and $J'' \leq 200$.

i	k	Y_{ik}		i	k	Y_{ik}	
1	0	106.8544964		0	2	-1.20357	$\times 10^{-7}$
2	0	-0.37984464		1	2	-7.98199	$\times 10^{-10}$
3	0	-7.703864	$\times 10^{-4}$	2	2	-4.21837	$\times 10^{-12}$
5	0	-5.390011	$\times 10^{-7}$	7	2	-1.2888117	$\times 10^{-17}$
7	0	6.5551619	$\times 10^{-10}$	8	2	1.760426295	$\times 10^{-18}$
9	0	-1.9725192	$\times 10^{-12}$	9	2	-1.17937534	$\times 10^{-19}$
10	0	9.9663375	$\times 10^{-14}$	10	2	4.906556	$\times 10^{-21}$
11	0	-2.5123	$\times 10^{-15}$	11	2	-1.3413739	$\times 10^{-22}$
12	0	3.7418	$\times 10^{-17}$	12	2	2.3980927	$\times 10^{-24}$
13	0	-3.33869	$\times 10^{-19}$	13	2	-2.684354	$\times 10^{-26}$
14	0	1.652	$\times 10^{-21}$	14	2	1.70	$\times 10^{-28}$
15	0	-3.48	$\times 10^{-24}$	15	2	-4.6349	$\times 10^{-31}$
0	1	7.019021	$\times 10^{-2}$	0	3	1.4803	$\times 10^{-13}$
1	1	-2.943389	$\times 10^{-4}$	1	3	1.9481	$\times 10^{-15}$
2	1	-1.699605	$\times 10^{-6}$	3	3	-9.3543	$\times 10^{-18}$
4	1	-1.474183	$\times 10^{-9}$	8	3	7.87129	$\times 10^{-24}$
6	1	5.732233	$\times 10^{-12}$	9	3	-6.789833	$\times 10^{-25}$
7	1	-3.68622	$\times 10^{-13}$	10	3	2.13759	$\times 10^{-26}$
8	1	1.031766	$\times 10^{-14}$	11	3	-2.61852	$\times 10^{-28}$
9	1	-1.2551	$\times 10^{-16}$	13	3	1.974	$\times 10^{-32}$
11	1	1.22142	$\times 10^{-20}$	15	3	-1.0266	$\times 10^{-36}$
13	1	-1.6097	$\times 10^{-24}$	1	4	-1.953	$\times 10^{-20}$
14	1	9.446	$\times 10^{-27}$	2	4	-1.906	$\times 10^{-21}$
				5	4	1.11596	$\times 10^{-24}$
				6	4	-7.344	$\times 10^{-26}$
				8	4	7.4791	$\times 10^{-29}$
				10	4	-6.261	$\times 10^{-32}$
				11	4	8.982	$\times 10^{-34}$
				14	4	-6.3065	$\times 10^{-40}$
				7	5	-1.3005	$\times 10^{-33}$

4.3.5 Results and conclusions

1. High-resolution LIF spectra to the NaRb $X^1\Sigma^+$ ground state were obtained for the first time using the FTS method. The obtained data set consists of more than 6150 transitions in $Na^{85}Rb$ and 2650 in $Na^{87}Rb$ to the ground state levels in the range $J'' = 1 - 200$, $v'' = 0 - 76$, with typical uncertainty of 0.003 cm^{-1}.

2. Transition frequencies were used for a direct fit of a spline-pointwise potential energy curve. The fitted potential describes more than 43300 differences between 4090 energy levels of both isotopomers with a standard deviation $\sigma = 0.0031$ cm^{-1} and a normalized standard deviation of $\bar{\sigma} = 0.70$.

3. Experimental PEC covers 99.85% of the potential well depth. The classical turning point of the last observed energy level ($v'' = 76$, $J'' = 27$) is around 12.4 Å and this level is about 4.5 cm^{-1} below the asymptote.

4. Term energies were also represented by the Dunham expansion. Obtained set of constants reproduces the experimental term energies with $\sigma = 0.003$ cm^{-1} and $\bar{\sigma} = 0.84$.

4.4 Combined analysis of the NaRb $a^3\Sigma^+$ and $X^1\Sigma^+$ states [dis3]

The experimental data on the lowest triplet state $a^3\Sigma^+$ of NaRb until now were scarce [72] or obtained at low resolution [69] (see Section 4.1). **The goal** of the present experiments was twofold: extending experimental information about the triplet $a^3\Sigma^+$ state and collecting data close to the NaRb ground state asymptote, see Fig. 4.1. This would allow us to derive more reliable $X^1\Sigma^+$ and $a^3\Sigma^+$ state potentials at large internuclear distances. Constructing the appropriate Hamiltonian for the problem, it should be taken into account that both states, $a^3\Sigma^+$ and $X^1\Sigma^+$, couple by hyperfine interaction, which is for the most weakly bound states of the same order of magnitude as the binding energy itself. Thus close to the asymptote these states loose their triplet or singlet character and coupled channels treatment should be applied (see e.g. [89, 90, 63, 91]).

4.4.1 Observations and assignment of the triplet spectra

A well known technique for reaching the triplet manifold from singlet states is through singlet and triplet molecular states mixed by perturbations (e.g. the spin-orbit coupling). Such perturbations between the $B^1\Pi$, $b^3\Pi$ and $c^3\Sigma^+$ states in NaRb were reported by Wang *et al.* [69, 70]. Therefore, we used a Rhodamine 6G single mode dye laser and excited transitions to levels of the $B^1\Pi$, $b^3\Pi$ and $c^3\Sigma^+$ complex, see Fig. 4.1. In Fig. 4.5 we present a typical fluorescence spectrum, where along with the $B \rightarrow X$ band system, a weaker band appears around 12100 cm^{-1}, which is due to decay to the $a^3\Sigma^+$ state, together with a continuum spectrum from bound-free emission to the repulsive branch of the $a^3\Sigma^+$ state. This type of progression to the triplet state originates from the mixture of relatively low vibrational levels of the $B^1\Pi$ state with levels of the triplet $b^3\Pi$ and $c^3\Sigma^+$ states.

The dispersed fluorescence spectra of the transitions to discrete levels of the $a^3\Sigma^+$ state were found to be different depending on whether the excitation is a Q type or P, R type: after Q excitation we observed mainly triplet progressions, and after P, R excitation doublet progressions were observed. Let's describe the origin of this structure.

In the $^1\Pi \leftarrow {}^1\Sigma^+$ excitation only f level of $^1\Pi(v, J)$ can be excited in Q transition and e level of $^1\Pi(v, J)$ can be excited in the P or R transition. The fluorescence to the triplet state $a^3\Sigma^+$ can be allowed through mixing of a triplet state to the $B^1\Pi$ state, induced mainly by the spin-orbit interaction. Looking at the *ab initio* calculations we can estimate that the possible perturbing state is either the $c^3\Sigma^+$ or the $b^3\Pi$ state. H. Katô and coworkers state in their paper [69] that when the perturber is the $c^3\Sigma^+$ state, doublet progressions are always observed, independently of an excitation type, whereas when the $b^3\Pi$ state perturbs the $B^1\Pi$ state, doublets are observed at P or R excitation and triplets at Q excitation.

At the same time, analysis made by A. Stolyarov [92] showed that the $B^1\Pi$ state is mainly perturbed by the $c^3\Sigma^+$ state, whereas influence of the $b^3\Pi$ state is much less. And appearance of triplet and doublet progressions, nevertheless, can be explained with the $c^3\Sigma^+$ perturber model only as well (see Fig. 4.10). Selection rules for perturbations are $\Delta J = 0$, $e \leftrightarrow e$, $f \leftrightarrow f$ (except for the hyperfine perturbations). If the perturbing state is the $c^3\Sigma^+$ state, the $B^1\Pi(v, J_e)$ level interacts with the $c^3\Sigma^+(v, N = J, J)$ which results into fluorescence to $N'' = J + 1$ and $J - 1$ levels. The $B^1\Pi(v, J_f)$ level can interact with the $c^3\Sigma^+(v, N = J + 1, J)$ and $(v, N = J - 1, J)$ levels. This leads to appearance of progressions with transitions corresponding to $N'' = J - 2$, J and $J + 2$. If only one $c^3\Sigma^+$ state level is mixed with the $B^1\Pi$ state f level, then we see doublets with $N'' = J + 2$, J or $N'' = J - 2$, J depending on the perturbed $c^3\Sigma^+$ state level.

Assignment of the observed spectra was made using the $a^3\Sigma^+$ state hybrid potential from Ref. [73], based on the experimental data by Katô group [69]. Assignment was also checked, where it was possible, by finding the corresponding $B^1\Pi \rightarrow X^1\Sigma^+$ transition or checking laser resonance in B–X transition. Distinguishing between different isotopomers was simplified by observing the HFS of the triplet lines (see Section 4.4.3). The new vibrational numbering in the $a^3\Sigma^+$ state was established in this study (see below). An example of transitions to the $a^3\Sigma^+$ state is shown in Fig. 4.11.

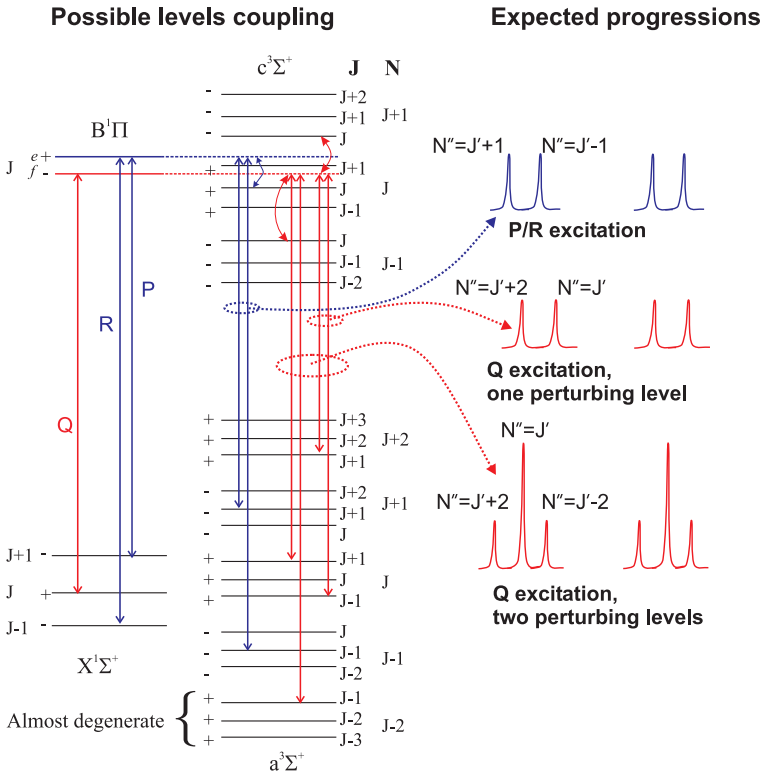

Figure 4.10. Schematic illustration for allowed transitions of the fluorescence to the $a^3\Sigma^+$ state induced by the spin-orbit interaction between the $B^1\Pi$ and $c^3\Sigma^+$ state levels following an excitation $B^1\Pi \leftarrow X^1\Sigma^+$. Here quantum number J is assumed to be even. If J is odd, the sign of parity (+ or −) should be exchanged.

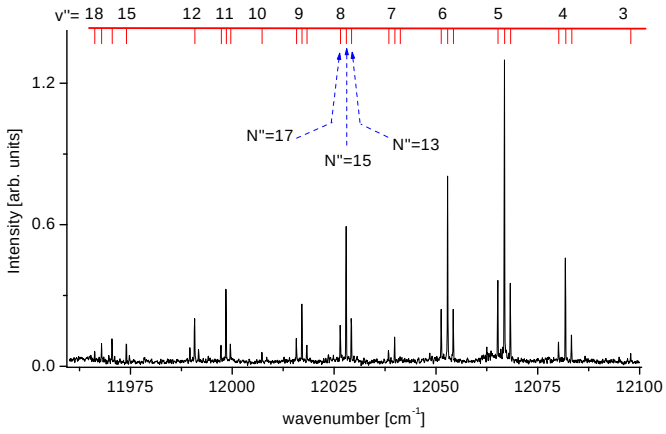

Figure 4.11. Progression to the $a^3\Sigma^+$ state in $Na^{85}Rb$ excited with a single mode Rh6G laser at frequency 16925.89 cm^{-1}. Corresponding singlet transition is $B^1\Pi\,(8, 15) \leftarrow X^1\Sigma^+\,(0, 15)$.

4.4.2 Transitions to near-dissociation levels

In order to observe transitions to weakly bound singlet and triplet ground state levels close to the atomic asymptote from a common upper level we took advantage of the long-range changeover, namely that close to the atomic asymptote the Hund's case (a) and (b) electronic states develop to the Hund's case (c) coupling and finally to the Hund's case (e) where the electronic angular momenta are uncoupled from the molecular axis. That is, the $c^3\Sigma^+$ state at long internuclear distances becomes a mixed state with triplet and singlet character giving rise to transitions to the ground $a^3\Sigma^+$ and $X^1\Sigma^+$ states. These transitions between case (c) states are indicated by arrows in Fig. 4.12.

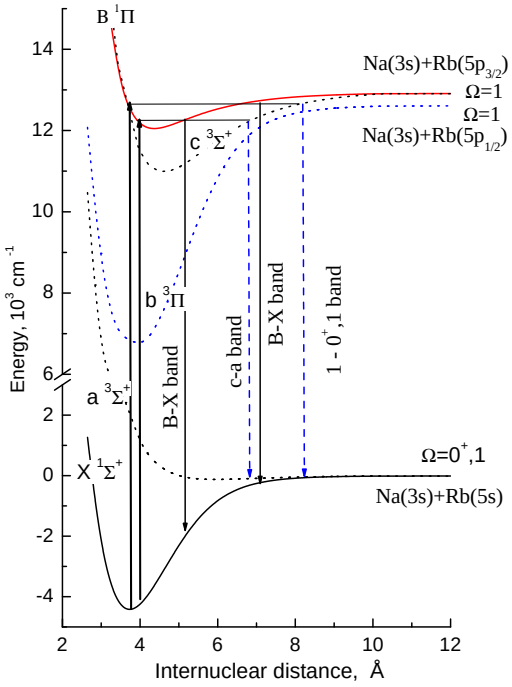

Figure 4.12. Excitation schemes for studying the electronic states correlating to the $Na(3S_{1/2})$ + $Rb(5S_{1/2})$ asymptote. For clarity the fluorescence bands are indicated only by the corresponding triplet or singlet component of the $B^1\Pi - b^3\Pi - c^3\Sigma^+$ complex.

In our experiments we observed several spectra which we interpret as long-range changeover. In Fig. 4.13 an example of the resolved fluorescence is shown when exciting a $B^1\Pi$ state $v'_B = 25$ level mixed with $c^3\Sigma^+$ state levels. Similarly to Fig. 4.5, bands to the $X^1\Sigma^+$ and $a^3\Sigma^+$ states are seen. In the same figure the calculated Franck-Condon factors (FCF) for $B^1\Pi \rightarrow X^1\Sigma^+$ transitions are shown as crosses. The FCFs were calculated applying a $B^1\Pi$ state potential based on the molecular constants from Ref. [70] and new measurements with polarization labeling spectroscopy [93]. They give reasonable agreement with the experimental intensities down to approximately 12700 cm^{-1}, where the FCFs predict the end of the B–X band. In reality this fluorescence progression is seen to be continuing down to 12500 cm^{-1}, where it appears simultaneously with the corresponding transitions to the $a^3\Sigma^+$ state from the common upper state level. These additional transitions to the $X^1\Sigma^+$ state arise due to the long-range changeover of the $c^3\Sigma^+$ state to the Hund's case (c).

A typical portion of the spectrum containing Q-type ($\Delta J = 0$) transitions with $J' = 19$ is shown in Fig. 4.14 reaching $v_a = 18$ of the $a^3\Sigma^+$ state and $v_X = 78$ of the $X^1\Sigma^+$ state. The assignment of

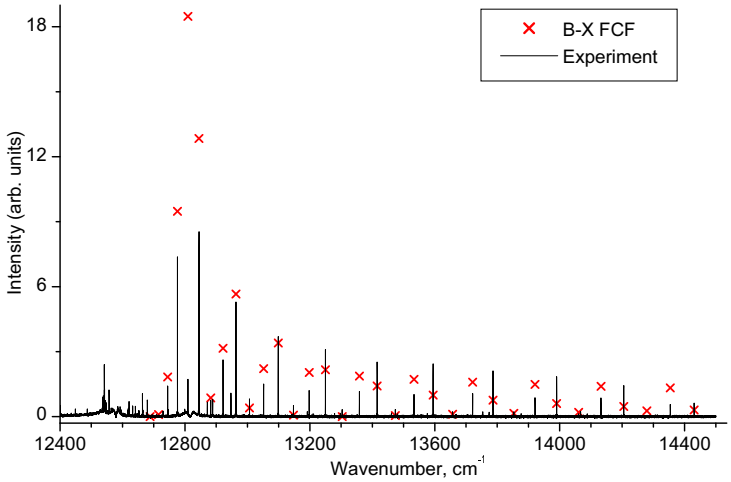

Figure 4.13. A comparison between the calculated Franck-Condon factors (FCF) for the B–X transitions (crosses) and the experimental intensities of the fluorescence progression excited by dye laser (Rh6G) at 17377.37 cm^{-1}. The absorption of the molecular fluorescence by the atomic Rb D2 line is the reason for low line intensities around 12800 cm^{-1} compared to prediction by FCF. The band seen below 12600 cm^{-1} is an overlap of singlet and triplet structure.

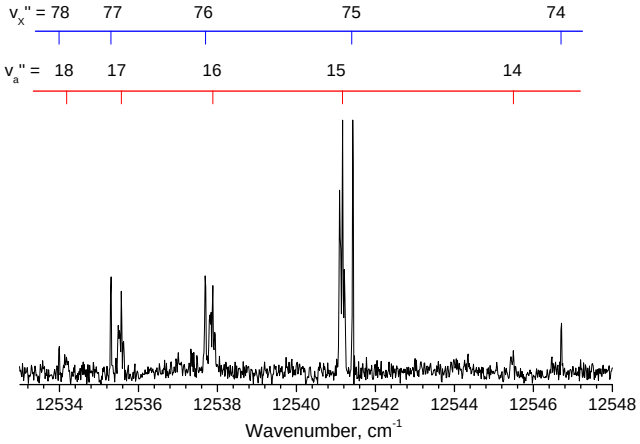

Figure 4.14. Transitions to levels near the $Na(3S_{1/2})$+$Rb(5S_{1/2})$ asymptote for $J'' = N'' = 19$ of $Na^{85}Rb$ excited with Rh6G laser at frequency 17377.29 cm^{-1}. The assignment of the triplet state levels is according to the new vibrational numbering established in this study.

the triplet state levels is according to the new vibrational numbering established in this study below. Similar spectra were recorded for a wide range of J' quantum numbers ($J' = 10 - 23$) including also P- and R-type ($\Delta J = \pm 1$) transitions. In this way abundant information on the near asymptotic levels of the $a^3\Sigma^+$ and $X^1\Sigma^+$ states was collected. These spectra are particularly interesting also because they show the whole pattern of singlet and triplet levels for a given rotational quantum number close to the asymptote, so it should be possible to establish the coupling between the the $a^3\Sigma^+$ and $X^1\Sigma^+$ state levels through hyperfine interaction and to distinguish the exchange energy.

It is worth mentioning that in case of excitation above the ($3S+5P_{1/2}$) asymptote no such progressions were observed, probably due to pre-dissociation of the $\Omega = 1$ ($3S+5P_{3/2}$) levels due to coupling to the continuum above the asymptote ($3S+5P_{1/2}$).

The total data set for the $a^3\Sigma^+$ state consists of more than 900 transition frequencies to 490 energy levels as shown in Fig. 4.15 for both isotopomers $^{23}Na^{85}Rb$ and $^{23}Na^{87}Rb$. The experimental uncertainty was estimated to be 0.003 cm^{-1} for lines recorded with high signal-to-noise ratio (SNR > 5). The data set for the $X^1\Sigma^+$ state obtained previously, see [dis2], was correspondingly enriched by about 250 transitions adding some 150 new rovibrational levels.

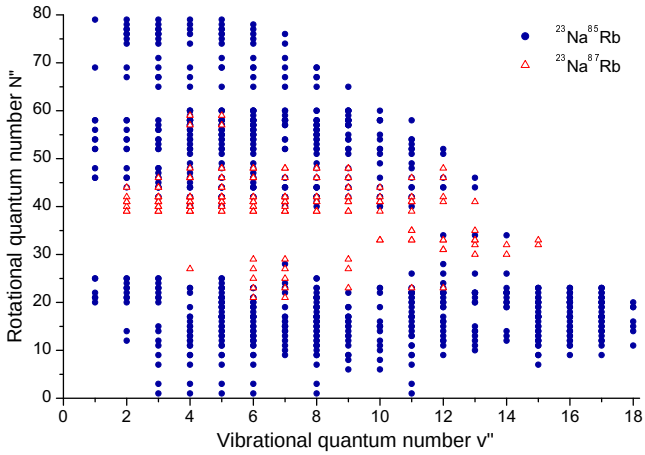

Figure 4.15. The range of vibrational and rotational quantum numbers of the observed energy levels in the $a^3\Sigma^+$ state of $Na^{85}Rb$ and $Na^{87}Rb$.

4.4.3 Analysis of the hyperfine splitting of the $a^3\Sigma^+$ state levels

At the resolution used in the experiments, the hyperfine structure (HFS) of the triplet lines were partially resolved (see Fig. 4.16). The hyperfine splitting of the $a^3\Sigma^+$ levels is caused by the Fermi contact interaction, and the appropriate theory was described in detail by Kasahara *et al.* [72] for $Na^{85}Rb$ in low vibrational levels of the $a^3\Sigma^+$ state (see also Section 2.7). The effective Hamiltonian for the electronic spin $\mathbf{S}$ and the nuclear spin $\mathbf{I}$ defines the interaction parameters:

$$\mathbf{H}_{hfs} = A_{\mathrm{Rb}} \cdot \mathbf{S}_{\mathrm{Rb}} \cdot \mathbf{I}_{\mathrm{Rb}} + A_{\mathrm{Na}} \cdot \mathbf{S}_{\mathrm{Na}} \cdot \mathbf{I}_{\mathrm{Na}} \tag{4.3}$$

From the experimental spectra the A_{Na} and A^{85}_{Rb} constants were determined [72] which describe the observed splitting within a Hund's case ($b_{\beta S}$) coupling scheme (see Figs. 2.2 and 4.17). Generally, the molecular coupling parameters correspond to the atomic constants A. But for atoms forming a diatomic molecule the dependence of these parameters on the bond length and thus on the vibrational and rotational quantum numbers cannot be excluded (see Ref. [94]). Within the resolution of our experiment we recorded partially resolved hyperfine structure of the $a^3\Sigma^+$ state levels and since our data covered a

much broader range of $a^3\Sigma^+$ levels of both isotopomers than in Ref. [72], we checked the dependence of $A_{\rm Na}$, $A_{\rm Rb}^{85}$ and $A_{\rm Rb}^{87}$ on the vibrational and rotational quantum numbers and determined the $A_{\rm Rb}^{87}$ constant for $Na^{87}Rb$ for the first time, see Fig. 4.18.

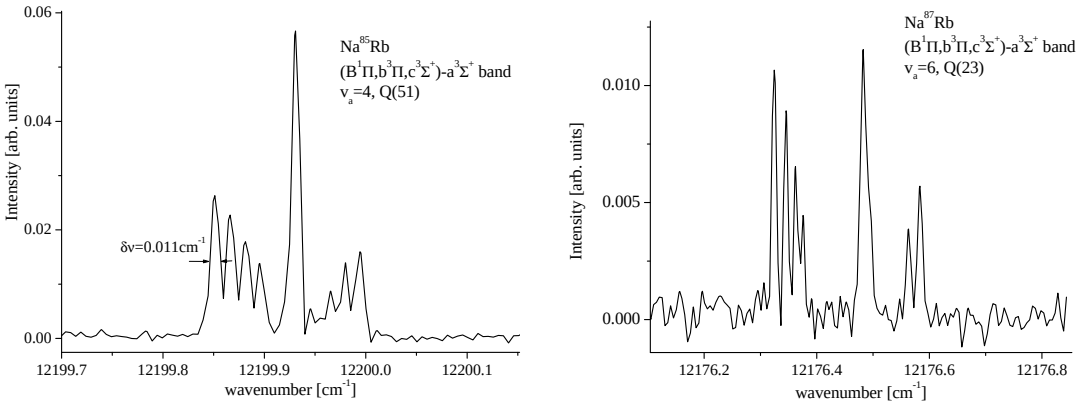

Figure 4.16. Hyperfine splitting of the transitions to the $a^3\Sigma^+$ state in $Na^{85}Rb$ and $Na^{87}Rb$.

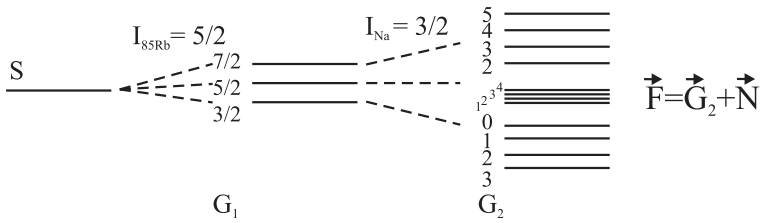

Figure 4.17. Scheme of momenta coupling and formation of the HFS in $Na^{85}Rb$.

In Fig. 4.16 examples of the observed hyperfine splitting of transitions to $a^3\Sigma^+$ state levels in $Na^{85}Rb$ and $Na^{87}Rb$ are shown. Within the resolution of the present experiment these splittings are the same in each isotopomer group for almost all observed rovibrational levels of the $a^3\Sigma^+$ state. The only feature, where slight deviations from the pattern in Fig. 4.16 were observed, is for $v_a = 16$ in $Na^{85}Rb$. These deviations, however, as it was later justified by the analysis, are due to local perturbation by the $v_X = 76$ level of the $X^1\Sigma^+$ state separated by only several tenths of a wavenumber. Therefore, extending the range of observations from Ref. [72], we found that the hyperfine splitting of the $a^3\Sigma^+$ state for both isotopomers is characterized by two constants which are very close to those of the corresponding free atoms. A comparison for $A_{\rm Rb}^{85}$ and $A_{\rm Na}^{23}$ was done in Ref. [72]. Our value for $A_{\rm Rb}^{87} = 0.113(1)$ cm^{-1} (see Fig. 4.18) also agrees with the atomic parameter 0.11399 cm^{-1} [95].

The hyperfine-structure-free positions of the triplet state levels are shifted from the central component of the hyperfine pattern (see Fig. 4.16) by 0.017 cm^{-1} for $Na^{85}Rb$ and by 0.062 cm^{-1} for $Na^{87}Rb$. Using these energy levels, potentials without HFS corrections are obtained below.

4.4.4 Single potential fit for the $a^3\Sigma^+$ state

At the first stage of the analysis we applied a single-potential approach for describing the experimental observations of the $a^3\Sigma^+$ state. The levels corrected for hyperfine structure were used to construct a potential curve for the $a^3\Sigma^+$ state in a manner similar to that used for the $X^1\Sigma^+$ state. For short and intermediate internuclear distances the potential curve is represented by a set of points connected with natural cubic spline functions [48]. In order to reduce any undesired oscillations of the curve close to

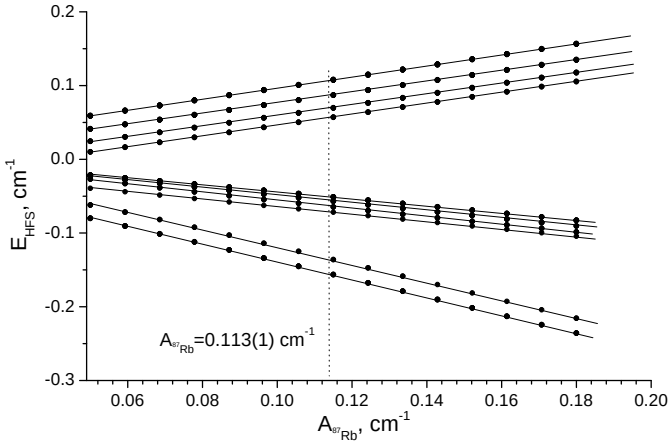

Figure 4.18. HFS splitting in the $a^3\Sigma^+$ state of $Na^{87}Rb$ as dependent on the HFS constant A^{87}_{Rb}. The dotted vertical line shows the A^{87}_{Rb} value, which corresponds to the observed HFS splitting.

the asymptote caused by too high flexibility of the spline representation we applied the regularization technique [50]. Initially, the potential was adjusted to fit all constructed 1935 differences between the observed line positions in both isotopomers. Once relatively good agreement between calculated and measured differences was achieved, we excluded high vibrational levels from the fit, since we expected possible shifts due to their interactions with the $X^1\Sigma^+$ state.

As a first approximate potential for the fit we adopted the curve from Ref. [73]. Unfortunately, all our attempts to reach quantitative agreement with the experimental observations failed and we obtained systematic deviations up to 0.05 cm^{-1}. The same happened when trying to fit data only for one of the isotopomers. After analysis of additional second-order spin-spin and spin-rotation interactions, we concluded that their magnitude should be much smaller than our experimental uncertainty and, therefore, they cannot explain the deviations. Then we decided to revise the vibrational numbering of the $a^3\Sigma^+$ state established for the first time in Ref. [69] and afterwards used in Ref. [73]. In fact, our observed spectra do not show any vibrational level below the level named $v_a = 0$ in Ref. [69]. However, when we shifted the vibrational numbering by one vibrational quantum, i.e. now the lowest observed levels became $v_a = 1$, we achieved almost immediately a good fit for $v_a < 15$ in $Na^{85}Rb$ and the same potential was able to describe the experimental observations in $Na^{87}Rb$ within their uncertainty without additional adjustment. The high quality of the fit including low vibrational levels ($v_a = 1$) from both isotopomers with a single potential curve is taken as a proof for the correctness of this new assignment. Additionally, we tried also fits by shifting the vibrational numbering by two and three quanta which were not successful.

4.4.5 Analysis of the $X^1\Sigma^+$ and $a^3\Sigma^+$ states by coupled channels calculations

The final forms of the $X^1\Sigma^+$ and $a^3\Sigma^+$ state potentials were determined in a coupled channels analysis which takes into account the hyperfine interaction between these states.

The absolute position of the $a^3\Sigma^+$ state in the energy scale with respect to the $X^1\Sigma^+$ state was adjusted so that the spacings between eigenenergies of both potentials agree with the separation of spectral lines decaying to the corresponding energy levels from a common upper state level (e.g., see Fig. 4.14). Here the hyperfine splitting was added to the eigenenergies of the triplet state. This procedure was performed for levels far from the asymptote to avoid possible shifts due to the hyperfine interaction between the X and a states.

For large internuclear distances (typically larger than 11 Å) we adopted the standard long-range form of molecular potentials:

$$U_{\rm LR}(R) = D - \frac{C_6}{R^6} - \frac{C_8}{R^8} - \frac{C_{10}}{R^{10}} \pm E_{\rm ex} \tag{4.4}$$

where the exchange contribution is given by

$$E_{ex} = A_{ex} R^{\gamma} \exp(-\beta R). \tag{4.5}$$

Here D is the energy of the atomic asymptote with respect to the minimum of the $X^1\Sigma^+$ state. It coincides with the dissociation energy of this state, D_e^X. The exchange energy is repulsive for the triplet state (plus sign in (4.4)) and attractive for the singlet state (minus sign). All parameters in Eqs. (4.4,4.5) are the same for the $X^1\Sigma^+$ and $a^3\Sigma^+$ states.

As a first guess we used the long-range parameters derived for the $X^1\Sigma^+$ state [dis2] also for the triplet $a^3\Sigma^+$ state. For the exchange energy we adopted the estimate of Ref. [82]. The connecting points between the short and the long-range potentials were chosen such that a continuous and smooth transition between the two representations for R below or above the connection point R_o is ensured.

Since the analysis of the molecular hyperfine structure has shown that the corresponding splitting is independent of the vibrational and rotational structure and agrees with the atomic values, the interactions that couple the $X^1\Sigma^+ - a^3\Sigma^+$ system can be modeled by the atomic hyperfine splitting of the corresponding atoms. The total Hamiltonian describing the interactions between ground state Na and Rb atoms is similar to that given in Ref. [91] and is adapted for the case of different atomic species. It contains the kinetic energy operator for the relative radial motion between two atoms, the Born-Oppenheimer potentials for the $X^1\Sigma^+$ and $a^3\Sigma^+$ states, a hyperfine contact interaction for Na atom and Rb atom, and the nuclear rotation. Weak magnetic spin-spin and second-order spin-orbit interactions can be neglected for the purpose of this study. These interactions become important when the accuracy in the determination of the position of weakly bound levels reaches a few megahertz (10^{-4} cm^{-1}). Details on such calculations have been discussed in Ref. [63] for the case of Na_2. The coupled channels code used in the present studies is based on Fourier Grid Hamiltonian method [96].

Preliminary coupled channels calculations with potential curves determined in single channel fits showed that the shifts of the calculated energy levels with respect to the unperturbed ones, i.e. the eigenvalues of the single potentials, exceed the experimental uncertainty only for $v_X \geq 74$ of the $X^1\Sigma^+$ state and $v_a \geq 14$ of the $a^3\Sigma^+$ state. The strongest one is the coupling between the $v_X = 76$ of the $X^1\Sigma^+$ state and $v_a = 16$ of the $a^3\Sigma^+$ state in agreement with our experimental observations on the hyperfine structure. For these levels the coupling leads to shifts of the order of 0.02 cm^{-1}, see Fig. 4.19. Generally however, although shifted, the whole pattern of the hyperfine splitting is preserved so that the levels can still be classified as singlet and triplet in the studied region. This is further confirmed by calculating the expectation values of the magnitude of the total spin operator **S** for levels within the coupled system; these differ by no more than few percent from 0 or 1 for the observed levels, with exception for levels closer to the asymptote.

As a next step of analysis, the molecular potentials for the singlet and triplet ground states were fitted by taking into account the coupling between them. The coupled channels calculations are quite time consuming due to the large number of observed rotational quantum numbers, and it would be inefficient to fit the potentials directly as a coupled system. The following iterative procedure was adopted instead: first the shifts of the calculated levels of the coupled system with respect to the eigenenergies of single potentials were determined as a first order correction, because the initial single-channel potentials were already a good approximation. Therefore, the experimental data were corrected by the corresponding shifts and molecular potentials were fitted to the corrected experimental data in a single channel fit. Thus a better approximation of the potentials was obtained and the procedure was repeated until the experimental data were described by the coupled channels calculations within the experimental uncertainties.

In the single channel fit only the dissociation energy, the dispersion coefficients and the exchange energy parameter A_{ex} were adjusted assuming the long-range expression (4.4) to be valid beyond R_o, approximately 11 Å. These parameters were fitted simultaneously to the experimental data for the $X^1\Sigma^+$ and the $a^3\Sigma^+$ states. When a change of the long-range parameters led to discontinuity in the connecting

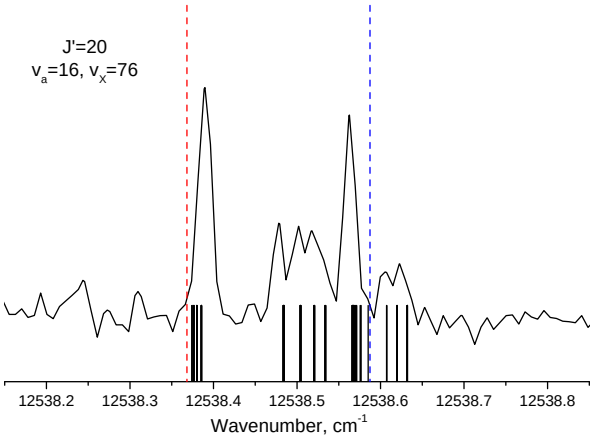

Figure 4.19. Piece of spectrum excited with Rh6G laser at 17377.30 cm^{-1}. Dashed lines denote the eigenenergies according to the single channel triplet ($v_a = 16$) and singlet ($v_X = 76$) calculations.

point R_o, the connecting point was shifted and/or separate fits of the pointwise representations of the potentials were carried out.

In several iterations we obtained the potentials of $X^1\Sigma^+$ and $a^3\Sigma^+$ states, listed in Tables 4.6 and 4.7, respectively. For convenience, quantities like T_e (position of the potential minimum), R_e (equilibrium distance) and D_0 (dissociation energy with respect to the first rovibrational level $v'' = 0$, $J'' = 0$) are also given. In order to assess the quality of the fitted potentials, in addition to the experimental data sets sorted separately for transitions to the singlet and the triplet state, a new combined data set was constructed. It contains all transitions to high vibrational levels of both states ($v_X \geq 74$ and $v_a \geq 14$). Differences between these selected transition frequencies were calculated not only between the transitions to a given electronic state, as done before, but also differences between transitions to different states were formed. This is possible since by a single excitation transitions to both the singlet and the triplet state were observed. Extremely precious are progressions appearing by the so called long-range changeover, since they contain information about high vibrational levels of both states and allow the separation between the states near the asymptote to be precisely estimated. The combined data set contains 555 transition frequencies forming about 3700 differences. The potentials from Tables 4.6 and 4.7 reproduce these differences with a standard deviation $\sigma = 0.0025$ cm^{-1} and a dimensionless standard deviation of $\bar{\sigma} = 0.63$ and they reproduce the total experimental data for the triplet state with $\sigma = 0.0035$ cm^{-1} and $\bar{\sigma} = 0.59$ and for the singlet state with $\sigma = 0.0032$ cm^{-1} and $\bar{\sigma} = 0.73$.

Figure 4.20 gives the magnitude of singlet-triplet coupling by the deviations of energy levels of the $X^1\Sigma^+$ and the $a^3\Sigma^+$ states calculated with coupled channels code from the eigenvalues of the single channel potentials. The several points for each vibrational level correspond to different rotational quantum numbers ($7 < J''(N'') < 27$). The top and bottom axis, v_a and v_X, respectively, are scaled such that the values v_a, v_X of closest level approach form a vertical line. The larger deviations appear for higher J'' (N''). Note that the deviations for singlet state levels are larger than for the corresponding triplet state levels. Therefore, long-range analysis based only on singlet transitions would introduce larger systematic distortions in the fitted potential curve for large internuclear distances than analysis based only on triplet transitions. This statement can be indirectly confirmed making single channel calculations with the potentials from Tables 4.6 and 4.7 showing that the $a^3\Sigma^+$ state potential reproduces differences between levels with $v_a > 7$ with a $\bar{\sigma} = 0.70$ (the coupled calculations give $\bar{\sigma} = 0.62$) while the $X^1\Sigma^+$ state potential reproduces differences between levels with $v_X > 68$ with a $\bar{\sigma} = 2.18$ (the coupled calculations give $\bar{\sigma} = 0.52$). So within the present experimental uncertainty the triplet state can still be considered as a single state, whereas a single channel treatment of the $X^1\Sigma^+$ state will lead to incorrect description

Table 4.6. Pointwise representation of the potential energy curve for the $X^1\Sigma^+$ state of NaRb.

R [Å]	U [cm^{-1}]	R [Å]	U [cm^{-1}]
2.100000	23623.67465	5.791989	3880.39592
2.200000	17634.41477	5.973808	4088.60966
2.300000	13279.18859	6.155626	4262.33458
2.400000	10069.56048	6.337444	4405.67319
2.500000	7667.49769	6.519263	4522.91885
2.600000	5874.22172	6.701081	4618.17079
2.700000	4521.74692	6.882899	4695.19866
2.800000	3427.90598	7.064718	4757.28897
2.900000	2528.63531	7.246536	4807.26121
3.000000	1798.65045	7.428355	4847.46365
3.131998	1060.60559	7.610173	4879.81088
3.263996	544.13656	7.791991	4905.89082
3.395993	215.36397	7.973810	4926.95998
3.527991	43.57832	8.155628	4944.02973
3.659989	0.83395	8.499301	4968.08811
3.791987	62.11989	8.699301	4978.43703
3.973805	276.44925	8.899301	4986.78123
4.155624	597.14349	9.192121	4996.27537
4.337442	984.16758	9.514223	5003.97364
4.519260	1405.59678	9.942941	5011.19667
4.701079	1836.47101	10.461689	5016.98016
4.882897	2257.79571	11.152144	5021.73265
5.064716	2655.74803	12.101429	5025.42308
5.246534	3020.92992	13.050715	5027.33721
5.428352	3347.84205	14.000000	5028.47884
5.610171	3634.22011		

$D = 5030.50235$ cm^{-1}	
$R_o = 11.2967$ Å	
$C_6 = 1.3237 \cdot 10^7$ cm^{-1}Å^6	$A_{ex} = 2.8609 \cdot 10^4$ cm^{-1}Å$^{-\gamma}$
$C_8 = 2.9889 \cdot 10^8$ cm^{-1}Å^8	$\gamma = 5.0081$
$C_{10} = 1.5821 \cdot 10^{10}$ cm^{-1}Å^{10}	$\beta = 2.2085$ Å^{-1}
$T_e^X = 0$ cm^{-1}	$R_e^X = 3.6434$ Å
$D_e^X = 5030.502(50)$ cm^{-1}	$D_0^X = 4977.187(50)$ cm^{-1}

Table 4.7. Pointwise representation of the potential energy curve for the $a^3\Sigma^+$ state of NaRb.

R [Å]	U [cm^{-1}]	R [Å]	U [cm^{-1}]
2.944440	29489.89467	6.468399	4872.49275
3.155560	18461.93317	6.605337	4882.75826
3.366670	12363.70802	6.794944	4896.83178
3.577780	8991.52099	6.984550	4910.34530
3.788890	7126.77387	7.174157	4923.07187
4.000000	6095.47898	7.363764	4934.83385
4.198190	5552.35782	7.553371	4945.59408
4.396380	5237.10044	7.990520	4966.55716
4.594570	5062.99324	8.427668	4982.64596
4.792760	4957.08727	8.864817	4994.72299
4.990949	4890.76470	9.301966	5003.67683
5.189139	4852.15516	9.739114	5010.27403
5.387328	4832.98126	10.176263	5015.16200
5.585518	4827.17289	10.941010	5020.80312
5.783708	4830.40026	11.705758	5024.24404
5.920646	4836.15057	12.470505	5026.30776
6.057584	4843.78306	13.235253	5027.62932
6.194522	4852.68409	14.000000	5028.49121
6.331461	4862.36273		

$D = 5030.50235$ cm^{-1}	
$R_o = 11.3370$ Å	
$C_6 = 1.3237 \cdot 10^7$ cm^{-1}Å^6	$A_{ex} = 2.8609 \cdot 10^4$ cm^{-1}Å$^{-\gamma}$
$C_8 = 2.9889 \cdot 10^8$ cm^{-1}Å^8	$\gamma = 5.0081$
$C_{10} = 1.5821 \cdot 10^{10}$ cm^{-1}Å^{10}	$\beta = 2.2085$ Å^{-1}
$T_e^a = 4827.14727$ cm^{-1}	$R_e^a = 5.6003$ Å
$D_e^a = 203.355(50)$ cm^{-1}	$D_0^a = 193.365(50)$ cm^{-1}

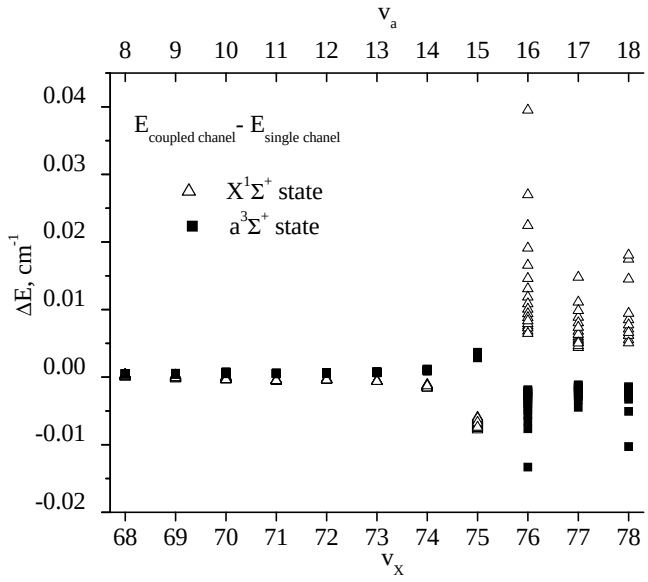

Figure 4.20. Deviation ΔE of the energy level positions for the $a^3\Sigma^+$ state (solid squares) and the $X^1\Sigma^+$ state (open triangles) calculated with coupled channels code from the eigenvalues of the single channel potentials. The $a^3\Sigma^+$ state vibrational quantum numbers v_a are given on the top x-axis, whereas $X^1\Sigma^+$ state ones v_X – on the bottom x-axis. Several points for each vibrational level correspond to different rotational quantum numbers ($J'' = N'' = 7 - 27$).

of the long-range potential.

The combined analysis on ground state and lowest triplet state potentials has led to a revision of the dissociation energy of the $X^1\Sigma^+$ state derived in [dis2]. The difference between the minimum of the $X^1\Sigma^+$ state and the Na($3S_{1/2}$)-Rb($5S_{1/2}$) atomic asymptote (with respect to the center of gravity of the hyperfine structure) amounts to $D_e^X = 5030.502$ cm^{-1} with an estimated uncertainty of ± 0.05 cm^{-1}. This should be compared to the 5030.848 cm^{-1} from Ref. [dis2] and the 5030.75 cm^{-1} from Ref. [73] in order to highlight the importance of the coupled channel analysis. The value of the dissociation energy with respect to the first rovibrational level amounts to $D_0^X = 4977.187$ cm^{-1}. The corresponding values for the triplet ground state are $D_e^a = 203.355$ cm^{-1} and $D_0^a = 193.365$ cm^{-1}. The D_e^a differs significantly from the most recent value from Ref. [73] not only due to the improved experimental data set, but mainly due to the new vibrational assignment established in this study.

4.4.6 Discussion

The estimation of the uncertainties of the long-range parameters is a problematic question. In the work on Ca_2 $X^1\Sigma^+$ state [97] the parameters for the long-range part of interatomic potential were determined experimentally by fitting them to abundant and accurate experimental data, and confidential intervals for the fitting parameters were obtained from the Monte Carlo simulations. In contrary to the situation on the Ca_2 ground state asymptote, the structure of the alkali metal Na and Rb atomic pair is much more difficult to model due to the presence of nonzero electronic and nuclear spins. Therefore, the direct estimation of the parameter uncertainties using Monte Carlo simulations would be very time-consuming.

Moreover, the experimental data in this study cover a narrower part of the long-range potential than in the Ca_2 case. On the long-range side the outermost classical turning point in NaRb at 15.6 Å ($v_X'' = 78$, $J'' = 20$) has to be compared with 20 Å in the case of Ca_2. Due to difference in the electronic structure of the Rb atom (open valence shell) and the Ca atom (closed subshell) the pure long-range

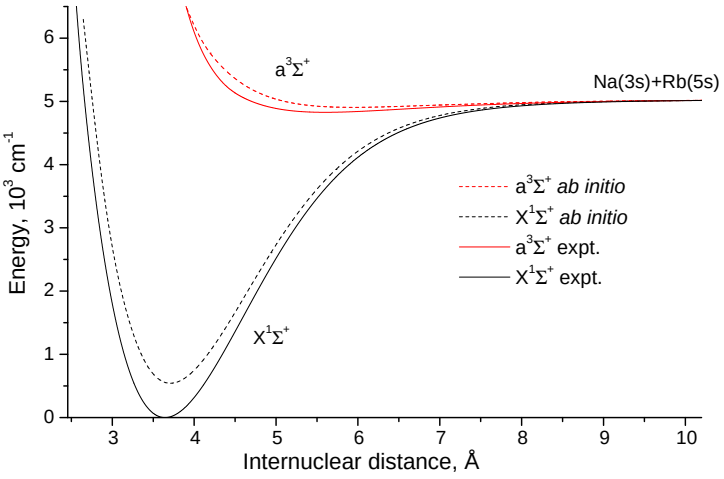

Figure 4.21. Comparison of present empirical and *ab initio* [34] potential energy curves.

potential expression (4.4) cannot be extended to as small internuclear distances as for Ca_2. The narrower range not only increases the uncertainty of the fitted parameters, but also increases the ambiguity in connecting the long-range potential to the pointwise representation (this problem was discussed already in Ref. [97]). Additionally, a new degree of freedom was added in the fit—the term A_{ex} for the exchange energy expression (4.5), the correlation of which with C_6 term was discussed in Ref. [97].

On the other hand, a single set of long-range parameters was fitted to data belonging to two different electronic states which gives desired constraint for the variation of the long-range parameters. For example, in the successive iterations the D value varied only between 5030.49 cm^{-1} and 5030.56 cm^{-1}, while the value of C_6 between $1.300 \cdot 10^7$ cm^{-1} $Å^6$ and $1.354 \cdot 10^7$ cm^{-1} $Å^6$. Although these intervals cannot be treated as some confidential limits, they still give some indication about the expected uncertainty of the fitted parameters.

The difficulty to provide the fitted long-range parameters with a rigorous estimation of their uncertainty is not only due to limited size of the present experimental data set, but also because of one of the main requirements, i.e. the smooth connection between the long-range and the pointwise representation of the potentials, was not built into the fit. The problem here is not just technical, but also conceptual, since in this case the uncertainty of the short-range potential energy curve should be estimated, which is delicate in the regions with a small amount of experimental data, because the results become model dependent (see, e.g., [55, 59, 50]).

It is worth mentioning that in the present analysis a direct experimental estimation of the exchange energy parameter A_{ex} was done. Since the other parameters (i.e., β and γ) were fixed to their estimated values from Ref. [82] and were not fitted, we would avoid commenting directly on the physical meaning of A_{ex} alone. We would rather state that all three parameters together give a good representation of the exchange energy contribution, derived from a direct fit to the experimental data.

Without being able to associate reliable uncertainty limits to the experimental dispersion coefficients and taking into account the strong correlation between them, we cannot compare strictly our values with the recent *ab initio* predictions [80, 81], although they are close to each other. In order to check the consistency of the theoretical calculations we tried to construct potential curves using values for C_6 and C_8 from [80, 81] and fitting only C_{10} and A_{ex} to the experimental data, corrected as discussed in the previous section using the potentials from Tables 4.6 and 4.7. The new potentials reproduce the experimental observations with similar quality which confirms the reliability of the theoretical coefficients. The analytic representations of these curves (2.55) are given in Table III of the EPAPS in [dis3].

Empirical $X^1\Sigma^+$ and $a^3\Sigma^+$ state PECs are compared to the *ab initio* ones in Fig. 4.21.

The obtained PECs of the $X^1\Sigma^+$ and $a^3\Sigma^+$ states were applied for calculating of scattering lengthes and prediction of Feschbach resonances for Na-^{85}Rb and Na-^{87}Rb different quantum states (see [dis3]), which is important for cold collision experiments with Na-Rb pairs. Results were compared to the results of other groups [82, 83, 84, 85].

4.4.7 Results and conclusions

1. New high-resolution LIF data were collected for the $a^3\Sigma^+$ state of NaRb using the FTS method. More than 900 transition frequencies to 490 energy levels were identified. The range of observed vibrational and rotational quantum numbers is $v'' = 1 - 18$ and $N'' = 1 - 80$. The typical experimental uncertainty is 0.003 cm^{-1}.

2. The new vibrational numbering in the $a^3\Sigma^+$ state was established from the isotopic effect in this study: vibrational numbering was changed by +1, compared to the one used in Ref. [69].

3. Data on the high-lying levels of the $a^3\Sigma^+$ and $X^1\Sigma^+$ state were obtained simultaneously using the long-range changeover in the $c^3\Sigma^+$ state. The data set for the $X^1\Sigma^+$ state obtained previously (see [dis2]) was correspondingly enriched by about 250 transitions adding some 150 new rovibrational levels. Turning point of the last observed level ($v''_X = 78$, $J'' = 20$) is 15.6 Å being approximately 1 cm^{-1} below the asymptote.

4. Both $X^1\Sigma^+$ and $a^3\Sigma^+$ states potentials were fitted simultaneously to spline-pointwise potential energy curves smoothly connected to the long-range potential, taking into account the hyperfine mixing of these states close to the asymptote. Analysis revealed that the shifts of the calculated energy levels with respect to the unperturbed ones, i.e. the eigenvalues of the single potentials, exceed the experimental uncertainty for $v_X \geq 74$ of the $X^1\Sigma^+$ state and $v_a \geq 14$ of the $a^3\Sigma^+$ state. New potentials reproduce experimental frequency differences for the $a^3\Sigma^+$ state with $\sigma = 0.0035$ cm^{-1} and $\bar{\sigma} = 0.59$ and for the $X^1\Sigma^+$ state with $\sigma = 0.0032$ cm^{-1} and $\bar{\sigma} = 0.73$.

5. Long-range coefficients C_6, C_8, C_{10}, as well as exchange energy parameter A_{ex} were fitted. Dispersion potential is in good agreement with the *ab initio* one.

6. New, more precise values of dissociation energies are obtained for both $X^1\Sigma^+$ and $a^3\Sigma^+$ states: $D_e^X = 5030.502 \pm 0.05$ cm^{-1} and $D_e^a = 203.355 \pm 0.05$ cm^{-1}.

7. For not confusing the reader with three different $X^1\Sigma^+$ state potentials, it should be stressed what are their differences. The MLJ potential provides reliable predictions, but of limited accuracy (ca. 0.1 cm^{-1}) and in a limited quantum number range, defined by the experimental data. $X^1\Sigma^+$ state potential from [dis2] allows for highly accurate predictions up to v''=73 and in this range is of the same quality as the potential from [dis3]. For $v'' \geq$74 hyperfine mixing of the a and X state should be taken into account, therefore potential from [dis3] is recommended.

8. New potentials allowed reliable predictions of scattering lengthes and Feshbach resonances, necessary for cold collision experiments with Na-Rb pairs.

4.5 NaRb $C^1\Sigma^+$ state [dis4]

We present results of the first detailed experimental study of the $C^1\Sigma^+$ state of the NaRb molecule. During the study of the ground state of NaRb, done in Riga [dis1] and particularly in Hannover by Fourier-transform spectroscopy of laser-induced fluorescence [dis2], it turned out that a lot of information about the excited $C^1\Sigma^+$ and $D^1\Pi$ states was available from the recorded spectra. Here the $C^1\Sigma^+$ state analysis based on these experimental data and newly derived data by colleagues from the Institute of Physics and Institute of Experimental Physics in Warsaw is presented.

4.5.1 Observations and term value analysis

The experimental details have been described in Section 3.2. Among the lasers used for the $X^1\Sigma^+$ state studies Nd:YAG and Ar^+ laser lines 514.5 and 501.7 nm excited not only the $D^1\Pi - X^1\Sigma^+$ transitions but also the $C^1\Sigma^+ - X^1\Sigma^+$ transitions. A single mode, frequency doubled Nd:YAG laser with frequency varied between 18787.25 cm^{-1} and 18788.44 cm^{-1} gives rise to 18 $C^1\Sigma^+ \rightarrow X^1\Sigma^+$ progressions (see spectrum example in Fig. 4.4). The range of v' covered in the $C^1\Sigma^+$ state by the Nd:YAG laser is $v' = 21 - 30$. The Ar^+ ion laser line at 514.5 nm also efficiently excites transitions in the $C^1\Sigma^+ \leftarrow X^1\Sigma^+$ system. Here a range of $v' = 32 - 44$ in the $C^1\Sigma^+$ state was obtained. Overall, 12 progressions were assigned. The Ar^+ ion laser line 501.7 nm also excited $C^1\Sigma^+ \leftarrow X^1\Sigma^+$ transitions in NaRb, however, the resulting fluorescence was very weak and we were only able to observe it at higher temperatures (620 K). The only identified progression originates from $v' = 46$. Finally, a term value for $v' = 5$ was obtained from a weak $C^1\Sigma^+ \rightarrow X^1\Sigma^+$ LIF spectrum excited by a Rhodamine 6G dye laser.

Due to the presence of argon buffer gas and very high signal-to-noise ratio, several strong fluorescence lines were accompanied by a large number of collisionally-induced rotational satellites from levels $(v', J' \pm \Delta J)$ with ΔJ up to 12 (see Fig. 4.22). The analysis of these satellites has increased the Fourier data set for the $C^1\Sigma^+$ state significantly. It also allowed us to establish a relative numbering of the rovibrational levels of the $C^1\Sigma^+$ state. Overall, from the analysis of the FTS spectra we obtained 138 term values of $Na^{85}Rb$ and 66 of $Na^{87}Rb$ $C^1\Sigma^+$ state with undoubtedly assigned rotational quantum numbers by using the eigenenergies of the ground state potential from Ref. [dis2].

The assignment of the excited $C^1\Sigma^+$ state levels for the observed LIF progressions was made in two steps. First, a rotational and isotopomer assignment was established using the $X^1\Sigma^+$ state PEC [dis2]. Then the energy of the excited state level was obtained by adding the experimental transition frequencies to the respective ground state term values calculated from the PEC. Relative vibrational numbering was established from v', J' term values plotted against $J'(J'+1)$. Initial absolute numbering was based on the so-called difference-based potential, which was used in order to improve the reliability of the theoretical calculations [34]. Following the idea of Ref. [4], first the difference between the ground state and the $C^1\Sigma^+$ state *ab initio* potentials was calculated and then the result was added to the experimental potential of the $X^1\Sigma^+$ state of Ref. [dis2]:

$$U_{\mathrm{C}}^{dif}(R) = U_{\mathrm{X}}^{expt}(R) + \left(U_{\mathrm{C}}^{ab\ initio}(R) - U_{\mathrm{X}}^{ab\ initio}(R)\right). \tag{4.6}$$

The basic idea shared with Ref. [4] is that there are contributions, which are neglected in the *ab initio* calculations, being common for different electronic states. Therefore, usually the accuracy of the difference between two *ab initio* PECs is expected to be better than the quality of the individual potentials. Although this was stated for a specific *ab initio* approach in Ref. [4], here we applied a similar procedure to the calculations of Ref. [34] and found that it gives quite good results. The initial v' numbering suggested using the difference-based potential was later confirmed.

As has been already discussed, e.g. in Ref. [59], if exciting the molecular sample with a single mode laser and observing the fluorescence in a direction parallel to the laser beam, the resulting fluorescence does not suffer from Doppler broadening. The line frequencies, however, can be shifted from the Doppler-free values within the Doppler profile. As a result, the overall uncertainty of determining the absolute term value from the transition frequencies is generally limited by the Doppler broadening (about 0.03 cm^{-1}

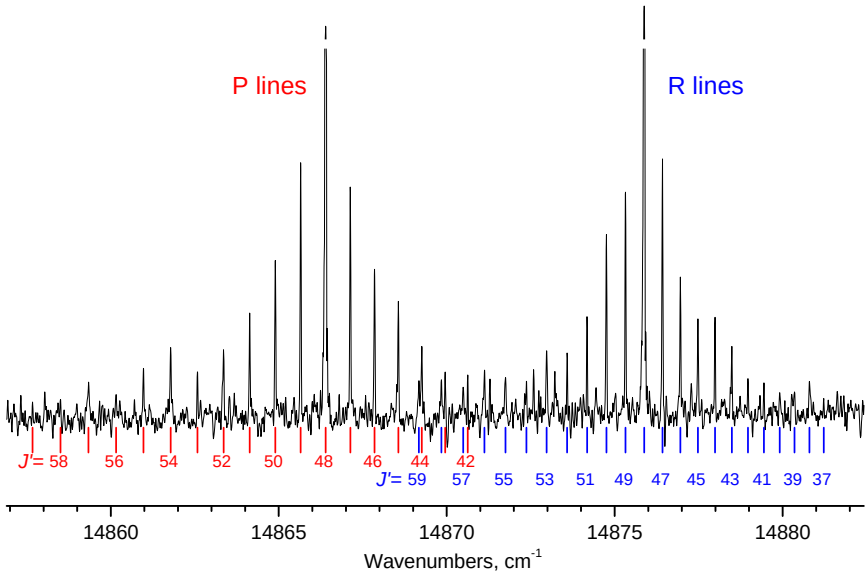

Figure 4.22. P and R collisionally-induced rotational satellites accompanying the LIF lines $C^1\Sigma^+(v' = 21, J' = 48) \rightarrow X^1\Sigma^+(v'' = 46, J'' = 47, 49)$. Excitation with Nd:YAG laser at frequency 18788.235 cm^{-1}.

FWHM for typical operation temperatures). Therefore we initially adopted the experimental uncertainty value of 0.01 cm^{-1} which was later justified by the data analysis.

From the FTS data a significant portion of the middle part of the C state PEC could be constructed. However, the bottom of the C state was still uncertain, since the main body of FTS measurements covered the region from $v' = 21$ to $v' = 46$, with a single measurement of $v' = 5$. In addition, it was important to investigate the possibility for collecting experimental data on the shelf region. Therefore, to enlarge and complete the data, a new experiment using the method of polarization labeling spectroscopy (PLS), which is well suited for the studies of excited states, was performed by our collaborators in Warsaw. In their experiments, the $C^1\Sigma^+ \leftarrow X^1\Sigma^+$ excitation spectrum of NaRb was studied by the V-type optical-optical double resonance polarization labeling spectroscopy (V-type PLS) with two independent pump and probe lasers [98]. Levels in the range $v' = 0 - 64$ were studied with accuracy of 0.05 cm^{-1}. The whole data field available from both Hannover and Warsaw measurements is shown in Figure 4.23 and consists of rovibrational levels with $v' = 0 - 64$ and $J' = 4 - 123$.

4.5.2 Construction of potential energy curve

Due to the special shape of the potential energy curve of the $C^1\Sigma^+$ state (see Fig. 4.1) we decided to construct a spline-pointwise potential with the IPA method [48], which is preferable for description of such irregular potentials. A use of regularization functional [50] allowed to overcome potential oscillating behavior in the regions poorly constrained by the experimental data. The initial guess of the PEC was the difference-based theoretical potential $U_C^{dif}(R)$ (4.6) defined in an equidistant grid of 33 points between 2.65 and 12.7 Å. With only few iterations of the IPA routine it was possible to fit all the LIF data for both NaRb isotopomers with a single PEC. This was considered as a first indication that the vibrational numbering suggested by the difference-based theoretical potential is correct. Since the FTS data set

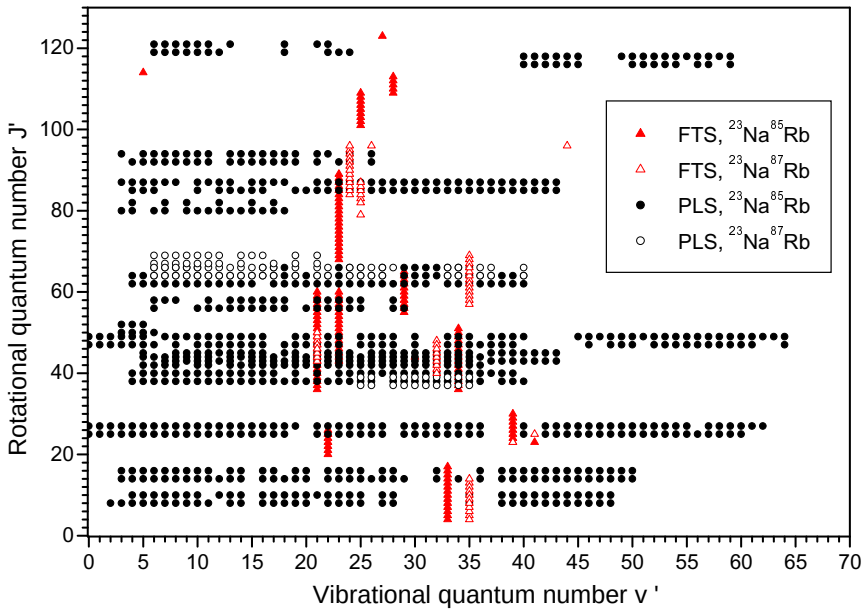

Figure 4.23. Distribution and sources of the experimental data used in the analysis of the $C^1\Sigma^+$ state of NaRb, accuracy of FTS data is 0.01 cm^{-1}, of PLS data – 0.05 cm^{-1}.

had quite a limited range of vibrational quantum numbers (from 21 to 46), we tested the vibrational assignment by constructing new potentials assuming a vibrational shift of $\Delta v = +1$ and $\Delta v = -1$. The attempts to fit the experimental results of both $Na^{85}Rb$ and $Na^{87}Rb$ with a single potential within the experimental uncertainty failed in these cases, as we expected. An additional test was made by comparing the calculated Franck-Condon factors (FCF) of the C–X transitions with the experimental intensity distributions of LIF. It was found that only the potential with the initially assumed vibrational assignment was able to give FCFs reproducing the observations.

The preliminary potential constructed with the FTS data allowed our colleagues from Warsaw to assign unambiguously the C–X transitions observed with the PLS method. They selected for labeling such ground state levels from which favorable FCF to the bottom of the $C^1\Sigma^+$ state and to the shelf region exist. For low v' deviations of the measured and the predicted line positions, calculated with the preliminary $C^1\Sigma^+$ state potential and the $X^1\Sigma^+$ state potential from Ref. [dis2] reached up to few cm^{-1} for $v' = 0-2$. The $C^1\Sigma^+$ state potential was gradually improved as new data with lower v' were included.

The final potential describes the experimental term energies of both $Na^{85}Rb$ (1001 levels) and $Na^{87}Rb$ (160 levels) isotopomers. The potential is defined at 49 points and is listed in Table 4.8. To larger distances a long-range expansion was used

$$U_{\rm LR}(R) = D - \frac{C_6}{R^6} - \frac{C_8}{R^8} - \frac{C_{10}}{R^{10}} \tag{4.7}$$

with C_6 and C_8 taken from Ref. [78]. Here D is the energy at the atomic asymptote. From theoretical predictions from Ref. [34], which, however, do not take into account the fine-structure splitting, we concluded that the $C^1\Sigma^+$ ($\Omega = 0$) state correlates to the $Na(3P_{1/2})+Rb(5S_{1/2})$ asymptote, because it is the lowest state correlating to Na(3P)+Rb(5S) limit. The energy of the $C^1\Sigma^+$ state asymptote $D = 21986.672 \pm 0.10$ cm^{-1} was calculated from the Na ($3p_{1/2}$) level energy [99] 16956.1703 cm^{-1} and the value of the ground state dissociation energy $D_e(X^1\Sigma^+) = 5030.502 \pm 0.10$ cm^{-1} [dis3]. The potential reproduces the PLS data with a standard deviation of 0.037 cm^{-1} and a dimensionless standard deviation of 0.79. The LIF data are reproduced with a standard deviation of 0.0083 cm^{-1} and a dimensionless

Table 4.8. List of potential energy grid points for the $C(3)^1\Sigma^+$ state. The full data set is represented with a standard deviation of 0.037 cm^{-1}.

R (Å)	$U(R)$ (cm^{-1})	R (Å)	$U(R)$ (cm^{-1})
2.6000	27339.156	5.7188	18627.109
2.7190	25761.642	5.8799	18856.61
2.8380	24277.932	6.0410	19091.257
2.9570	22970.966	6.2020	19326.105
3.0760	21903.509	6.3631	19557.231
3.1950	21024.166	6.5241	19780.173
3.3140	20270.612	6.6852	19990.929
3.4330	19631.429	6.8462	20183.582
3.5519	19105.284	7.0073	20350.56
3.6709	18678.278	7.2342	20519.818
3.7899	18338.747	7.4612	20608.871
3.9089	18075.017	7.6881	20666.835
4.0278	17876.402	7.9151	20728.386
4.1468	17733.865	8.1420	20807.328
4.2658	17639.271	8.5707	21017.979
4.3848	17585.876	8.9993	21330.484
4.5038	17568.111	9.4280	21740.865
4.6228	17581.281	9.8567	21910.956
4.7418	17621.977	10.2853	21950.712
4.8815	17699.64	10.7140	21968.14
5.0209	17805.681	11.1427	21976.325
5.1605	17936.028	11.5700	21980.261
5.3001	18086.687	12.0000	21982.33
5.4397	18254.406	12.4300	21983.475
5.5793	18435.788		
$R_{\text{out}} = 12.11009$ Å			
$D = 21986.672$ cm^{-1}		$C_8 = 2.1416 \cdot 10^9$ cm^{-1}Å^8	
$C_6 = -2.429 \cdot 10^6$ cm^{-1}Å^6		$C_{10} = 9.36942 \cdot 10^9$ cm^{-1}Å^{10}	
Potential minimum			
$R_{min} = 4.51$ Å		$U_{min} = 17568.07$ cm^{-1}	

standard deviation of 0.83. The combined dimensionless standard deviation for both data sets amounts to 0.80. Dissociation energy D_e of the $C^1\Sigma^+$ state obtained with the present potential is 4418.60 cm^{-1}. Its uncertainty is conservatively estimated as 0.3 cm^{-1} and takes into account the uncertainties of the ground state D_e and the U_{min} of the $C^1\Sigma^+$ state.

4.5.3 Dunham-type fit

For a conventional spectroscopic use a list of Dunham coefficients for the $C^1\Sigma^+$ state of $Na^{85}Rb$ is given in Table 4.9. They reproduce the experimental term energies in the range $0 \leq v' \leq 40$ and $8 \leq J' \leq 121$ with a dimensionless standard deviation of 0.92. Including the levels of the shelf region for an entire description of the data by the Dunham formalism would be unreasonable due to an enormously large number of parameters necessary.

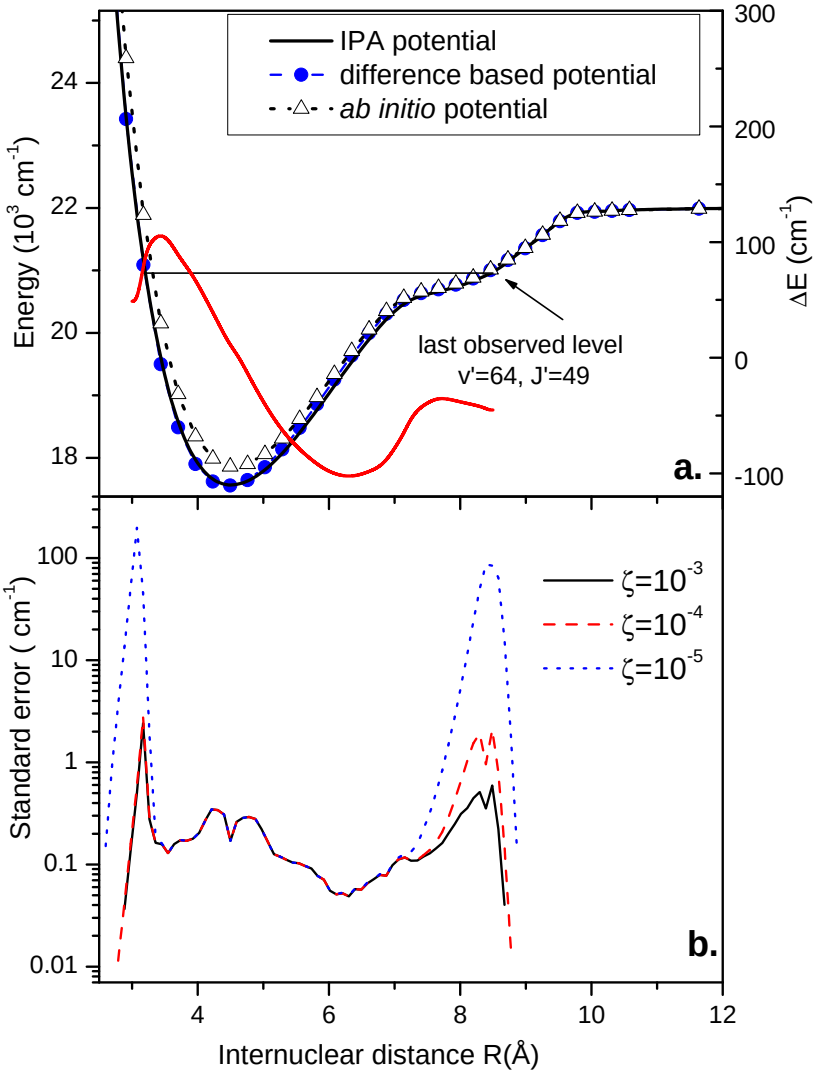

Figure 4.24. a. Comparison of the experimental IPA potential for the $C^1\Sigma^+$ state (solid line) and the corresponding *ab initio* potential by Korek *et al.* [34] (triangles and dotted line) and the difference-based potential (full circles). In red: $\Delta E = U_C^{expt} - U_C^{dif}$, referred to the right hand scale. b. Standard error of the fitted parameters for three different values of the singularity parameter ζ.

Table 4.9. Dunham parameters for the $C(3)^1\Sigma^+$ state of $Na^{85}Rb$ for the limited range $0 \leq v' \leq 40$ and $8 \leq J' \leq 121$. $T_e + Y_{0,0}$ is referred to the minimum of the ground state potential. The limited data set is represented with a standard deviation of 0.02 cm^{-1}.

parameter	value (cm^{-1})	uncertainty (cm^{-1})
$(T_e + Y_{0,0})_{\mathrm{Dun}}$	17568.128	0.012
$Y_{1,0}$	63.6019	0.44×10^{-2}
$Y_{2,0}$	-0.04156	0.57×10^{-3}
$Y_{3,0}$	-0.22266×10^{-2}	0.33×10^{-4}
$Y_{4,0}$	0.30505×10^{-4}	0.86×10^{-6}
$Y_{5,0}$	-0.3383×10^{-6}	0.82×10^{-8}
$Y_{0,1}$	0.4579804×10^{-1}	0.50×10^{-5}
$Y_{1,1}$	-0.13316×10^{-3}	0.11×10^{-5}
$Y_{2,1}$	-0.1195×10^{-5}	0.89×10^{-7}
$Y_{3,1}$	0.4089×10^{-7}	0.28×10^{-8}
$Y_{4,1}$	-0.8097×10^{-9}	0.32×10^{-10}
$Y_{0,2}$	-0.91916×10^{-7}	0.28×10^{-9}
$Y_{1,2}$	0.9417×10^{-9}	0.29×10^{-10}
$Y_{2,2}$	-0.2788×10^{-10}	0.70×10^{-12}

4.5.4 Discussion

The present measurements characterize 77% of the $C^1\Sigma^+$ state potential well depth—from the bottom up to about 21000 cm^{-1} (see Fig. 4.24), which is still about 1000 cm^{-1} below the Na(3P)+Rb(5S) asymptote. The last observed rovibronic level is located well in the shelf region. In Fig. 4.24a the experimental potential is compared to the *ab initio* potential from Ref. [34] (triangles in Figure 4.24a) and the difference-based potential (full circles).

As one can see, the difference-based potential is much closer to the experimental one than the *ab initio* potential, so that the statement from Ref. [4] is confirmed here. The red line in Fig. 4.24a displays the difference $\Delta E = U_{\mathrm{C}}^{expt} - U_{\mathrm{C}}^{dif}$, referring to the magnified right hand side scale, for better visibility, and shows variations of about 100 cm^{-1}. This finding suggests that for more reliable predictions of excited state potentials it is better to use the differences of *ab initio* potential curves with respect to the experimental potential, if it is known with high precision.

Some caution has to be applied to the uncertainties of the Dunham parameters given in Table 4.9 and especially for that of T_e. During the fitting procedure for the potential energy curve we observed that the potential minimum is determined with relatively large ambiguity. $U_{\min}$ varied from fit to fit, depending on the number of fitted parameters to within ± 0.2 cm^{-1}. In Fig. 4.24b the standard error of the fitted parameters is shown for three different values of the singularity parameter ζ used within the Singular Value Decomposition technique (see Section 2.10.1) in order to avoid changes in the potential shape not caused by the experimental data. Regions where the standard error does not change with ζ are fixed mainly by the experimental data. Outside these regions the variation of the potential is limited by ζ and therefore its shape is less well described within the present data set. Note the increase of the uncertainty around the potential minimum, which reaches 0.3 cm^{-1}. On the other hand the value of T_e determined from the Dunham coefficients (with $Y_{0,0} = 0.022$ cm^{-1} for the C state) was not so sensitive to the number of Dunham coefficients and the range of the experimental data being always around the value reported in Table 4.9.

In principle, $T_e + Y_{0,0}$ should coincide with $U_{\min}$. However, a small difference remains, but well within the expected uncertainty of $U_{\min}$. Presently, we attribute the large difference in the estimation of the uncertainty to the kind of flexibility of both representations: the small uncertainty in T_e in the fit of Dunham coefficients originates from the rigidness of this model, whereas the larger uncertainty in $U_{\min}$

is due to the small amount of experimental data near the potential minimum and the flexibility of the pointwise representation of the potential. We would like to stress here the intrinsic uncertainty in the determination of the potential minimum, which is only indirectly defined by the experimental data and is model dependent, especially when extrapolated from a scarce data set.

A particular shape of the $C^1\Sigma^+$ state with the "shelf" implied its possible suitability as an intermediate state for photoassociation (PA) of cold NaRb ground state molecules. However, analysis showed that the largest PA rates for the $X^1\Sigma^+ - C^1\Sigma^+$ transition are smaller by about two orders of magnitude when compared to the results for the NaRb $X^1\Sigma^+ - A^1\Sigma^+$ transition [27]. This gives indeed preference to the choice of the $A^1\Sigma^+$ state for PA experiments.

4.5.5 Results and conclusions

1. NaRb $C^1\Sigma^+ \rightarrow X^1\Sigma^+$ high-resolution LIF spectra were obtained for the first time using the FTS method. The data field of the $C^1\Sigma^+$ state has been enlarged significantly by the term values obtained from the analysis of the rotational relaxation lines. Experimental term value uncertainty is 0.01 cm^{-1}.

2. From the analysis of the FTS spectra 138 term values of $Na^{85}Rb$ and 66 term values of $Na^{87}Rb$ $C^1\Sigma^+$ state in the range $v' = 5; 21 - 46$, $J' = 4 - 123$ were obtained.

3. FTS term energies together with the data obtained by our collaborators in Warsaw by polarization labeling spectroscopy technique were incorporated into a direct fit of a single spline-pointwise potential energy curve to the level energies. The PEC describes the experimental term energies of both $Na^{85}Rb$ (1001 level) and $Na^{87}Rb$ (160 levels) isotopomers with $\sigma = 0.037$ cm^{-1} and $\bar{\sigma} = 0.80$. The FTS data are reproduced with $\sigma = 0.0083$ cm^{-1} and $\bar{\sigma} = 0.83$.

4. Dissociation energy of the $C^1\Sigma^+$ state obtained with the present potential is 4418.6 ± 0.3 cm^{-1}.

5. Term energies were also fitted to Dunham expansion below the "shelf region". The obtained set of constants reproduces the experimental term energies in the range $0 \leq v' \leq 40$ and $8 \leq J' \leq 121$ with $\bar{\sigma} = 0.92$.

4.6 NaRb $D^1\Pi$ state [dis5]

During the study of the ground state of NaRb, done in Hannover by means of Fourier-transform spectroscopy of laser-induced fluorescence [dis2] it turned out that a lot of information about the excited $C^1\Sigma^+$ and $D^1\Pi$ states was available from the recorded spectra. A significant amount of data became available from analysis of rotational relaxation lines. Below, the $D^1\Pi$ state analysis based on these experimental data is presented. Detailed analysis of the observed Λ-doubling for various rovibrational levels is also given.

4.6.1 Observations and term value analysis

The experimental details have been described in Section 3.2. The Ar^+ ion laser lines 514.5 nm, 501.7 nm, 496.5 nm, 488.0 nm, and 476.5 nm efficiently induced the D–X fluorescence in NaRb. Overall 130 progressions were assigned. The range of vibrational quantum numbers v' observed in the $D^1\Pi$ state with the Ar^+ laser lines is $v' = 0 - 39$. A tunable single mode, frequency doubled Nd:YAG laser was also used to excite $D^1\Pi - X^1\Sigma^+$ transitions in NaRb. The laser frequency was varied between 18787.25 cm^{-1} and 18788.44 cm^{-1} giving rise to 38 D–X progressions. The range of vibrational levels excited in the $D^1\Pi$ state by the Nd:YAG laser is $v' = 0 - 16$.

Due to the presence of the argon buffer gas and very high signal-to-noise ratio several strong fluorescence lines were accompanied by large number of collisionally-induced satellites with ΔJ up to ± 30. To enrich the rotational relaxation spectra some spectra were recorded at 10 mbar buffer gas pressure. In a few spectra collisionally-induced transitions from the neighboring vibrational levels were also observed. The analysis of rotational satellites has enlarged the data set of the $D^1\Pi$ state significantly.

Similarly to the case of the $C^1\Sigma^+$ state, the rotational and isotopomer assignment was established using the $X^1\Sigma^+$ state PEC [dis2]. Then the energies of the excited levels were obtained by adding the experimental transition frequencies to the respective ground state term values calculated from the PEC. The vibrational numbering for $v' \leq 12$ was obtained with the help of the $D^1\Pi$ state Dunham constants and corresponding RKR potential from Ref. [4]. For higher levels a graphical analysis of the term energies as a function of $J'(J'+1) - 1$ helped us to unambiguously establish the continuation of the vibrational numbering. This plot, giving also an overview of the data field, is shown in Fig. 4.25.

Overall, from the analysis of the Fourier spectra we obtained 1182 term values of $Na^{85}Rb$ and 314 term values of $Na^{87}Rb$ for the $D^1\Pi$ state. The range of vibrational and rotational quantum numbers is $v' = 0 - 39$ and $J' = 1 - 200$ respectively. As in the case of the $C^1\Sigma^+$ state (see Section 4.5), the attributed experimental uncertainty value is 0.01 cm^{-1}.

4.6.2 Λ-doubling and q factors

The $D^1\Pi - X^1\Sigma^+$ rotational relaxation spectra appeared due to collisional population of neighboring rotational levels in the $D^1\Pi$ state preferably with the same symmetry (e or f) and subsequent D–X emission according to selection rules for electric dipole transitions. Q lines were typically accompanied by Q satellites, whereas the doublet lines were accompanied by P, R doublet satellites. However, in a number of cases the strongest parent lines had additional satellites coming from the neighboring rotational levels of the opposite symmetry. Thus, a strong Q line had not only a Q satellite branch, but also the P and R satellites (see Fig. 4.26). This opened the opportunity to establish directly the Λ-splitting of rotational levels of the $D^1\Pi$ state. From the analysis of the Q lines we obtained f level energies, whereas from the analysis of the P and R lines we obtained the energies of e levels. Then the evaluation of q factors is straightforward:

$$E_e - E_f \equiv \Delta_{e/f} = qJ'(J'+1). \tag{4.8}$$

This allowed us to obtain q factor values and their sign for 20 vibrational levels in the interval $v' = 0 - 35$ in a wide range of rotational quantum numbers ($J' = 20 - 122$).

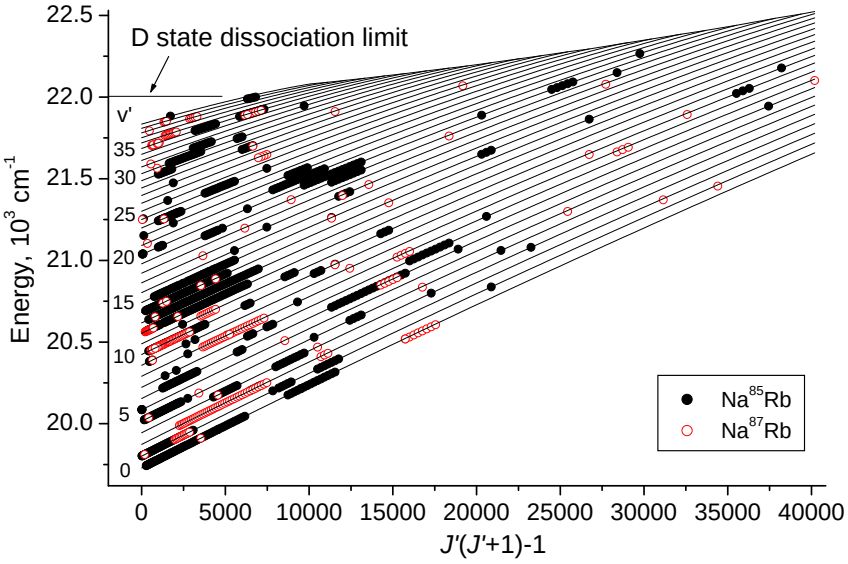

Figure 4.25. Plot of the $D^1\Pi$ state experimental term energies against $J'(J'+1)-1$. Solid lines show the calculated term energies, obtained with the present potential from Table 4.11.

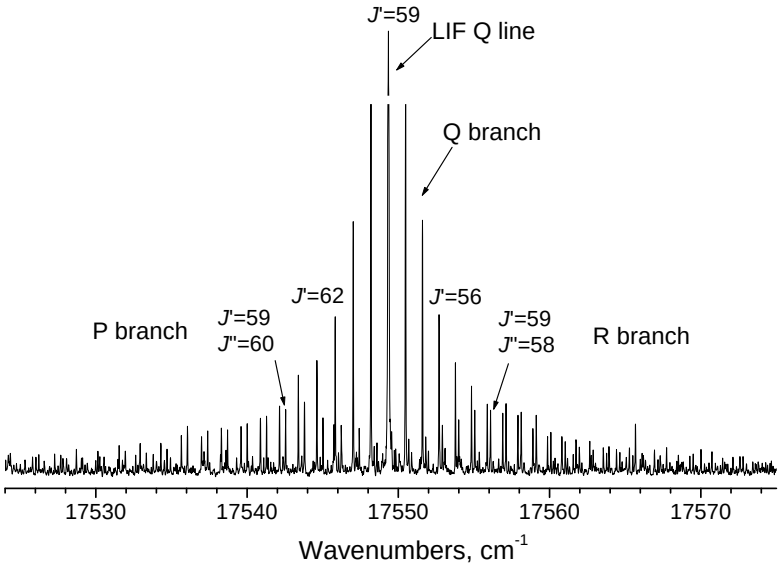

Figure 4.26. P, Q, R collisionally-induced rotational satellites accompanying the parent Q transition ($D^1\Pi(13,\,59) \rightarrow X^1\Sigma^+(30,\,59)$) excited with the Ar^+ laser line 488.0 nm.

For most of the vibrational levels the measured q factors are around $0.9 \cdot 10^{-5}$ cm^{-1}. As q factors are calculated from the Λ-splitting energy $\Delta_{e/f}$, q factor uncertainty is determined by the uncertainty of about 0.004 cm^{-1} of the Λ-splitting energy . The latter arises mainly from two sources: the uncertainty of the experimental D–X transition energy difference (0.003 cm^{-1}) and the uncertainty of the calculated energy difference between the ground state levels (0.003 cm^{-1}, as stated in [dis2]). Note, that the q factor uncertainty is inversely proportional to $J'(J'+1)$.

In few cases an anomalous behavior of the Λ-splittings was observed, clearly indicating a local perturbation in the D$^1\Pi$ state. Fig. 4.27 presents an example of such a perturbation for the vibrational level $v' = 10$ with the perturbation center around $J' = 31$ for Na^{85}Rb.

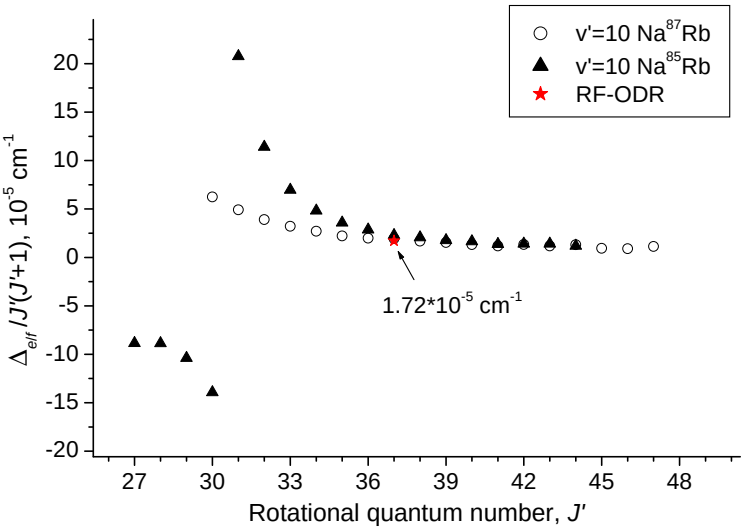

Figure 4.27. The dependence of $\Delta_{e/f}/J'(J'+1)$ on J' for $v' = 10$ level in Na^{85}Rb (triangles) and Na^{87}Rb (open circles). The arrow marks the q factor determined from the RF-ODR experiment, see Table 4.10.

Analysis of q factors outside the local perturbation regions in $v' = 0 - 30$ range did not reveal a vibrational or isotopomer dependence within our accuracy, whereas a slight decrease of q factors with J' was observed. Thus it was possible to describe the whole set of q factors by linear J'-dependence

$$q = q_0 + q_1 J'. \tag{4.9}$$

Fig. 4.28 presents approximately eighty q factors plotted as a function of J'. These q values are obtained from about thousand experimental q factors after performing a weighted average for a given J'. The large scatter of q values for low J' comes from the very small Λ-splittings, which are comparable with the experimental uncertainty. The resulting fit parameters in (4.9) are $q_0 = 1.079(14) \cdot 10^{-5}$ cm^{-1} and $q_1 = -2.30(15) \cdot 10^{-8}$ cm^{-1}.

The q factors measured in this work are consistent with the RF-ODR measurements [4], which are of higher accuracy, but cover a very limited set of measured levels with $J' \leq 52$. The values q_{RF-ODR} presented in Table 4.10 and Fig. 4.28 have been recalculated using experimental Λ-splitting values from Ref. [65] and the recently established correct J' assignment from [dis2]. A comparison between the experimental q factors and the *ab initio* calculations from Ref. [4] is included in Table 4.10 and Fig. 4.28. The *ab initio* q factors were obtained from the electronic structure calculations performed by means of the many-body multi-partitioning perturbation theory (MPPT), using the singlet-singlet approximation, i.e. the Λ-splitting is determined by electronic-rotational perturbations caused by distant singlet $^1\Sigma^+$ states. Analysis of L-uncoupling matrix elements between the D$^1\Pi$ state and the X, A, C and E$^1\Sigma^+$

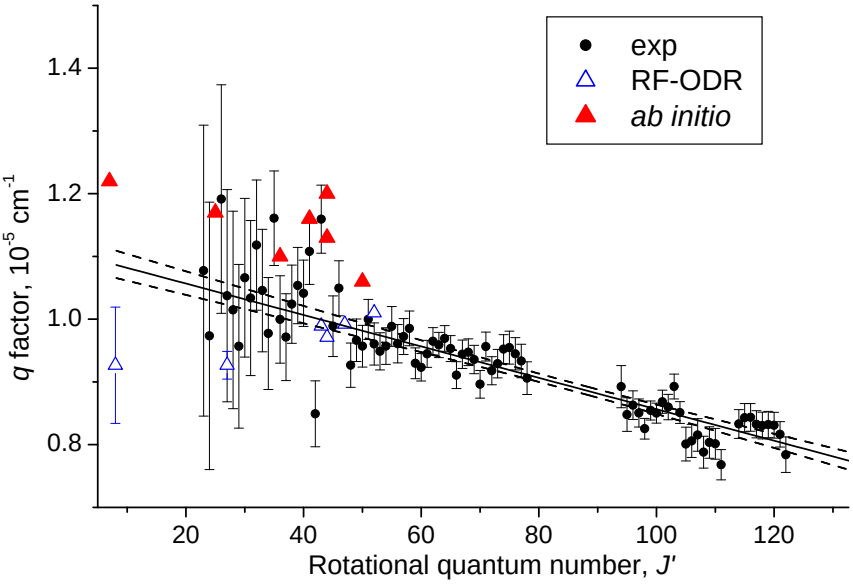

Figure 4.28. $D^1\Pi$ state unperturbed q factors (circles), averaged for different vibrational levels and isotopomers. The solid line corresponds to the fitted linear dependence $\bar{q} = [1.079 - 0.00230 \cdot J']10^{-5}$ cm^{-1} and the dashed lines denote the 95% confidential region. Full triangles are *ab initio* q factors from Ref. [4]. Open triangles denote the RF-ODR q factor values (see Table 4.10).

Table 4.10. The $D^1\Pi$ state q_{RF-ODR} factors (in 10^{-5} cm^{-1}) obtained from the RF-ODR experiments in Ref. [65] and recalculated for correct J' values; J' in parentheses corresponds to the previous assignment from Ref. [65]. The given uncertainty is one standard deviation. $q_{ab\ initio}$ are the calculated values from Ref. [4].

Isotopomer	v'	$J'(J'[65])$	q_{RF-ODR}	$q_{ab\ initio}$
$Na^{85}Rb$	0	44(44)	0.971 ± 0.003	+1.20
$Na^{85}Rb$	1	8(7)	0.93 ± 0.09	+1.22
$Na^{85}Rb$	4	27(25)	0.93 ± 0.02	+1.17
$Na^{85}Rb$	4	43(41)	0.989 ± 0.002	+1.16
$Na^{85}Rb^*$	6	47(44)	0.992 ± 0.003	+1.13
$Na^{87}Rb$	10	37(36)**	1.723 ± 0.002	+1.10
$Na^{85}Rb$	12	52(50)	1.0101 ± 0.0012	+1.06

* – isotopomer changed compared to Ref. [65]
** – perturbed level

states showed that the Λ-splitting in the $D^1\Pi$ state is mainly determined by the interaction with the $C^1\Sigma^+$ state. The calculated q factors are in good agreement with the experimental data, but slightly larger (see Fig. 4.28), probably because of neglecting the influence of the $^1\Sigma^+$ states higher than the $E^1\Sigma^+$ state in the calculations.

Note that the only experimental q factor in Table 4.10 showing strong deviation from calculations is the one for the level $v' = 10$, $J' = 37$. Present measurements (see Fig. 4.27) support the statement already proposed in Ref. [4] that this discrepancy is attributed to a local perturbation.

4.6.3 Construction of potential energy curve

The $D^1\Pi$ state for both isotopomers of NaRb is described in the adiabatic approximation with a single potential energy curve. The potential was defined as proposed in Ref. [48] as a set of points $\{R_i, U(R_i)\}$ connected by cubic spline functions. Fitting procedure is similar to one used for the NaRb C state. In order to avoid unphysical oscillations in the regions not sufficiently determined by the experimental data, we applied the regularization procedure [50].

As an initial guess for the potential curve, we took the RKR potential constructed using molecular constants from Ref. [4]. Since the shift of the f levels under the influence of far lying higher Σ^- states is expected to be very small, the potential fit was based on the f levels considered as "unshifted". The e levels were also included in the fit after subtracting from their experimental term energies the value of the Λ-splitting $q(J')J'(J'+1)$ determined in the previous section. Levels showing deviations more than 0.03 cm^{-1} (about 7% of the whole data set) were not included in the final fitting procedure. These levels are considered either as perturbed (see Section 4.6.5) or as Doppler-shifted levels.

Taking into account the $q(J')$ dependence of Eq. 4.9, the final spline-pointwise potential fits all unperturbed energy levels of both isotopomers with a standard deviation of 0.008 cm^{-1} and a dimensionless standard deviation of 0.78. It consists of 35 points and is given in Table 4.11. In order to interpolate the potential, a natural cubic spline [51] through all 35 grid points should be used. Note, that if the J' dependence of the q factors is neglected and a single averaged q factor ($0.87 \cdot 10^{-5}$ cm^{-1}) is used, we get a standard deviation of 0.009 cm^{-1} and a dimensionless standard deviation of 0.88.

Initially, the PEC was constructed in a pointwise form up to 10 Å. In order to ensure the proper asymptotic behavior of the potential we connected the PEC with a long-range (LR) branch, for which we adopted the usual dispersion form

$$U(R) = D - \frac{C_6}{R^6} - \frac{C_8}{R^8} - \frac{C_{10}}{R^{10}} \tag{4.10}$$

with coefficients C_6 and C_8 taken from Ref. [78]. The dissociation asymptote D of the $D^1\Pi$ state correlating to the $Na(3P_{3/2})$ + $Rb(5S_{1/2})$ atomic limit was calculated from the $Na(3P_{3/2})$ level energy [99] (neglecting hyperfine structure, referred to the hyperfine center of gravity) and the $X^1\Sigma^+$ state dissociation energy 5030.50(10) cm^{-1} [dis3]. The connecting point R_{out} and the C_{10} parameter were varied in order to ensure a smooth connection with the pointwise potential. Thus, the C_{10} parameter presented here should be considered just as an effective coefficient.

The $D^1\Pi$ state dissociation energy obtained in the present experiment is 2311.30(14) cm^{-1}. The accuracy of the derived $D^1\Pi$ state dissociation energy is associated with the accuracy of the $X^1\Sigma^+$ state dissociation energy [dis3] and the estimated uncertainty of 0.1 cm^{-1} of the $D^1\Pi$ state potential minimum value. The dissociation energy with respect to the first bound level ($v' = 0$, $J' = 1f$) is 2274.79(10) cm^{-1}.

In Figure 4.30a the experimental IPA potential is compared with the *ab initio* potential from Ref. [34] (full circles). Also the difference-based potential $U_D^{dif}(R)$ (4.6) suggested in Ref. [4, 75] as an improved estimate from *ab initio* results is given in Figure 4.30a (open circles). It is produced from the difference of the *ab initio* $D^1\Pi$ and $X^1\Sigma^+$ state potentials given in Ref. [34], which is then added to the experimental ground state potential U_X^{expt} given in Table 4.6. As can be seen, the difference-based potential is significantly closer to the IPA potential than the *ab initio* one. Similar conclusions were obtained in studies of

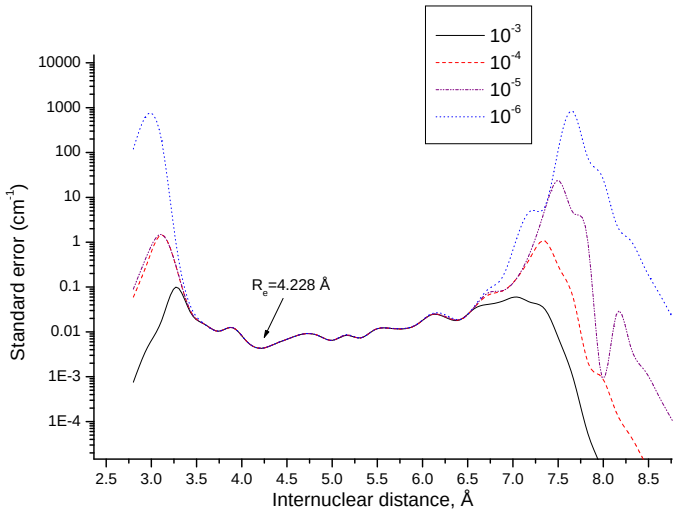

Figure 4.29. Standard error of the fitted parameters for different values of the singularity parameter ζ.

Table 4.11. List of the grid points of the potential energy curve for the NaRb $D^1\Pi$ state. Energies are given with respect to the minimum of the ground state (Table 4.6).

R (Å)	$U(R)$ (cm^{-1})	R (Å)	$U(R)$ (cm^{-1})
2.80000	26088.574	5.28571	20599.728
2.97500	23892.559	5.42857	20762.635
3.15000	22416.175	5.57143	20916.356
3.32500	21452.447	5.71429	21058.223
3.50000	20753.769	5.85714	21186.491
3.60000	20448.239	6.00000	21300.660
3.70000	20203.231	6.29429	21491.459
3.80000	20013.336	6.58857	21630.673
3.90000	19872.445	6.88286	21729.052
4.00000	19775.498	7.17714	21798.073
4.14286	19703.369	7.64762	21870.204
4.28571	19697.224	8.11810	21915.936
4.42857	19744.947	8.58857	21945.594
4.57143	19835.458	9.05905	21964.683
4.71429	19958.393	9.52952	21977.465
4.85714	20104.327	9.86476	21984.053
5.00000	20264.751	10.20000	21989.488
5.14286	20432.036		
$R_{\text{out}} = 9.94559$ Å			
$D = 22003.868$ cm^{-1}		$C_8 = 3.4178 \cdot 10^9$ cm^{-1}Å^8	
$C_6 = -1.5046 \cdot 10^7$ cm^{-1}Å^6		$C_{10} = -1.6265 \cdot 10^{10}$ cm^{-1}Å^{10}	
Potential minimum			
$R_{min} = 4.2279$ Å		$T_{min} = 19692.564$ cm^{-1}	

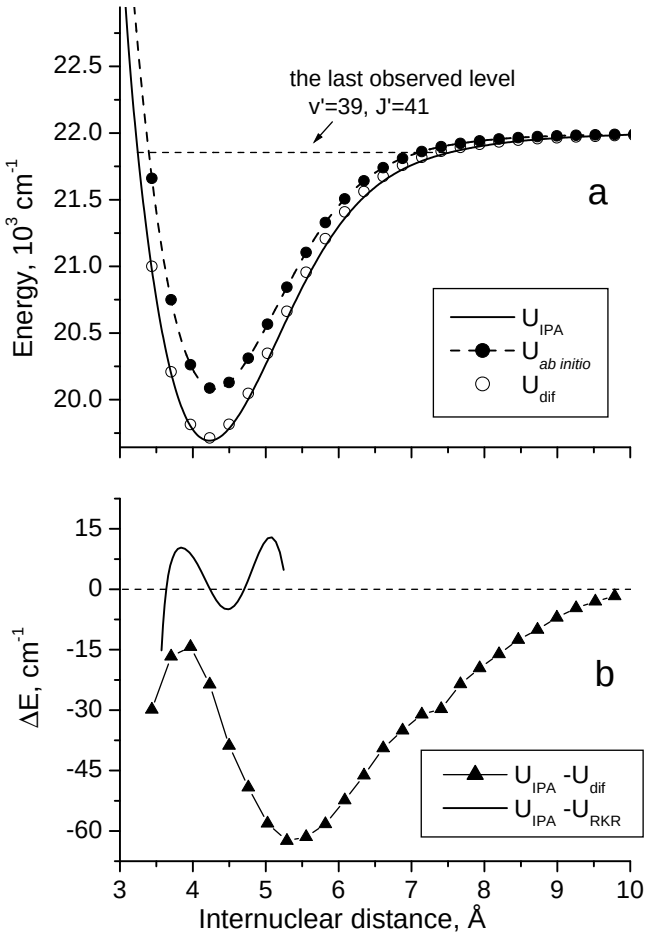

Figure 4.30. (a) Comparison of the new determination of the $D^1\Pi$ state IPA potential (solid line) with the corresponding *ab initio* potential by Korek *et al.* [34] (full circles) and the difference based potential (open circles), moved to the correct atomic limit (b) Difference of the IPA potential $U_{\rm IPA}$ with respect to the difference based potential (triangles) and to the RKR potential $U_{\rm RKR}$ from Ref. [4] (solid line).

the NaRb $A^1\Sigma^+ - b^3\Pi$ complex in Ref. [75] and by present studies of the NaRb $C^1\Sigma^+$ state [dis4]. The difference between the IPA potential and the RKR potential from Ref. [4] is shown in Fig. 4.30b.

4.6.4 Dunham expansion

For the convenience of simple spectroscopic estimations we have also fitted a Dunham expansion with the conventional Y_{lk} coefficients to the unperturbed energy levels, where l and k are powers of $(v'+1/2)$ and $[J'(J'+1)-1]$, respectively. The levels are described with a standard deviation of 0.009 cm^{-1} and a dimensionless standard deviation of 0.87 for both isotopomers. The Dunham parameters, rounded as described in Ref. [61], are listed in Table 4.12. It is worth mentioning that the T_e = 19692.06 cm^{-1}, R_e = 4.2155 Å, ω_e = 73.26 cm^{-1} and B_e = 0.05244 cm^{-1} values from Ref. [4] for $Na^{85}Rb$ are rather close to the ones in the present work.

Table 4.12. Dunham parameters (in cm^{-1}) of the $Na^{85}Rb$ $D^1\Pi$ state for $v' \leq 39$, $J' \leq 200$, valid also for $Na^{87}Rb$ employing the conventional mass relations.

T_e	19692.5496		$Y_{0,2}$	-0.105723	$\times 10^{-6}$
$Y_{0,0}$	-0.019		$Y_{1,2}$	-0.12890	$\times 10^{-8}$
$Y_{1,0}$	73.10306		$Y_{2,2}$	0.202	$\times 10^{-10}$
$Y_{2,0}$	-0.281142		$Y_{3,2}$	-0.473	$\times 10^{-11}$
$Y_{3,0}$	-0.53893	$\times 10^{-2}$	$Y_{5,2}$	0.423	$\times 10^{-14}$
$Y_{4,0}$	0.11707	$\times 10^{-3}$	$Y_{6,2}$	-0.104	$\times 10^{-15}$
$Y_{6,0}$	-0.40941	$\times 10^{-6}$	$Y_{0,3}$	0.2124	$\times 10^{-12}$
$Y_{7,0}$	0.18988	$\times 10^{-7}$	$Y_{3,3}$	-0.1245	$\times 10^{-15}$
$Y_{8,0}$	-0.3688	$\times 10^{-9}$	$Y_{4,3}$	0.1342	$\times 10^{-16}$
$Y_{9,0}$	0.27	$\times 10^{-11}$	$Y_{5,3}$	-0.345	$\times 10^{-18}$
$Y_{0,1}$	0.5212303	$\times 10^{-1}$	$Y_{0,4}$	-0.118	$\times 10^{-17}$
$Y_{1,1}$	-0.221455	$\times 10^{-3}$	$Y_{1,4}$	-0.141	$\times 10^{-18}$
$Y_{2,1}$	-0.62437	$\times 10^{-5}$	$Y_{4,4}$	-0.95	$\times 10^{-22}$
$Y_{3,1}$	0.33948	$\times 10^{-6}$			
$Y_{4,1}$	-0.30585	$\times 10^{-7}$			
$Y_{5,1}$	0.1196	$\times 10^{-8}$			
$Y_{6,1}$	-0.252	$\times 10^{-10}$			
$Y_{7,1}$	0.20	$\times 10^{-12}$			

4.6.5 Perturbations

As stated above, the obtained PEC fits most of the observed levels with a standard deviation of 0.008 cm^{-1}. However, we have measured a number of v', J' levels whose experimental term values deviate from the calculated ones by more than 0.03 cm^{-1} indicating a possible presence of local perturbations. In cases where a long series of rotational satellites was observed we could follow how both e and f components behave in the particular local perturbation region. In Fig. 4.31 differences between the observed term values (E_{expt}) and energies calculated with the PEC (E_{calc}) are shown for vibrational levels $v' = 23$ and 10. It is obvious that both e and f components are perturbed in the presented J' ranges. This means that perturbations are caused by nearby triplet states, apparently the $d^3\Pi$ or the $e^3\Sigma^+$, see Fig. 4.1. For higher vibrational levels the additional influence of the $E^1\Sigma^+$ state cannot be excluded.

We have to confess that we were not able to study perturbations systematically due to the accidental character of optical excitations of different v', J' levels by fixed-frequency laser lines. Nevertheless, we have found more than 10 perturbation regions in the $v' = 0 - 39$ interval. The largest observed deviation

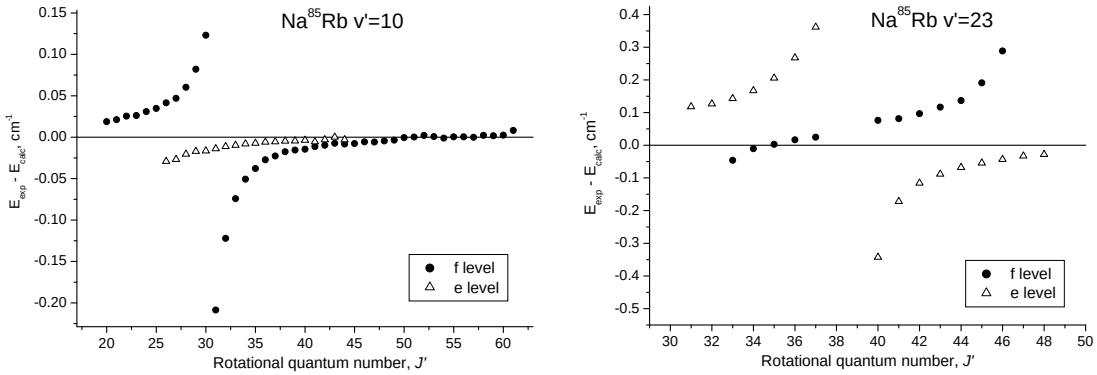

Figure 4.31. The difference between observed and unperturbed (calculated from the IPA potential) term energies for vibrational levels $v' = 10$ and $v' = 23$ of the $D^1\Pi$ state.

of a term value reached almost 2 cm^{-1} for $v' = 38$, $J'_e = 79$. A list of perturbation regions is given in part 5 of the supplementary online material of [dis5].

4.6.6 Results and conclusions

1. NaRb $D^1\Pi \rightarrow X^1\Sigma^+$ high-resolution LIF spectra were obtained for the first time using the FTS method. The data field of the $D^1\Pi$ state has been enlarged significantly by the term values obtained from the analysis of the rotational relaxation lines.

2. From the analysis of the FTS spectra 1182 term values of $Na^{85}Rb$ and 314 term values of $Na^{87}Rb$ for the $D^1\Pi$ state were obtained. Experimental term value uncertainty is 0.01 cm^{-1}. The range of vibrational and rotational quantum numbers is $v' = 0 - 39$ and $J' = 1 - 200$. The present FTS measurements characterize 93.5% of the $D^1\Pi$ state potential well.

3. A large set of q factors in the $D^1\Pi$ state was obtained allowing to derive their dependence on the rotational quantum number J'. No vibrational dependence of q factors was observed within the accuracy of present measurements. In several cases an anomalous behavior of a q factor was observed, clearly indicating a local perturbation in the $D^1\Pi$ state.

4. Experimental term energies were incorporated into a direct fit of a single spline-pointwise potential energy curve to the level energies. The PEC describes the experimental term energies of both NaRb isotopomers with $\sigma = 0.008$ cm^{-1} and $\bar{\sigma} = 0.78$.

5. Dissociation energy of the $D^1\Pi$ state obtained with the present potential is 2311.30 ± 0.14 cm^{-1}.

6. Term energies were also fitted to the Dunham expansion. The obtained set of constants reproduces the experimental term energies with $\sigma = 0.009$ cm^{-1} and a dimensionless standard deviation of $\bar{\sigma} = 0.87$ for both isotopomers.

7. Analysis of perturbation regions revealed that both e and f components are perturbed, thus testifying to the triplet character of perturbing state. Apparently, either the $d^3\Pi$ or the $e^3\Sigma^+$ state perturbs the $D^1\Pi$ state.

Chapter 5

NaCs molecule

5.1 Background

The first spectroscopic observation of the NaCs molecule by Walter and Barrat [66] dates back to 1928. Later, Weizel and Kulp [100] succeeded in a partial analysis of the rotationally unresolved band spectra of Walter and Barrat and were able to deduce vibrational term differences of the lowest vibrational levels in the $X^1\Sigma^+$ state and in an excited state at $T_e \approx 18230$ cm^{-1} which they labeled as the D state but which they could not further characterize.

Accurate experimental spectroscopic information on NaCs is still limited, including that on the ground state. A combination of polarization spectroscopy and optical double-resonance methods in Ref. [101] has provided precise data for the lowest part of the $X^1\Sigma^+$ ground state limited to vibrational quantum numbers $v'' \leq 21$, and measurement of laser-induced fluorescence by means of a grating spectrograph yielding data for higher levels up to $v'' = 64$. Combined analysis of these data gave Dunham coefficients, RKR potential and an estimate of the dissociation energy $D_e = 4950 \pm 100$ cm^{-1} of the $X^1\Sigma^+$ ground state. In the same paper first analysis of the excited $D(2)^1\Pi$ state is presented. The Dunham molecular constants are given for $v' = 0 - 2$, while inclusion of levels $v' = 3 - 7$ into the fit showed numerous deviations thus testifying presence of perturbations in the $D^1\Pi$ state. The authors of Ref. [101] also pointed out that the Ar^+ 515.4 nm line excited low vibrational levels of the $^1\Pi$ state correlating to the Na(3P)+Cs(6S) asymptote. This state was labelled as the $G^1\Pi$ state.

Kopystynska *et al.* [102] studied the laser-induced fluorescence spectra in a cell with different mixtures of alkalis. Exciting with Ar^+ laser at 514.5 nm they found several progressions one of which around 660 nm they identified as a progression of NaCs to the $a^3\Sigma^+$ state. Because of fairly low resolution they used several indirect arguments for this identification. However, the present studies showed that these were transitions to the $X^1\Sigma^+$ state (see below).

An extensive theoretical study of the electronic structure of NaCs has been performed by Korek *et al.* [35]. Potential energy curves for 32 electronic states were calculated far out to the atomic asymptotes. Low electronic states from Ref. [35] are shown in Fig. 5.1. It can be seen that the calculated sequence of singlet terms makes the alphabetic notation of the excited electronic states ambiguous. Thus, only numeric electronic state classification is used hereafter.

The pair of Na and Cs atoms is presently one of the interesting objects in relation to experiments with mixed alkali-metal species at ultracold temperatures. Results of experimental research performed on inelastic cold collisions in Na-Cs trap were reported in Refs. [103, 77]. Experimental observation of ultracold $NaCs^+$ molecular formation in a novel two-species magneto-optical trap was described in Ref. [104]. Recently, also first successful formation of translationally cold NaCs molecules starting from a laser-cooled atomic vapor of Na and Cs atoms was realized [23]. In these experiments the colliding atoms were transferred into bound molecular states in a two-step photoactivated process in which the atoms were first photoassociated by trap photons into an excited state molecular complex and then allowed to

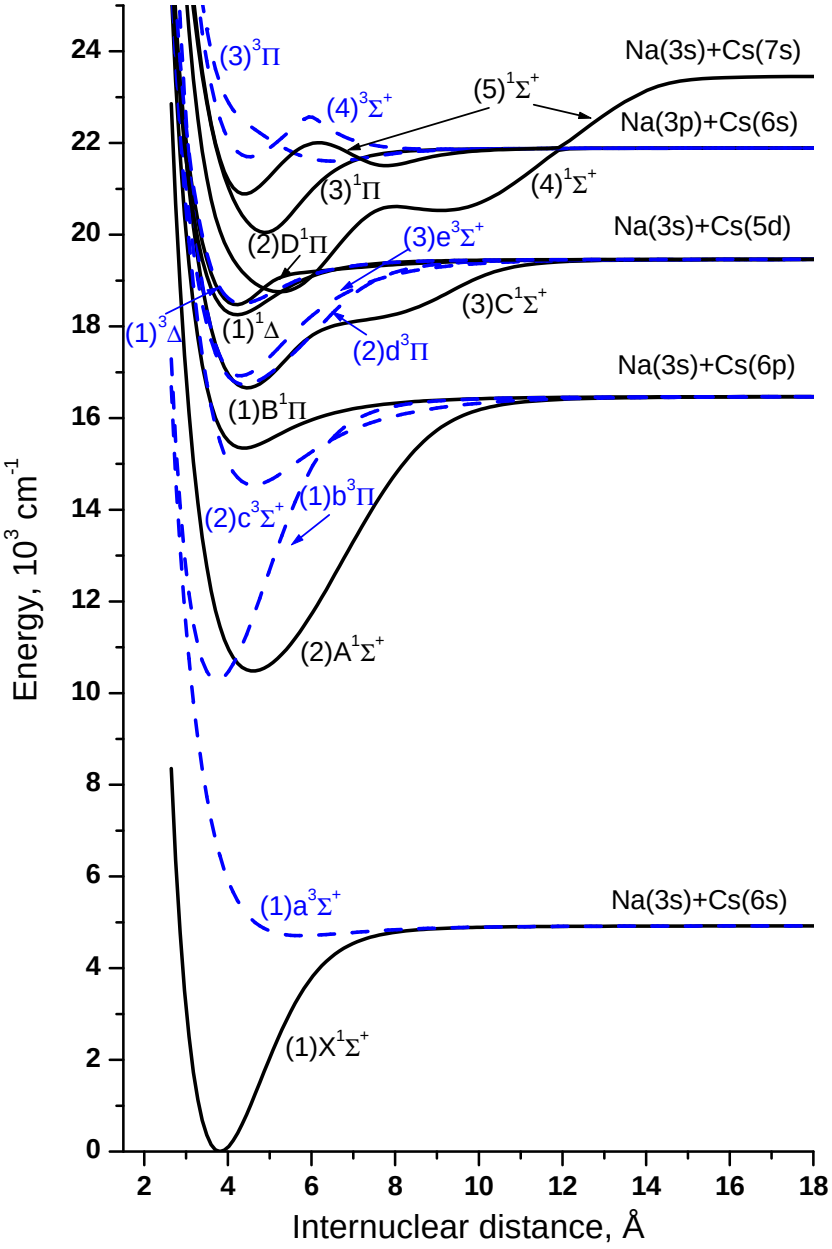

Figure 5.1. Low singlet and triplet electronic states in NaCs according to Ref. [35].

decay into a bound molecular ground state.

Calculations of NaCs long-range potentials are found in [78, 79, 80, 81].

5.2 NaCs $X^1\Sigma^+$ state [dis6]

The **goal** of the present investigation was to study the ground $X^1\Sigma^+$ electronic state of NaCs in a wide range of internuclear distances with the help of the Fourier-transform spectroscopy.

5.2.1 Experiment

Experimental details are found in Section 3.2. Strong laser-induced fluorescence (LIF) was observed when the sample was illuminated with Ar^+ laser operated at lines: 514.5, 496.5, 488.0, 476.5 nm (single mode) and by a single mode dye laser with Rhodamine 6G dye. This allowed us to observe the $(3)^1\Pi - X^1\Sigma^+$, $(2)^1\Pi - X^1\Sigma^+$ and $(4)^1\Sigma^+ - X^1\Sigma^+$ transitions in NaCs along with Na_2 progressions. As the working temperatures were relatively low, the Na_2 signals were weak and did not disturb the measurement and the identification of the NaCs bands. Pure Cs_2 bands were not observed during these experiments.

Ar^+ lines 514.5 and 496.5 nm excited the $(3)^1\Pi - X^1\Sigma^+$ and $(4)^1\Sigma^+ - X^1\Sigma^+$ transitions in NaCs. Ar^+ lines 488.0 and 476.5 nm excited only the $(3)^1\Pi$ state. Overall 55 $(3)^1\Pi - X^1\Sigma^+$ and 14 $(4)^1\Sigma^+ - X^1\Sigma^+$ progressions were assigned. The frequency of the Rhodamine 6G laser was varied between 17527 cm^{-1} and 17768 cm^{-1} which allowed us to record and assign about 40 $(2)^1\Pi \rightarrow X^1\Sigma^+$ and 10 $(4)^1\Sigma^+ \rightarrow X^1\Sigma^+$ progressions.

Due to a considerable extension of the $(4)^1\Sigma^+$ potential in internuclear separation, see Fig. 5.1, it was possible to observe transitions to high vibrational levels of the ground state (up to $v'' = 83$) close to the dissociation limit.

5.2.2 Analysis and potential construction

The assignment of the recorded spectra was simplified by the published $X^1\Sigma^+$ state RKR potential in Ref. [101]. After we identified the strongest progressions, a spline-pointwise potential was fitted to the differences of the transition frequencies similarly to the case of NaRb. This preliminary potential was further improved adding more newly collected experimental data in the fit; this sequential procedure allows continuous checking of the assignment, especially for high J'' and in case of gaps in v''. The total data set (Fig. 5.2) consists of more than 5070 transitions corresponding to 2892 different ground state levels in NaCs.

Fig. 5.3 gives a short section of the many recordings to show the quality of data and also the reliability of the extrapolation to the atomic ground state asymptote; the last observed level is $v'' = 83$. This progression is given as an example having low $J'' = 10, 12$ to reduce the influence of the centrifugal potentials in the energy scale very much getting a proper extrapolation. The calculation with the potential derived below predicts that $v'' = 84$ would be the last bound vibrational level for these J'' values.

For the construction of the empirical PEC of the ground state we used both spline-pointwise and analytic potentials.

Analytic potential is represented as a truncated expansion over analytic functions (2.55), where fitting parameters are a_i. This analytic form is used in the interval $R_i < R < R_o$. For the long-range region $R \geq R_o$ the following expression is applied:

$$U_{\rm LR}(R) = D_e - \frac{C_6}{R^6} - \frac{C_8}{R^8} - \frac{C_{10}}{R^{10}} - E_{ex}, \tag{5.1}$$

where exchange energy is

$$E_{ex} = A_{ex} R^{\gamma} \exp(-\beta R). \tag{5.2}$$

Parameters β and γ are estimated as discussed for heteronuclear species in [82] from the atomic ionization energies of Na and Cs, see Eq. 2.20. C_6, C_8 and C_{10} were fixed to their most recent theoretical values from Refs. [81, 80]. D_e and A_{ex} were fitted. R_m, b and the connecting points R_i and R_o were kept fixed to values, which allowed fast convergence of the fitting routine.

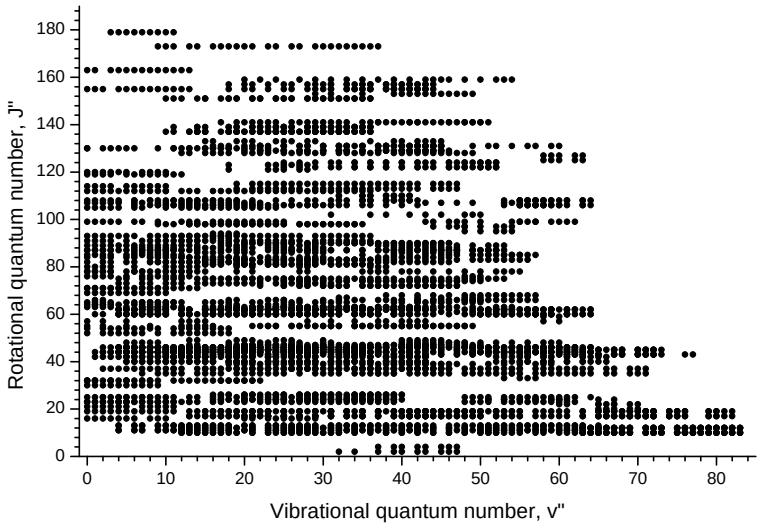

Figure 5.2. The range of vibrational and rotational quantum numbers of the observed ground state energy levels in NaCs.

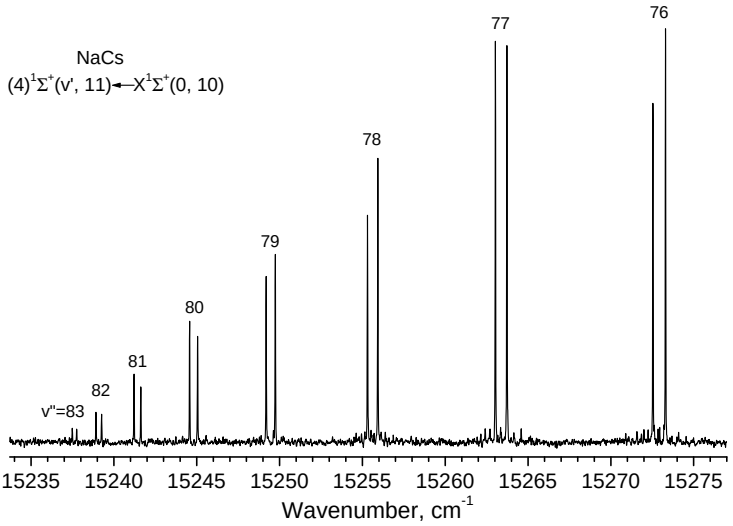

Figure 5.3. The vibrational progression up to $v'' = 83$ in NaCs excited by a single mode Ar^+ laser line 496.5 nm.

For short internuclear distances $R \leq R_i$ the potential is smoothly extended with the expression

$$U_{\mathrm{SR}}(R) = A \exp(-B(R - R_i)), \tag{5.3}$$

where A and B were adjusted in order to ensure smooth connection between the extension and the analytic form.

For the fit 29 potential coefficients according to Eq. (2.55) were used which allowed us to fit almost all observations within experimental accuracy. Only levels with a turning point larger than about 12 Å showed systematic deviations. Table 5.1 gives the derived parameters of the potential, describing the experimental data with a normalized standard deviation $\bar{\sigma} = 0.88$. Using the potential, eigenvalues of the radial Schrödinger equation can be derived in the quantum number limits according to the overview in Fig. 5.2 with an averaged accuracy of better than 0.003 cm^{-1}.

Spline-pointwise potential was constructed similarly to the case of the NaRb $X^1\Sigma^+$ state, described in Section 4.3.3. The final potential contains 51 points and is given in Table 5.2. Experimental data for $v'' < 84$ and $J'' < 180$ are reproduced with a standard deviation 0.0029 cm^{-1} and dimensionless standard deviation 0.61. Note, that in the case of the spline-pointwise potential the contribution of the exchange energy is incorporated into the C_{10}/R^{10} term, thus C_{10} being an effective parameter.

In the traditional way we performed also fits of the observed energy levels to the Dunham power expansion (2.31). The fit gives a standard deviation 0.0027 cm^{-1} and a normalized standard deviation 0.73 for $v'' < 84$ and $J'' < 180$, comparable to the result of the potential fit. For $v'' < 61$ and $J'' < 180$ the corresponding parameters are 0.0023 cm^{-1} and 0.61. This representation of all energy levels by 56 parameters Y_{lm} is contained in Table 5.3 and will give more reliable calculations of energy levels compared to those Y_{lm} reported in Ref. [101] because of their limited data set.

5.2.3 Discussion

From the very large body of highly resolved fluorescence data we could derive a potential energy curve of the $X^1\Sigma^+$ state with the correct asymptotic behavior. Experimental data cover 99.97% of the potential well depth. The extrapolation of the potential for large internuclear separations starts at the largest classical turning point 15.28 Å from the highly-lying level $v'' = 83$, $J'' = 12$ and covers the small extrapolation energy 1.4 cm^{-1} from the rotationless asymptote. If we assume that the theoretical values of the dispersion coefficients have an accuracy of about 1% for C_6 and 10% for the others then the extrapolated dissociation energy results to the very precise value $D_e = 4954.18 \pm 0.10$ cm^{-1}. The exchange energy does not influence the estimation because at these large internuclear separations its value is already significantly smaller than the dispersion contributions (Le Roy radius for the NaCs ground state is 11.9 Å). The new D_e value is in excellent agreement with the first estimation made in Ref. [101], but a factor of 10^3 more precise. Also the newly determined potential functions and the Dunham parameters supersede the earlier published results significantly.

Reporting the dissociation energy with respect to the unobservable minimum of a potential curve introduces a model dependence by the different kinds of setting up the potential curve which results in slight variations of the potential minimum but perfect representation of the vibrational ladder. To remove this ambiguity it is much better to relate the dissociation asymptote to an observable level. Here we use $v'' = 0$, $J'' = 0$, giving the dissociation energy with the symbol D_0 according to the generally accepted nomenclature of molecular spectroscopy: $D_0 = 4904.836 \pm 0.10$ cm^{-1}.

With our precise data on the ground state of NaCs we can check the identification of the observation by A. Kopystynska *et al.* [102] to be a vibrational progression of the $a^3\Sigma^+$ state. As we were also using the laser line 514.5 nm for excitation, we simply compared their recording with ours and our assignment. It became immediately clear that their observation is a part of a progression to the ground state $X^1\Sigma^+$ with high vibrational levels 54 to 58. This explains the small value of the observed vibrational spacing of 46 cm^{-1} compared to 99 cm^{-1} at the bottom of the potential well, but still being much too large to be the vibrational spacing of the $a^3\Sigma^+$ state. The position of this progression, appearing as if it were a separated band, is related to the intensity distribution according to the FCFs between $(4)^1\Sigma^+$ and $X^1\Sigma^+$ observed in this experiment.

Table 5.1. Parameters of the analytic representation (Eqs. 2.55, 5.1, 5.3) of the potential energy curve of the $X^1\Sigma^+$ state in NaCs.

for $R \leq 2.80$ Å	
R_i	2.80 Å
A	5509.4338 cm^{-1}
B	1.5020227100 $Å^{-1}$
for 2.80 Å $< R <$ 12.70 Å	
b	-0.4000
R_m	3.85062906 Å
a_0	0.0 cm^{-1}
a_1	1.29677346150536610 cm^{-1}
a_2	$1.51728492476490264 \times 10^4$ cm^{-1}
a_3	$1.09095191433899363 \times 10^4$ cm^{-1}
a_4	$-2.45806495177720808 \times 10^3$ cm^{-1}
a_5	$-1.60799862149231794 \times 10^4$ cm^{-1}
a_6	$-8.70962559205579782 \times 10^3$ cm^{-1}
a_7	$2.18747535596727575 \times 10^4$ cm^{-1}
a_8	$-3.00243720449833432 \times 10^5$ cm^{-1}
a_9	$-7.86930451496603433 \times 10^5$ cm^{-1}
a_{10}	$3.39616970842697797 \times 10^6$ cm^{-1}
a_{11}	$7.35841534829050489 \times 10^6$ cm^{-1}
a_{12}	$-2.63747919952689409 \times 10^7$ cm^{-1}
a_{13}	$-4.45851005134318396 \times 10^7$ cm^{-1}
a_{14}	$1.35133654058888495 \times 10^8$ cm^{-1}
a_{15}	$1.76262769398831815 \times 10^8$ cm^{-1}
a_{16}	$-4.75687836575036168 \times 10^8$ cm^{-1}
a_{17}	$-4.47488337869063497 \times 10^8$ cm^{-1}
a_{18}	$1.21600041878172946 \times 10^9$ cm^{-1}
a_{19}	$7.46075675097115278 \times 10^8$ cm^{-1}
a_{20}	$-2.29173360205131388 \times 10^9$ cm^{-1}
a_{21}	$-8.70893719909687042 \times 10^8$ cm^{-1}
a_{22}	$3.09544150282176447 \times 10^9$ cm^{-1}
a_{23}	$8.19954467973030806 \times 10^8$ cm^{-1}
a_{24}	$-2.80675453436517239 \times 10^9$ cm^{-1}
a_{25}	$-6.96373081872487426 \times 10^8$ cm^{-1}
a_{26}	$1.51653594722299957 \times 10^9$ cm^{-1}
a_{27}	$4.44558531531333089 \times 10^8$ cm^{-1}
a_{28}	$-3.66990684866598368 \times 10^8$ cm^{-1}
a_{29}	$-1.35242647548431933 \times 10^8$ cm^{-1}
for $R \geq 12.70$ Å	
R_o	12.700 Å
D_e	4954.1847 cm^{-1}
C_6	1.550513×10^7 $cm^{-1}Å^6$
C_8	4.88540×10^8 $cm^{-1}Å^8$
C_{10}	1.7170×10^{10} $cm^{-1}Å^{10}$
A_{ex}	2.834990×10^4 $cm^{-1}Å^{-\gamma}$
γ	5.12271
β	2.17237 $Å^{-1}$

Table 5.2. List of the grid points of the spline-pointwise potential energy curve of the NaCs $X^1\Sigma^+$ state.

R (Å)	$U(R)$ (cm^{-1})	R (Å)	$U(R)$ (cm^{-1})
2.44	14592.03265	5.309291	2607.833543
2.54555	10993.97179	5.449736	2883.018858
2.65109	8333.922936	5.590181	3137.577798
2.75664	6200.27792	5.764437	3422.509004
2.86219	4704.209791	5.938693	3672.385991
2.967731	3546.457589	6.112949	3888.024578
3.073277	2601.150555	6.287205	4071.548022
3.178824	1838.927902	6.461461	4225.913132
3.28437	1236.46165	6.680398	4383.779883
3.389916	774.199269	6.899335	4507.87088
3.495462	434.903063	7.118272	4604.627148
3.601008	202.904811	7.410188	4700.743554
3.706555	63.776331	7.702104	4769.014757
3.812101	4.28667	7.99402	4817.532712
3.917647	12.343243	8.285935	4852.165924
4.023193	76.966249	8.577851	4877.058744
4.139968	202.475109	8.979235	4900.534908
4.256742	373.217075	9.38062	4915.981072
4.373517	578.740103	9.782004	4926.263296
4.490291	809.884575	10.183388	4933.429883
4.607066	1058.7412	10.986157	4942.059957
4.747511	1371.899737	11.788925	4946.650014
4.887956	1690.807508	12.591694	4949.386034
5.028401	2007.251894	13.394463	4951.0261
5.168846	2314.638541	14.197231	4951.974865
$R_{\text{out}} = 12.3$ Å			
$D_e = 4954.18655$ cm^{-1}		$C_8 = 4.8851 \cdot 10^8$ $cm^{-1}Å^8$	
$C_6 = 1.54962 \cdot 10^7$ $cm^{-1}Å^6$		$C_{10} = 1.8884 \cdot 10^{10}$ $cm^{-1}Å^{10}$	

Table 5.3. Dunham coefficients (in cm^{-1}) for the NaCs ground state.

$Y_{1,0}$	98.8786618		$Y_{0,2}$	-0.796345	$\times 10^{-7}$
$Y_{2,0}$	-0.32115		$Y_{1,2}$	-0.41069	$\times 10^{-9}$
$Y_{3,0}$	-0.256	$\times 10^{-2}$	$Y_{3,2}$	-0.46707	$\times 10^{-12}$
$Y_{4,0}$	0.42816	$\times 10^{-3}$	$Y_{5,2}$	0.572237	$\times 10^{-15}$
$Y_{5,0}$	-0.62317	$\times 10^{-4}$	$Y_{8,2}$	-0.4369589	$\times 10^{-19}$
$Y_{6,0}$	0.60947	$\times 10^{-5}$	$Y_{9,2}$	0.15324	$\times 10^{-20}$
$Y_{7,0}$	-0.4233446	$\times 10^{-6}$	$Y_{10,2}$	-0.159217	$\times 10^{-22}$
$Y_{8,0}$	0.214274	$\times 10^{-7}$	$Y_{13,2}$	0.10775	$\times 10^{-28}$
$Y_{9,0}$	-0.8045518	$\times 10^{-9}$	$Y_{15,2}$	-0.657872	$\times 10^{-33}$
$Y_{10,0}$	0.2263192	$\times 10^{-10}$	$Y_{0,3}$	0.8108	$\times 10^{-13}$
$Y_{11,0}$	-0.478034677	$\times 10^{-12}$	$Y_{1,3}$	-0.19155	$\times 10^{-14}$
$Y_{12,0}$	0.7537892	$\times 10^{-14}$	$Y_{2,3}$	0.17507	$\times 10^{-15}$
$Y_{13,0}$	-0.873440396	$\times 10^{-16}$	$Y_{6,3}$	-0.869044	$\times 10^{-21}$
$Y_{14,0}$	0.721486439	$\times 10^{-18}$	$Y_{8,3}$	0.16785	$\times 10^{-23}$
$Y_{15,0}$	-0.401878463	$\times 10^{-20}$	$Y_{9,3}$	-0.354	$\times 10^{-25}$
$Y_{16,0}$	0.135217881	$\times 10^{-22}$	$Y_{11,3}$	0.389062	$\times 10^{-29}$
$Y_{17,0}$	-0.207498958	$\times 10^{-25}$	$Y_{13,3}$	-0.218846	$\times 10^{-33}$
$Y_{0,1}$	0.580099	$\times 10^{-1}$	$Y_{1,4}$	0.31764	$\times 10^{-19}$
$Y_{1,1}$	-0.2313	$\times 10^{-3}$	$Y_{2,4}$	-0.618678	$\times 10^{-20}$
$Y_{2,1}$	-0.12837	$\times 10^{-5}$	$Y_{6,4}$	0.17395	$\times 10^{-25}$
$Y_{3,1}$	0.965	$\times 10^{-8}$	$Y_{8,4}$	-0.2046	$\times 10^{-28}$
$Y_{4,1}$	-0.8798	$\times 10^{-9}$	$Y_{10,4}$	0.101431	$\times 10^{-31}$
$Y_{6,1}$	0.4168	$\times 10^{-12}$	$Y_{12,4}$	-0.45229	$\times 10^{-35}$
$Y_{8,1}$	-0.3308	$\times 10^{-15}$	$Y_{13,4}$	0.747789	$\times 10^{-37}$
$Y_{9,1}$	0.5194886	$\times 10^{-17}$	$Y_{14,4}$	-0.424822	$\times 10^{-39}$
$Y_{11,1}$	-0.391816	$\times 10^{-21}$	$Y_{2,5}$	0.46738	$\times 10^{-25}$
$Y_{13,1}$	0.1753605	$\times 10^{-25}$	$Y_{7,5}$	-0.133787	$\times 10^{-31}$
			$Y_{8,5}$	0.56824584	$\times 10^{-33}$
			$Y_{9,5}$	-0.616878	$\times 10^{-35}$

During the present experiment we have collected a large set of term values for excited states, particularly the $(3)^1\Pi$ state. These levels together with the collisionally excited levels were used for obtaining the spline-pointwise PEC of the $(3)^1\Pi$ state [105].

5.2.4 Results and conclusions

1. High-resolution LIF spectra to the NaCs $X^1\Sigma^+$ ground state were obtained for the first time using the FTS method. The obtained data set consists of more than 5070 transitions corresponding to 2892 different ground state levels in the range $v' = 0 - 83$, $J' = 2 - 179$.

2. Transition frequencies were used for a direct fit of the analytic and spline-pointwise potential energy curves. Analytic potential (29 parameters) reproduces experimental data with $\sigma = 0.003$ cm^{-1} and $\bar{\sigma} = 0.88$, whereas spline-pointwise PEC (51 parameter) with $\sigma = 0.0029$ cm^{-1} and $\bar{\sigma} = 0.61$.

3. Experimental PEC covers 99.97% of the potential well depth. The classical turning point of the last observed energy level ($v'' = 83$, $J'' = 12$) is around 15.3 Å and this level is about 1.4 cm^{-1} below the asymptote.

4. A new, more accurate value of dissociation energy is obtained with the present potential $D_e = 4954.18 \pm 0.10$ cm^{-1}.

5. Term energies were also fitted to the Dunham expansion. The obtained set of constants reproduces the experimental term energies for with $\sigma = 0.0027$ cm^{-1} and $\bar{\sigma} = 0.73$.

5.3 Combined analysis of the NaCs $a^3\Sigma^+$ and $X^1\Sigma^+$ states

The $a^3\Sigma^+$ state of NaCs has never been studied experimentally before. At the same time there is a need of accurate spectroscopic data on the lowest triplet state. Therefore the **goal** of the present experiments was to collect experimental information on the NaCs $a^3\Sigma^+$ state, especially close to the asymptote and to perform a combined analysis of the $a^3\Sigma^+$ and $X^1\Sigma^+$ states, taking into account their hyperfine mixing close to the asymptote. In order to study the $a^3\Sigma^+$ state we decided to apply the same technique as for the NaRb $a^3\Sigma^+$ state, i.e. to reach the triplet manifold through mixed singlet–triplet complex.

5.3.1 Observations

The first observation of transitions to the $a^3\Sigma^+$ state was made by us using a Rhodamine 6G single mode dye laser [dis6]. Electronic structure calculations [35], see Fig. 5.1, show that there could be a coupling between the $(3)C^1\Sigma^+$ state and a triplet state. However, with Rh6G we were able to observe only one rather weak progression under excitation at 17344 cm^{-1}. Excitation region was also unfavorable due to strong Na_2 emission. Identification was done based on the *ab initio* potential of $a^3\Sigma^+$ taken from Ref. [35], however assignment was not unambiguous due to absence of the corresponding singlet transition from the same upper state level.

In the next experiments we decided to excite the $B^1\Pi$, $b^3\Pi$ and $c^3\Sigma^+$ complex of NaCs, similarly to the case of NaRb. It should be noted that this complex has never been studied before unlike in NaRb. Energy considerations based on Fig. 5.1 allowed us to choose the appropriate excitation region, which corresponds to the lasing of the DCM dye. Thus we excited transitions to levels of the $B^1\Pi$, $b^3\Pi$ and $c^3\Sigma^+$ complex, and observed emission to the $X^1\Sigma^+$ and $a^3\Sigma^+$ states. Fluorescence to the lowest triplet state was rather strong. Na_2 signals were also sometimes intense, but did not disturb measurements and identification of the NaCs B→X bands. Pure Cs_2 bands were not observed during these experiments. The frequency of the DCM laser was gradually varied between 14966 cm^{-1} and 15882 cm^{-1}. The lowest excitation frequency at which triplet band appeared was ca. 15145 cm^{-1}. Fig. 5.4 presents a typical fluorescence spectrum, where along with the B→X band system a weaker band appears around 11000 cm^{-1} due to decay to the $a^3\Sigma^+$ state.

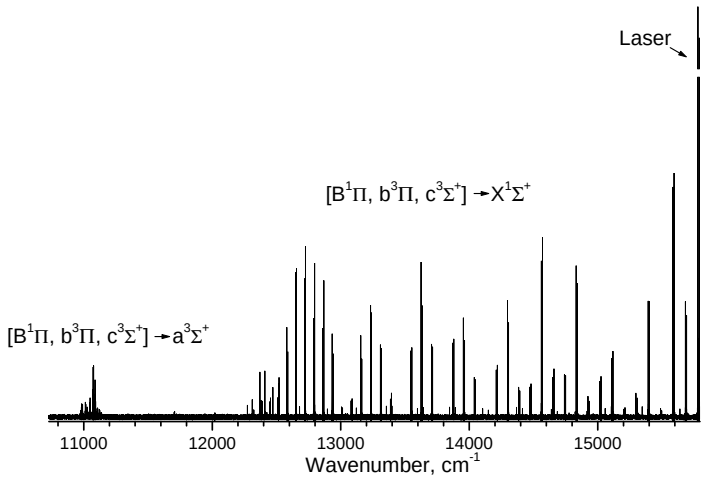

Figure 5.4. The $B^1\Pi \rightarrow X^1\Sigma^+$ and $\left[B^1\Pi,\ b^3\Pi,\ c^3\Sigma^+\right] \rightarrow a^3\Sigma^+$ bands of NaCs excited with a single mode DCM laser at frequency of 15788.934 cm^{-1}.

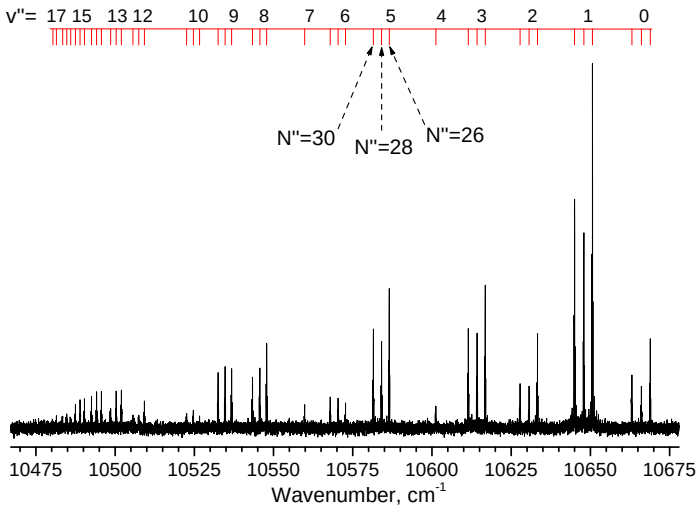

Figure 5.5. $[B^1\Pi, b^3\Pi, c^3\Sigma^+] \rightarrow a^3\Sigma^+$ progression in NaCs, excited with a single mode DCM laser at frequency of 15337.256 cm^{-1}. The exciting transition is $B^1\Pi\,(0, 28) \leftarrow X^1\Sigma^+\,(0, 28)$.

5.3.2 Spectra analysis

In order to be able to assign transitions to the $a^3\Sigma$ state, at the early stage of experiments we always recorded $B^1\Pi \rightarrow X^1\Sigma^+$ transitions together with the $[B^1\Pi, b^3\Pi, c^3\Sigma^+] \rightarrow a^3\Sigma^+$ ones, see Fig. 5.4. Identification of B→X bands was straightforward thanks to high accuracy $X^1\Sigma^+$ state spline-pointwise PEC obtained previously (see Table 5.2). In transitions to the lowest triplet state we observed progressions of two types: doublets and triplets, and we explain this structure by the same considerations as in NaRb (see Chapter 4.4.1 and Fig. 4.10). Typical example of triplet progression can be seen in Fig. 5.5.

For assigning of a progression to the $a^3\Sigma^+$ state it was necessary to find the singlet progression coming from the same upper state level. For finding the correspondence between the singlet and triplet progression we searched for relaxation lines of the singlet transitions and using them calculated excitation energy for the neighboring J' level and put the laser at this new frequency. If the hypothesis were true then we were able to observe the triplet spectra shifted relative to the old one. In such a way N'' value for transitions to the $a^3\Sigma^+$ state was assigned. For vibrational numbering some initial relative numbering was chosen based on the longest progressions. When $a^3\Sigma^+$ state energies at some N'' values (> 5) for different vibrational levels were collected, we fitted these term values to molecular constants and then used them for identification of several new progressions, always checking assignment with the help of the singlet band. The next step was fitting a spline-pointwise PEC [48] to the new data. The obtained potential was then gradually improved when more energy levels were added.

However, it was not always possible to find the corresponding singlet transition (the excited level could be with so strong triplet character that the resulting singlet fluorescence is very weak, or B→X FCF are small). In this case and also when singlet spectra were not available (for improving the SNR we filtered out the singlet band at the later stage of measurements) N'' identification was always checked by laser resonance in X→B transition.

A very interesting feature observed in transitions to the $a^3\Sigma^+$ state was that after Q excitation we found rather different intensity distributions among multiplet components for different progressions, see e.g. Fig. 5.6. As can be seen, sometimes the central component of the triplet completely disappeared and we observed doublet with N'-2 and N'+2. Such structure is probably explained by the influence of the strongly perturbed upper state wavefunction and will be investigated in the studies of the $[B^1\Pi, b^3\Pi, c^3\Sigma^+]$ complex.

As a result, we have obtained the data set for the $a^3\Sigma^+$ state consisting of more than 3000 transition

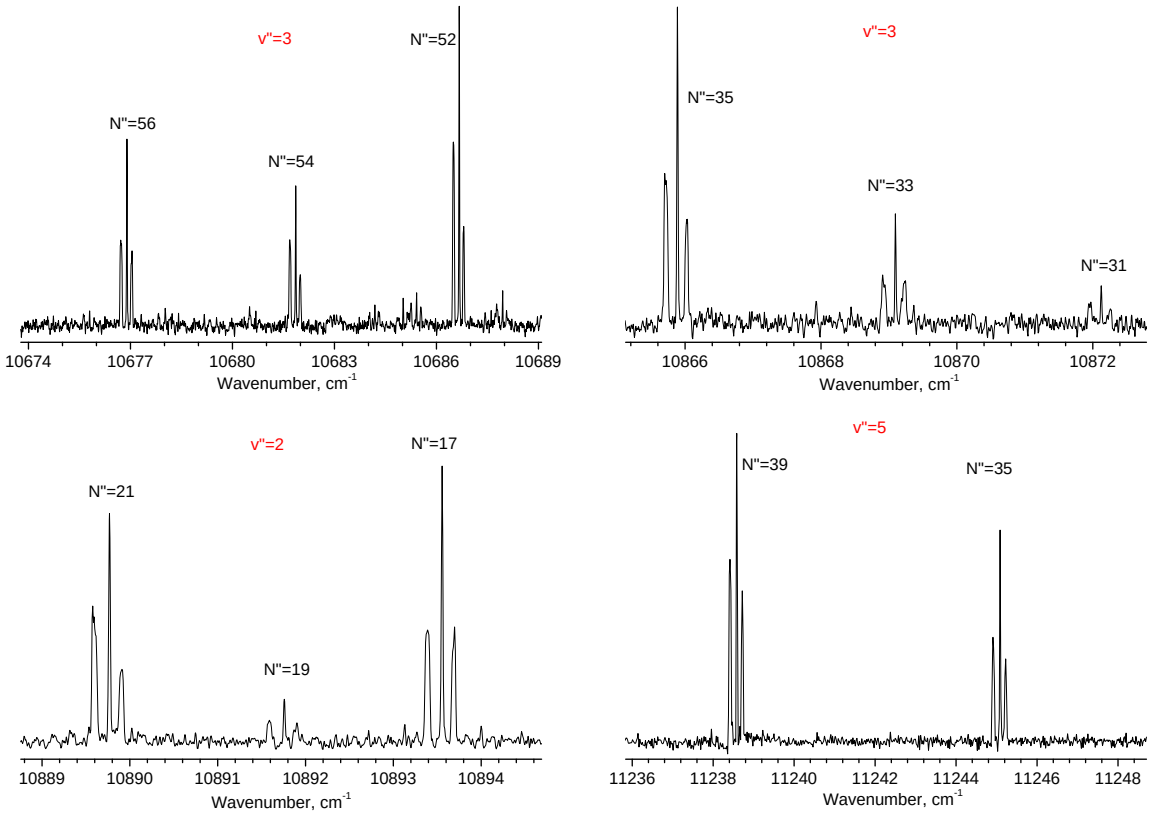

Figure 5.6. Examples of different intensity distributions among multiplet components at Q excitation.

frequencies to ca. 940 energy levels as shown in Figure 5.7. Uncertainty was estimated to 0.003 cm^{-1}. The range of observed vibrational and rotational quantum numbers is $6 < N'' < 103$, $0 < v'' < 19$. The last observed level is $v'' = 19$, $N'' = 25$, which has a classical turning point around 14.2 Å.

In our experiments we also observed several spectra caused by the long-range changeover similarly to the case of NaRb [dis3]. Thus transitions to high vibrational levels of the $X^1\Sigma^+$ state were found together with the $a^3\Sigma^+$ transitions and enriched the data field of the $X^1\Sigma^+$ state. However these spectra were rare and the highest v'' did not exceed the previously reached v_X=83, see e.g. Fig. 5.8.

5.3.3 Hyperfine structure

At the resolution used in the experiments (typically 0.015-0.03 cm^{-1}) the hyperfine structure (HFS) of the triplet lines was partially resolved. Analysis showed that the hyperfine splitting of the $a^3\Sigma^+$ levels is described within a Hund's case ($b_{\beta S}$) coupling scheme and is caused by the Fermi contact interaction like in the $a^3\Sigma^+$ state of NaRb. The observed structure is well described by atomic HFS parameters for levels not close to the asymptote (see Fig. 5.9). The strong deviations from the observed pattern appear for $v_a = 16$, which will be explained below by taking into account hyperfine mixing of the weakly bound $X^1\Sigma^+$ and $a^3\Sigma^+$ levels. The hyperfine-structure-free positions of the triplet state levels are shifted from the central component of the hyperfine pattern by 0.039 cm^{-1} for NaCs.

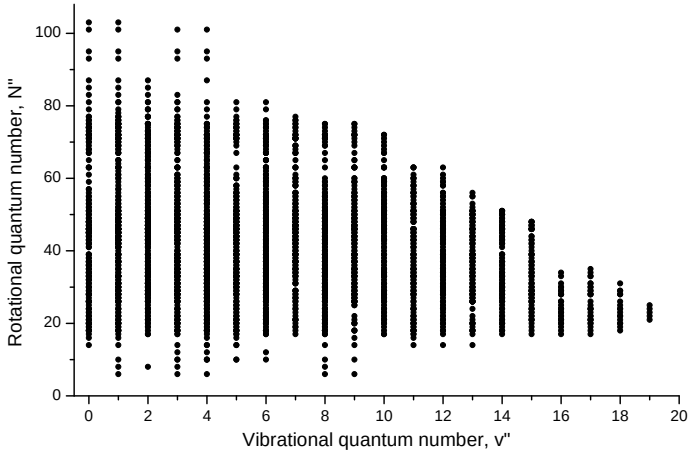

Figure 5.7. The range of vibrational and rotational quantum numbers of the observed energy levels in the $a^3\Sigma^+$ state of NaCs.

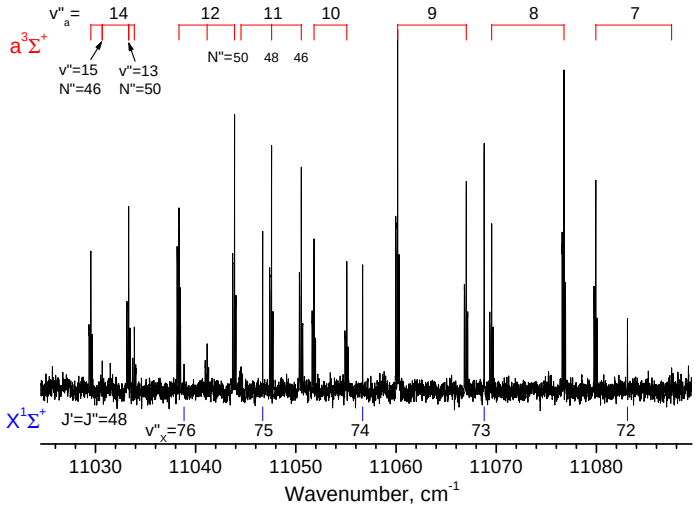

Figure 5.8. A piece of NaCs LIF spectrum excited at frequency 15805.510 cm^{-1}, where both progressions to the $X^1\Sigma^+$ and $a^3\Sigma^+$ states from a common upper level (v'_B=11, $J' = N' = 48$) can be seen within the same energy region due to the long-range changeover. FCFs of the $B^1\Pi$-$X^1\Sigma^+$ transition in this region are zero. Energy of the excited state level is 15990.581 cm^{-1}.

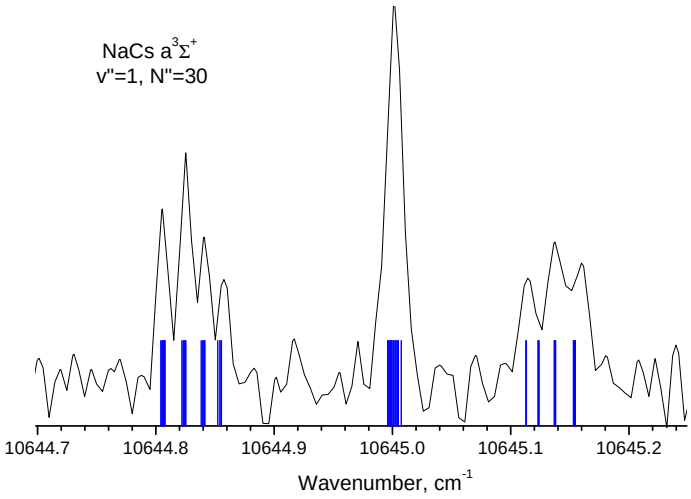

Figure 5.9. Typical hyperfine splitting of the transitions to the $a^3\Sigma^+$ state in NaCs. Vertical lines show the result of coupled channels calculations

5.3.4 Fitting of potentials to experimental observations

Initially experimental data on the $a^3\Sigma^+$ state were fitted to the spline-pointwise potential in a single-potential model. This approach allowed for obtaining of already sufficiently good potential, which however showed systematic deviations for vibrational levels starting from app. $v'' = 15$, which could be an indication of hyperfine mixing between the $X^1\Sigma^+$ and $a^3\Sigma^+$ state. The derived potential was transformed to the analytic form (2.55) and used together with the analytic $X^1\Sigma^+$ state potential from [dis6] for calculating the initial HFS corrections. The next steps of the fitting procedure were the same as in the NaRb case: experimental data were corrected for the HFS shift and then single-channel potentials were fitted; new potentials were used to calculate new corrections, etc. After approximate 5 iterations the fitting procedure converged.

The absolute position of the $a^3\Sigma^+$ state in the energy scale was established using transitions to the ground and lowest triplet state originating from the same upper state level. The $X^1\Sigma^+$ state data set has also been enlarged by data obtained in other experiment [105] with Ar^+ 501.7 nm and Nd:YAG laser providing long $(4)^1\Sigma^+$-$X^1\Sigma^+$ progressions (accuracy of data with Ar^+ 501.7 nm is 0.003 cm^{-1}, Nd:YAG data 0.01 cm^{-1}). Thus data field for the $X^1\Sigma^+$ state was enriched by ca. 1350 frequencies. In total, ca. 9500 frequencies corresponding to about 4700 energy levels of both a and X states were used in the combined fitting procedure.

For the long-range region $R \geq R_o$ the expression (4.4) is applied with some modification: in the present studies potential is given with respect to the atomic asymptote, therefore D is set to 0. C_6, C_8 and C_{10} coefficients and exchange energy parameter A_{ex} were fitted. Parameters β and γ are estimated as discussed for heteronuclear species in Ref. [82] from the atomic ionization energies of Na and Cs, see Eq. 2.20.

For short internuclear distances $R \leq R_i$ the potential is smoothly extended with the expression

$$U_{\rm SR}(R) = A + B/R^{\alpha}, \tag{5.4}$$

where α can be non-integer. Note that this expression differs from the previously used Eq. (5.3).

The derived potentials describe the total data set of the X and a states with a normalized standard deviation of 0.78. The importance of applying the coupled channels approach can be illustrated with the example of transitions to $v''_a = 16$ and $v''_{\rm X} = 79$, see Fig. 5.10. The hyperfine coupling of the X and a state levels is so strong that classification of levels as singlets and triplets becomes ambiguous, which

is confirmed by spin operator expectation values, which value for several HFS components is about 0.5. As can be inferred from Fig. 5.10, the coupled channels approach allows to reproduce the observed HFS pattern with good accuracy.

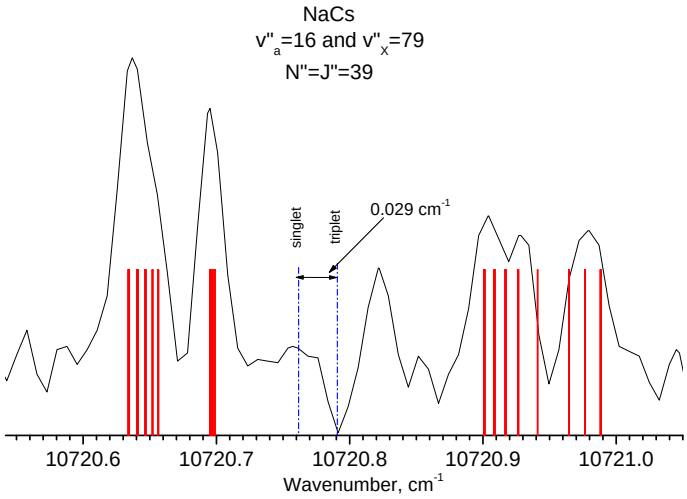

Figure 5.10. Hyperfine mixing of weakly bound singlet ($v''_{\rm X} = 79$) and triplet ($v''_a = 16$) levels with $N''_a = J''_X = 39$. Solid red lines show the eigenvalues obtained with the CCC with the present potentials, and dashed blue lines denote the single-channel eigenenergies.

The obtained dispersion coefficients are in good agreement with theoretical calculations from Refs. [80, 81], see values in Table 5.1. Empirical C_6 and C_8 are in error limits predicted by theory, whereas C_{10} value goes beyond the stated 10% uncertainty interval. Empirical potentials were compared with *ab initio* potentials by Korek *et al.* [35], see Fig. 5.11. We can see that in the case of NaCs *ab initio* potentials of the a and X states are much closer to the empirical ones than it was in NaRb (compare with Fig. 4.21). Quantitatively it is also indicated by *ab initio* dissociation energy values: 214 cm^{-1} for a state and 4923 cm^{-1} for X state.

5.3.5 Results and conclusions

1. Transitions to the $a^3\Sigma^+$ state of NaCs were observed for the first time. Spectra were recorded using high-resolution FTS. More than 3000 transition frequencies to ca. 940 energy levels were assigned. The range of observed vibrational and rotational quantum numbers is $v'' = 0 - 19$ and $N'' = 6 - 103$. The typical experimental uncertainty is 0.003 cm^{-1}.

2. The data set for the $X^1\Sigma^+$ state obtained previously (see [dis6]) was enriched by about 1350 transitions, using B→X, $(4)^1\Sigma^+ \rightarrow X^1\Sigma^+$ bands and transitions caused by the long-range changeover.

3. Both $X^1\Sigma^+$ and $a^3\Sigma^+$ states potentials were fitted simultaneously to analytic potential energy curves smoothly connected to the long-range potential, taking into account the hyperfine mixing of these states close to the asymptote. New potentials reproduce experimental data for the $a^3\Sigma^+$ and $X^1\Sigma^+$ state with $\bar{\sigma} = 0.78$.

4. Long-range coefficients C_6, C_8, C_{10}, as well as exchange energy parameter A_{ex} were fitted. Dispersion potential is in good agreement with the *ab initio* one.

5. Dissociation energies obtained with the present potentials for the $X^1\Sigma^+$ and $a^3\Sigma^+$ states are $D_e^{\rm X} = 4954.22 \pm 0.10$ cm^{-1} and $D_e^a = 217.15 \pm 0.10$ cm^{-1}.

Table 5.4. Parameters of the analytic representation (Eqs. 2.55, 5.1, 5.4) of the potential energy curve of the $a^3\Sigma^+$ state in NaCs. Potential is given with respect to the atomic asymptote.

	for $R \leq 4.78$ Å
A	-0.164777827×10^3 cm^{-1}
B	$0.184208874 \times 10^{19}$ cm^{-1}Å$^{\alpha}$
α	0.236563805×10^2
	for 4.78 Å $< R <$ 10.20 Å
b	-0.6400
R_m	5.75585938 Å
a_0	-217.137992 cm^{-1}
a_1	5.060041760921147 cm^{-1}
a_2	$0.4718687621656754 \times 10^3$ cm^{-1}
a_3	$0.2514219323834187 \times 10^3$ cm^{-1}
a_4	$-0.8746237247738273 \times 10^2$ cm^{-1}
a_5	$-0.2154118954152781 \times 10^3$ cm^{-1}
a_6	$-0.2370010651661931 \times 10^3$ cm^{-1}
a_7	$-0.5975533223022640 \times 10^3$ cm^{-1}
a_8	$-0.4760140339369856 \times 10^3$ cm^{-1}
a_9	$0.3782291928282492 \times 10^3$ cm^{-1}
a_{10}	$0.6798234616502023 \times 10^3$ cm^{-1}
a_{11}	$0.6723220594269379 \times 10^3$ cm^{-1}
a_{12}	$-0.1248173837589433 \times 10^2$ cm^{-1}
a_{13}	$-0.4626112296933644 \times 10^3$ cm^{-1}
	for $R \geq 10.20$ Å
C_6	1.545671×10^7 cm^{-1}Å^6
C_8	5.001807×10^8 cm^{-1}Å^8
C_{10}	2.019156×10^{10} cm^{-1}Å^{10}
A_{ex}	2.549387×10^4 cm^{-1}Å$^{-\gamma}$
γ	5.12271
β	2.17237 Å^{-1}
T_e=$-D_e$	$-217.152(10)$ cm^{-1}
R_e	5.745 Å

Table 5.5. Parameters of the analytic representation (Eqs. 2.55, 5.1, 5.4) of the potential energy curve of the $X^1\Sigma^+$ state in NaCs. Potential is given with respect to the atomic asymptote.

for $R \leq 2.84$ Å	
A	0.900290886×10^4 cm^{-1}
B	-0.113527906×10^3 cm^{-1}Å$^{\alpha}$
α	-4.1859263636
for 2.84 Å $< R <$ 10.20 Å	
b	-0.4000
R_m	3.85062906 Å
a_0	-4954.220839 cm^{-1}
a_1	0.8980684901406436 cm^{-1}
a_2	$0.1517322305891121 \times 10^5$ cm^{-1}
a_3	$0.1091020368289819 \times 10^5$ cm^{-1}
a_4	$-0.2458305183215540 \times 10^4$ cm^{-1}
a_5	$-0.1608232304418994 \times 10^5$ cm^{-1}
a_6	$-0.8705013039210540 \times 10^4$ cm^{-1}
a_7	$0.2188050377166237 \times 10^5$ cm^{-1}
a_8	$-0.3002538567610332 \times 10^6$ cm^{-1}
a_9	$-0.7869349465616797 \times 10^6$ cm^{-1}
a_{10}	$0.3396165702257235 \times 10^7$ cm^{-1}
a_{11}	$0.7358409821995481 \times 10^7$ cm^{-1}
a_{12}	$-0.2637478410754801 \times 10^8$ cm^{-1}
a_{13}	$-0.4458510218550479 \times 10^8$ cm^{-1}
a_{14}	$0.1351336683210848 \times 10^9$ cm^{-1}
a_{15}	$0.1762627711656325 \times 10^9$ cm^{-1}
a_{16}	$-0.4756878196895964 \times 10^9$ cm^{-1}
a_{17}	$-0.4474883318729266 \times 10^9$ cm^{-1}
a_{18}	$0.1216000437575875 \times 10^{10}$ cm^{-1}
a_{19}	$0.7460756869348375 \times 10^9$ cm^{-1}
a_{20}	$-0.2291733580746639 \times 10^{10}$ cm^{-1}
a_{21}	$-0.8708937018563435 \times 10^9$ cm^{-1}
a_{22}	$0.3095441525806588 \times 10^{10}$ cm^{-1}
a_{23}	$0.8199544778248683 \times 10^9$ cm^{-1}
a_{24}	$-0.2806754519640437 \times 10^{10}$ cm^{-1}
a_{25}	$-0.6963731310931557 \times 10^9$ cm^{-1}
a_{26}	$0.1516535914525204 \times 10^{10}$ cm^{-1}
a_{27}	$0.4445582767694474 \times 10^9$ cm^{-1}
a_{28}	$-0.3669909023138414 \times 10^9$ cm^{-1}
a_{29}	$-0.1352434700004024 \times 10^9$ cm^{-1}
for $R \geq 10.20$ Å	
C_6	1.545671×10^7 cm^{-1}Å^6
C_8	5.001807×10^8 cm^{-1}Å^8
C_{10}	2.019156×10^{10} cm^{-1}Å^{10}
A_{ex}	2.549387×10^4 cm^{-1}Å$^{-\gamma}$
γ	5.12271
β	2.17237 Å^{-1}
T_e=$-D_e$	$-4954.221(10)$ cm^{-1}
R_e	3.851 Å

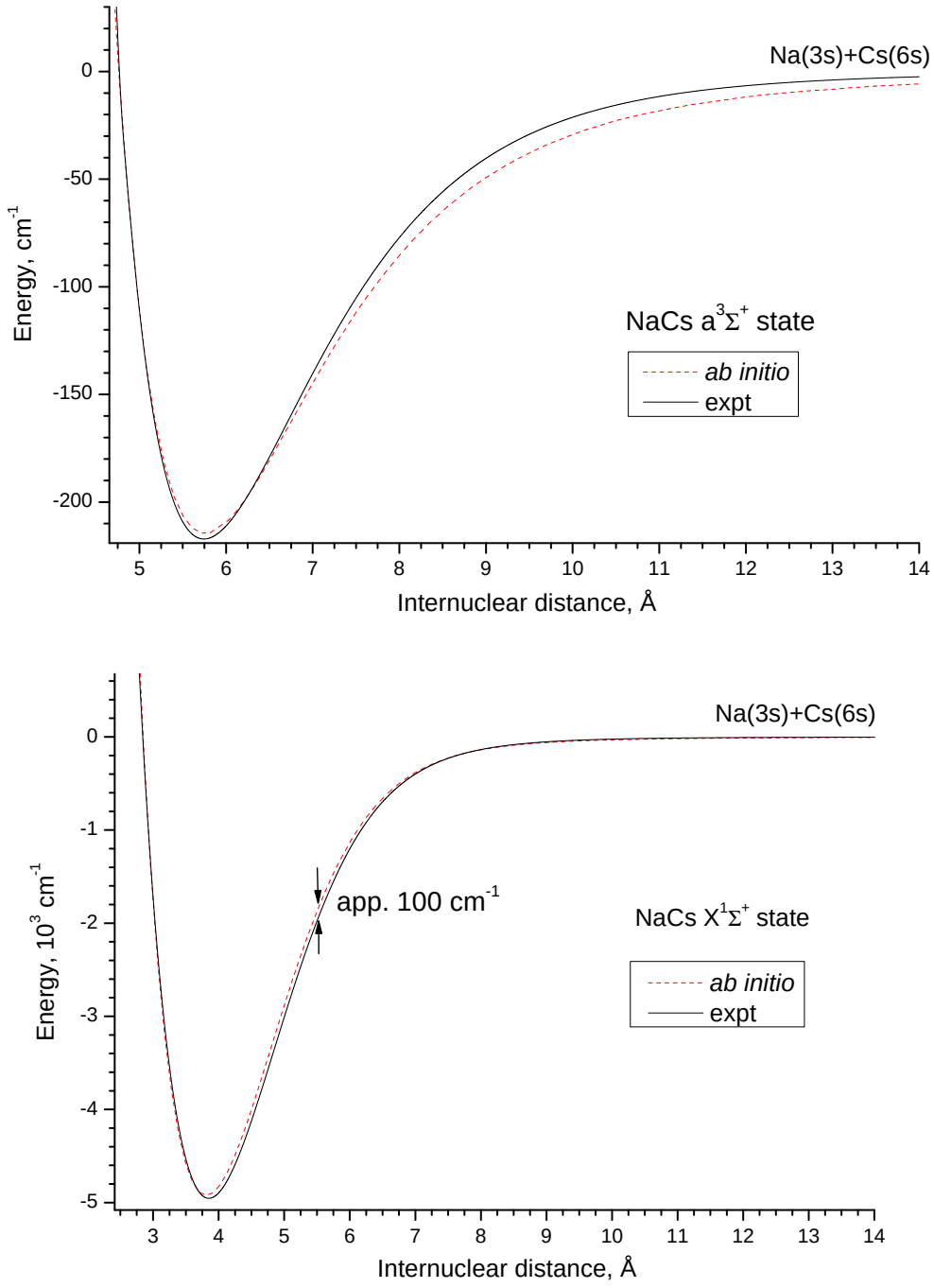

Figure 5.11. Comparison of the present empirical NaCs $a^3\Sigma^+$ and $X^1\Sigma^+$ state potentials with *ab initio* potentials from Ref. [35].

Chapter 6

Conclusions

In consistence with the goals and tasks of the present work the following **main results** have been obtained:

- For the first time the NaRb ground $X^1\Sigma^+$ state and lowest triplet $a^3\Sigma^+$ state have been studied experimentally in a wide range of internuclear distances with high accuracy. Spline-pointwise empirical potential energy curves were obtained in a combined fitting procedure taking into account the hyperfine mixing of these states close to the asymptote. The obtained potentials allow for adequate modeling of cold collision experiments with Na-Rb pairs.
- A first detailed experimental study of the NaRb excited $C^1\Sigma^+$ state converging to the Na(3p) + Rb(5s) states of separated atoms has been performed. The obtained data were incorporated into a direct fit of a single spline-pointwise potential energy curve to the level energies. This method allowed for description of this state including the shelf region.
- A detailed experimental study of the NaRb $D^1\Pi$ state converging to the Na(3p) + Rb(5s) atomic limit has been performed for the first time with high resolution. The obtained data were incorporated into a direct fit of a single spline-pointwise potential energy curve to the level energies. The $D^1\Pi$ state q factors, which describe the Λ-doubling, have been obtained in a wide range of rotational and vibrational quantum numbers. The rotational dependence of q-factors has been derived. Analysis revealed several local perturbation regions in the $D^1\Pi$ state.
- For the first time the NaCs ground $X^1\Sigma^+$ state has been studied experimentally in a wide range of internuclear distances with high accuracy. The lowest triplet $a^3\Sigma^+$ state has been observed for the first time and studied at high resolution in a wide range of internuclear distances. Analytical empirical potential energy curves of the $X^1\Sigma^+$ and $a^3\Sigma^+$ states were obtained in a combined fitting procedure taking into account the hyperfine mixing of these states close to the asymptote.

Concluding remarks

- Our work has demonstrated that Fourier transform spectroscopy of laser induced fluorescence is a powerful tool for studying not only of ground states, but also excited states due to collision induced transitions. Analysis of rotational satellites allows enlarging of the data sets significantly. In this sense collision facilitated FTS LIF method can be considered for excited states as a method, competing and complementary to two laser pump-probe spectroscopy experiments. Its main advantages are relative easiness of the experiment, high accuracy and fast measurements.
- Applying of direct potential fit analysis allowed us to obtain empirical potential energy curves from the observations. This fully quantum mechanical approach allows to represent the experimental data with equivalent accuracy compared to conventional analysis based on fits to empirical level

energy expressions, but at the same time provides us with much better physical model of the electronic state.

- Analysis of the ground and lowest triplet state of NaRb and NaCs highlighted the importance of taking into account the hyperfine mixing of weakly bound levels of these states near the asymptote for providing the proper long-range description.
- Comparison of the derived empirical potentials of the ground and selected excited states of NaRb and NaCs with the *ab initio* data allowed us to conclude that accuracy of *ab initio* potential energy curves is growing over the years, but measurements are still necessary for meeting the demands of modern spectroscopy tasks in the short-range region. Analysis showed that for more reliable predictions of excited state potentials in many cases it is better to use the differences of *ab initio* potential energy curves with respect to the ground state potential, if it is known with high accuracy. On the other hand, *ab initio* long-range potentials are of much higher accuracy and show agreement with the experiment consistent with the reported experimental and *ab initio* uncertainties.
- The results obtained in the course of work open path for new experimental studies, e.g. dynamic and structural studies of these molecules (measurements of lifetimes, permanent electric dipole moments, etc.) and cold collision experiments with atomic pairs.

Bibliography

[1] E. Wiedemann and G.C. Schmidt, Ann. Physik 42, 448 (1891).

[2] G. Herzberg, Molecular Spectra and Molecular Structure. I. Spectra of Diatomic Molecules, D. Van Nostrand Company, New York, Second Edition, 1953.

[3] C.H. Townes, A.L. Schawlow, Microwave Spectroscopy, McGraw-Hill, New York, 1955.

[4] A. Zaitsevskii, S.O. Adamson, E.A. Pazyuk, A.V. Stolyarov, O. Nikolayeva, O. Docenko, I. Klincare, M. Auzinsh, M. Tamanis, R. Ferber, and R. Cimiraglia, Phys. Rev. A 63, 052504 (2001).

[5] H. Lefebvre-Brion and R. W. Field, Perturbations in the Spectra of Diatomic Molecules, Academic, New York, London, 1986.

[6] Special issue on Cold molecules, Eur. Phys. J. D 31, 149 (2004).

[7] D. J. Heinzen, R. Wynar, P. D. Drummond, and K. V. Kheruntsyan, Phys. Rev. Lett. 84, 5029 (2000).

[8] M. G. Kozlov and D. DeMille, Phys. Rev. Lett. 89, 133001 (2002).

[9] J. J. Hudson, B. E. Sauer, M. R. Tarbutt, and E. A. Hinds, Phys. Rev. Lett. 89, 023003 (2002).

[10] D. DeMille, Phys. Rev. Lett. 88, 067901 (2002).

[11] www.nobel.se

[12] H.R. Thorsheim, J. Weiner, P.S. Julienne, Phys. Rev. Lett. 58, 2420 (1987).

[13] J.T. Bahns,W.C. Stwalley, P.L. Gould, Adv. At. Mol. Opt. Phys. 42, 171 (2000).

[14] F. Masnou-Seeuws, P. Pillet, Adv. At. Mol. Opt. Phys. 47, 53 (2001).

[15] A. Fioretti, D. Comparat, A. Crubellier, O. Dulieu, F. Masnou-Seeuws, P. Pillet, Phys. Rev. Lett. 80, 4402 (1998).

[16] N. Nikolov, E.E. Eyler, X.T. Wang, J. Li, H.Wang, W.C.Stwalley, P. Gould, Phys. Rev. Lett. 82, 703 (1999).

[17] A.N. Nikolov, J.R. Ensher, E.E. Eyler, H. Wang, W.C. Stwalley, P. Gould, Phys. Rev. Lett. 84, 246 (2000)

[18] C. Gabbanini, A. Fioretti, A. Lucchesini, S. Gozzini, M. Mazzoni, Phys. Rev. Lett. 84, 2814 (2000).

[19] F. Fatemi, K. Jones, P. Lett, E. Tiesinga, Phys. Rev. A 66, 053401 (2002).

[20] J. M. Sage, S. Sainis, T. Bergeman and D. DeMille, Phys. Rev. Lett. 94, 203001 (2005).

[21] M.W. Mancini, G. D. Telles, A. R. L. Caires,V. S. Bagnato, and L.G. Marcassa, Phys. Rev. Lett. 92, 133203 (2004).

[22] D.Wang, J. Qi, M. F. Stone, O. Nikolayeva, H.Wang, B. Hattaway, S. D. Gensemer, P. L. Gould, E. E. Eyler and W. C. Stwalley, Phys. Rev. Lett. 93, 243005 (2004).

[23] C. Haimberger, J. Kleinert, M. Bhattacharya, and N. P. Bigelow, Phys. Rev. A 70, 021402(R) (2004).

[24] Z. Hadzibabic, C. A. Stan, K. Dieckmann, S. Gupta, M. W. Zwierlein, A. Görlitz and W. Ketterle, Phys. Rev. Lett. 88, 160401 (2002).

[25] G. D. Telles, L. G. Marcassa, S. R. Muniz, S. G. Miranda, A. Antunes, C. Westbrook, and V. S. Bagnato, Phys. Rev. A 59, R23 (1999).

[26] Y. E. Young, R. Ejnisman, J. P. Shaffer, and N. P. Bigelow, Phys. Rev. A 62, 055403 (2000).

[27] S. Azizi, M. Aymar, O. Dulieu, Eur. Phys. J. D 31, 195 (2004).

[28] A. Crubellier, O. Dulieu, F. Masnou-Seeuws, M. Elbs, H. Knöckel, and E. Tiemann, Eur. Phys. J. D 6, 211 (1999).

[29] C. A. Stan, M.W. Zwierlein, C. H. Schunck, S.M. F. Raupach, and W. Ketterle, Phys. Rev. Lett. 93, 143001 (2005).

[30] S. Inouye, J. Goldwin, M. L. Olsen, C. Ticknor, J. L. Bohn, and D. S. Jin, Phys. Rev. Lett. 93, 183201 (2005).

[31] W.C. Stwalley, Eur. Phys. J. D 31, 221 (2004).

[32] C.A. Moore, G.P. Davis, R.A. Gottscho, Phys. Rev. Lett. 52, 538 (1984).

[33] M. Auzinsh, R. Ferber, O. Nikolayeva, N. Shafer-Ray, M. Tamanis, J. of Phys. D: Applied Physics 34, 624 (2001)

[34] M. Korek, A.R. Allouche, M. Kobeissi, A. Chaalan, M. Dagher, K. Fakherddin, M. Aubert-Frecon, Chem. Phys. 256, 1 (2000).

[35] M. Korek, A. R. Allouche, K. Fakhreddine, and A. Chaalan, Can. J. Phys. 78, 977 (2000).

[36] F. Hund, Z. Phys. 36, 637 (1926).

[37] R.A. Frosch and H.M. Foley, Phys. Rev. 88, 1337 (1952).

[38] L. Li, Q. Zhu, R.W. Field, Mol. Phys. 66, 685 (1989).

[39] R.J. Le Roy, in Specialist Periodical Reports, Molecular Spectroscopy (Chemical Society, London, 1973), Vol.1.

[40] R.J. Le Roy, Can. J. Phys. 52, 246 (1974).

[41] B.M. Smirnov and M.I. Chibisov, Zh. Eksp. Teor. Fiz. 48, 939 (1965) [Sov. Phys. JETP 21, 624 (1965)].

[42] M. I. Chibisov and R. K. Janev, Phys. Rep. 166, 1 (1988).

[43] J.L. Dunham, Phys. Rev. 41, 713 (1932); ibid 41, 721 (1932).

[44] R. Rydberg, Z. Phys. 73, 376 (1931); O. Klein, ibid 76, 226 (1932); A. L. G. Rees, Proc. Phys. Soc. London 59, 998 (1947).

[45] Y.H. Huang, R.J. Le Roy, J. Chem. Phys. 119, 7398 (2003).

[46] W. M. Kosman and J. Hinze, J. Mol. Spectrosc. 56, 93 (1975);

[47] C. R. Vidal and H. Scheingraber, J. Mol. Spectrosc. 65, 46 (1977).

[48] A. Pashov, W. Jastrzebski, and P. Kowalczyk, Comput. Phys.Commun. 128, 622 (2000).

[49] A. Pashov, Ph.D. thesis, Institute of Physics, Polish Academy of Sciences, 2000.

[50] A. Grochola, W. Jastrzebski, P. Kowalczyk, and A. Pashov, J. Chem. Phys. 121, 5754 (2004).

[51] W. H. Press, S. A. Teukolsky, W. T. Vetterling, and B. P. Flannery, Numerical Recipes in Fortran 77 (Cambridge University Press, 1999).

[52] W. Jastrzebski, W. Jaśniecki, P. Kowalczyk, R. Nadyak, and A. Pashov, Phys. Rev. A 62, 042509 (2000).

[53] A. Pashov, W. Jastrzebski, W. Jaśniecki, V. Bednarska, and P. Kowalczyk, J. Mol. Spectrosc. 203, 264 (2000).

[54] A. Pashov, W. Jastrzebski, and P. Kowalczyk, J. Chem. Phys. 113, 6624 (2000).

[55] W. Jastrzebski, A. Pashov, and P. Kowalczyk, J. Chem. Phys. 114, 10725 (2001).

[56] F. Martin, P. Crozet, A. J. Ross, M. Aubert-Frecon, P. Kowalczyk, W. Jastrzebski, and A. Pashov, J. Chem. Phys. 115, 4118 (2001).

[57] W. Jastrzebski, R. Nadyak, and P. Kowalczyk, Chem. Phys. Lett. 374, 297 (2003).

[58] A. Grochola, W. Jastrzebski, P. Kowalczyk, A. Ross, and P. Crozet, Chem. Phys. Lett. 372, 173 (2003).

[59] O. Allard, A. Pashov, H. Knöckel, and E. Tiemann, Phys. Rev. A 66, 42503 (2002).

[60] P. G. Hajigeorgiou and R. J. Le Roy, J. Chem. Phys. 112, 3949 (2000).

[61] R.J. Le Roy, J. Mol. Spectrosc. 191, 223 (1998).

[62] J. Y. Seto, R. J. Le Roy, J. Verges, and C. Amiot, J. Chem. Phys. 113, 3067 (2000).

[63] C. Samuelis, E. Tiesinga, T. Laue, M. Elbs, H. Knöckel, and E. Tiemann. 63, 012710 (2000).

[64] M. Marinescu and A. Dalgarno, Z. Phys. D: At., Mol. Clusters **36**, 239 (1996)

[65] O. Nikolayeva, I. Klincare, M. Auzinsh, M. Tamanis, R. Ferber, E.A. Pazyuk, A.V. Stolyarov, A. Zaitsevskii, R. Cimiraglia, J. Chem. Phys. 113, 4896 (2000).

[66] M. Walter and S. Barrat, Proc. Roy. Soc. London, 119, 257 (1928).

[67] P. Kusch, Phys. Rev., 49, 218 (1936).

[68] N. Takahashi and H. Katô, J. Chem. Phys. 75, 4350 (1981).

[69] Y-C. Wang, M. Kajitani, S. Kasahara, M. Baba, K. Ishikawa, and H. Katô, J. Chem. Phys. 95, 6229 (1991).

[70] Y-C. Wang, K. Matsubara, and H. Katô, J. Chem. Phys., 97, 811 (1992).

[71] K. Matsubara, Y-C. Wang, K. Ishikawa, M. Baba, A. J. McCaffery, and H. Katô, J. Chem. Phys., 99, 5036 (1993).

[72] S. Kasahara, T. Ebi, M. Tanimura, H. Ikoma, K. Matsubara, M .Baba, and H. Katô, J.Chem. Phys. 105, 1341 (1996).

[73] W. T. Zemke and W. C. Stwalley, J. Chem. Phys. 114, 10811 (2001).

[74] I. Klincare, M. Tamanis, R. Ferber, Chem. Phys. Lett. 382, 593 (2003).

[75] M. Tamanis, R. Ferber, A. Zaitsevskii, E.A. Pazyuk, A.V. Solyarov, Hongmin Chen, Jiangbing Qi, Henry Wang, W.C. Stwalley, J. Chem. Phys. 117, 7980 (2002).

[76] A. Jarmola, M. Tamanis, R. Ferber, E.A. Pazyuk, A.V. Stolyarov, JQSRT 95, 165 (2005).

[77] M.W. Mancini, A.R.L. Caires, G.D. Telles, V.S. Bagnato, and L.G. Marcassa, Eur. Phys. J. D 30, 105 (2004).

[78] B. Bussery, Y. Achkar, M. Aubert-Frecon, Chem. Phys. 116, 319 (1987).

[79] M. Marinescu and H. R. Sadeghpour, Phys. Rev. A. 59, 390 (1999).

[80] A. Derevianko, J. F. Babb, and A. Dalgarno, Phys. Rev. A 63, 052704 (2001).

[81] S. G. Porsev and A. Derevianko, J. Chem. Phys. 119, 844 (2003).

[82] S. B. Weiss and M. Bhattacharya and N. P. Bigelow, Phys. Rev. A 68, 042708 (2003).

[83] S. B. Weiss and M. Bhattacharya and N. P. Bigelow, Phys. Rev. A 69, 049903 (2004).

[84] H. Ouerdane and M. J. Jamieson, Phys. Rev. A 70, 022712 (2004).

[85] M. Bhattacharya, L.O. Baksmaty, S.B.Weiss, and N.P. Bigelow, Eur. Phys. J. D 31, 301 (2004).

[86] A. J. Ross, C. Effantin, J. d'Incan, and R. F. Barrow, Mol. Phys. 56, 903 (1985).

[87] C. Amiot, J. Chem. Phys. 93, 8591 (1990).

[88] A programm for fitting Dunham coefficients. Authors: E. Tiemann, H. Knöckel.

[89] W. Jastrzebski, P. Kowalczyk, and A. Pashov. J. Mol. Spectroscop. 209, 50 (2001).

[90] Ch. Lisdat and O. Dulieu and H. Knöckel and E. Tiemann. Eur. Phys. J. D, 17,319 (2002).

[91] F. H. Mies and E. Tiesinga and P. S. Julienne, Phys. Rev. A 61,022721 (2000).

[92] A. Stolyarov, private communication.

[93] W. Jastrzebski, P. Kortyka, P. Kowalczyk and A. Pashov, submitted to J. Chem. Phys., 2006.

[94] H. Knöckel, B. Bodermann, E. Tiemann. Eur. Phys. J. D 28, 199 (2004).

[95] A. A. Radzig and P. M. Smirnov, *Reference Data on Atoms, Molecules ad Ions*, Springer, Berlin, 1985.

[96] O. Dulieu, P. S. Julienne, J. Chem. Phys. 103, 60 (1995).

[97] O. Allard, C. Samuelis, A. Pashov, H. Knöckel, and E. Tiemann, Eur. Phys. J. D 26, 155 (2003).

[98] W. Jastrzebski and P. Kowalczyk, Phys. Rev. A 51, 1046 (1995).

[99] P. Juncar, J. Pinar, J. Hamon and A. Chartier, Metrologia 17, 77 (1981).

[100] W. Weizel and M. Kulp, Ann. Physik 5. Folge, 971 (1930).

[101] U. Diemer, H. Weickenmeier, M. Wahl, and W. Demtröder, Chem. Phys. Lett., 104, 489 (1984).

[102] A. Kopystynska, C. Gabbanini, S. Gozzini, M. Biagini, L.Moi, Phys. Lett. A 159, 266 (1991).

[103] J. P. Shaffer, W. Chalupczak, and N. P. Bigelow, Phys. Rev. A 61, 011404(R) (1999).

[104] J. P. Shaffer, W. Chalupczak, and N. P. Bigelow, Phys. Rev. Lett. 82, 1124 (1999).

[105] O. Docenko, M. Tamanis, J. Zaharova, R. Ferber, A. Pashov, H. Knöckel and E. Tiemann, accepted for publication in J. Chem. Phys.

Acknowledgments

First of all, I would like to thank a lot my supervisors Dr. Maris Tamanis and Prof. Ruvin Ferber for their guidance, help and support during all these years. I am extremely grateful to Dr. Asen Pashov, who taught me so many spectroscopy secrets, always gave a helping hand when I needed it and was not only a good colleague, but a real friend. Special thanks to Prof. Eberhard Tiemann, who kindly allowed to perform the experiments in his laboratory at the University of Hannover and fruitful discussions with whom opened me a lot of new knowledge in physics. I am also thankful to Dr. Horst Knöckel for his assistance and useful advices. My warmest thanks to Dr. Ilze Klincare for her friendly encouragement and help in physics and in life. I am also grateful to my colleagues Dr. Olga Nikolajeva and Jelena Zaharova for their friendly support. I would like to express also my gratitude to Dr. Andrey Stolyarov and Dr. Elena Pazyuk for sharing their valuable knowledge in molecular physics. I thank my family and friends for their love and understanding.

I acknowledge the support from the University of Latvia, Latvian Science Council, Morberg scholarship and European Social Fund.